Microfluidic Energy Conversion

By application of two phase flow

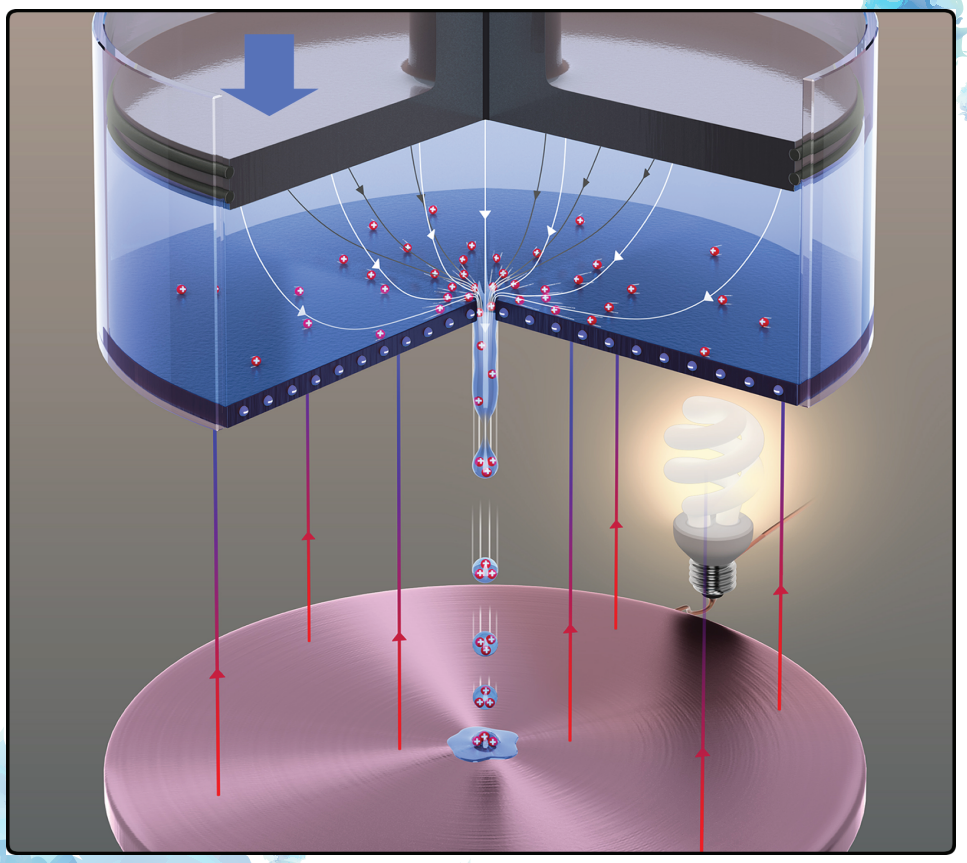

Yanbo Xie

MESA+
INSTITUTE FOR NANOTECHNOLOGY

BIOS
Lab on a Chip group

MICROFLUIDIC ENERGY CONVERSION

BY APPLICATION OF TWO PHASE FLOW

Yanbo Xie

UNIVERSITY OF TWENTE.

NWO

Thesis committee members:

Chairman	Prof. dr. ir. A.J. Mouthaan	University of Twente
Promotor	Prof. dr. ir. A. van den Berg	University of Twente
	Prof. dr. J.C.T. Eijkel	University of Twente
Members	Prof. dr. ir. W.G. van der Wiel	University of Twente
	Prof. dr. S.G. Lemay	University of Twente
	Prof. dr. M. Versluis	University of Twente
	dr. L. Shui	South China Normal University
	Prof. dr. H. Bruus	Technical University of Denmark

The work described in this thesis was performed at the BIOS Lab on a chip group of the MESA+ Institute for Nanotechnology at the University of Twente, Enschede, The Netherlands. The work was financially supported by the NWO TOP grant 700.58.341 'Energy from streaming potential using nanotechnology'.

Author: Yanbo Xie
Tittle: Microfluidic energy conversion device
By application of two phase flow
PhD Thesis, University of Twente, The Netherlands
ISBN: 978-90-365-0744-8
DOI: 10.3990/1.9789036507448
Publisher: Wöhrmann Print Service, Zutphen, The Netherlands
Cover design: Yanbo Xie; 3D image created by Vincent Bos in Nymus3D

MICROFLUIDIC ENERGY CONVERSION

BY APPLICATION OF TWO PHASE FLOW

DISSERTATION

to obtain
the degree of doctor at the University of Twente,
on the authority of the rector magnificus,
prof.dr. H. Brinksma,
on account of the decision of the graduation committee,
to be publicly defended
on Thursday the 26th of September 2013 at 14:45 hours

by

Yanbo Xie

Born on the 16th of April 1984
in Xi'an, ShaanXi Province, China

This dissertation has been approved by:

Promotors: prof.Dr.ir. Albert van den Berg and prof.Dr. Jan C.T. Eijkel

To my wife and family

Table of Contents

Chapter 1

Introduction

This chapter introduces the principle of energy conversion from the streaming potential. Present work including experiments and theoretical predictions to improve the energy conversion efficiency are reviewed. Aims, methods and outline of this thesis are presented.

1. Introduction

With the rapid growth of the economy and population in the past decades, the electrical energy consumption increases rapidly. According to research by Paul B. Weisz [1], the consumption of oil increased 16 times since 20th century, while the prediction from research indicates that the peak and subsequent decline in world oil production will probably occur within the next few decades. In order to prevent energy crisis from traditional energy sources, people are eager to find new energy sources instead.

The other important issue to consider when developing new energy sources is the "greenhouse effect". Traditional energy sources such as mine oil and coal produce large quantities of CO_2, which was pointed at as the main reason of climate change on earth. The United Nations Frame work conventions' researched the historical carbon emission level and pointed at the need of "stabilization of greenhouse-gas concentrations in the atmosphere at a level that would prevent dangerous anthropogenic interference with the climate system". [2]

To meet the demands of energy consumption, new energy sources are under research and development, and this has become one of the most important research topics. In particular, novel environmentally-friendly energy conversion systems are required. Because of the recent development of micro-machined techniques, more and more novel method for energy harvesting using micromachining are invented, to find potential paths to replace traditional energy sources. To increase the energy harvesting efficiency thereby is one of the most important goals. High efficiency and high power density while using environmentally-friendly devices or materials are preferable for future applications. The table below lists the energy conversion properties of micro-scale devices [3]:

Table 1: the examples of micro-machine for energy harvesting

Machine	Energy input	Energy output	Typical Efficiency	Advantages	Ref.
Micro heat engine	Heat	Electrical	37%	High power density	[4-6]
Micro fuel cell	Chemical	Electrical	Up to 60%	High power density	[7]
MEMS piezoelectric	Vibration	Electrical	7%	More kT energy	[8]
Photovoltaic cells	Solar	Electrical	12%	Better engineered materials	[9]
Nanostructured materials	Heat, electrical, chemical	Electrical	N/A	Nanoscale only	[10]
Biologically inspired approaches	(Bio)chemical	(Bio)chemical, Electrical	N/A	Nanoscale only	[11]
Thermo-acoustics	Heat	Acoustical	3%	Can pump microchannels	[12]
Streaming potential	Pressure	Electrical	3-5%	Nanoscale only	[13-15]

The developing ‘‘lab on a chip’’ technology provides new opportunities to convert fluidic mechanical energy to electrical energy.[16] Electro-kinetic phenomena, such as the streaming current, can convert mechanical energy into electrical energy.[17] In this thesis we consider the use of streaming current to convert mechanical energy into electrical energy.

2. Microfluidic Energy conversion

2.1 Electrical double Layer (EDL)

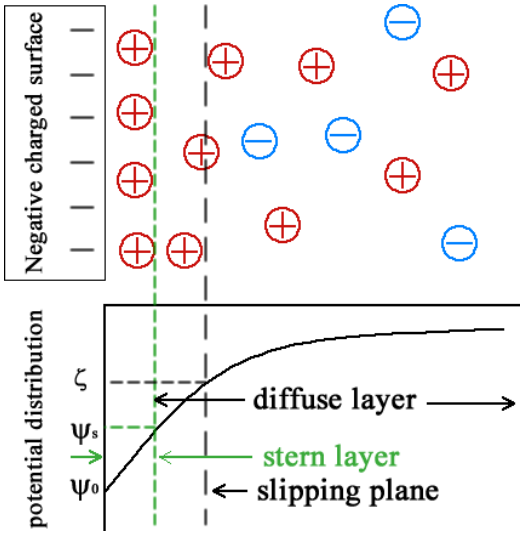

Figure 1 shows the surface potential distribution in liquid phase.

At most interfaces of a liquid with a solid, liquid or the gas phase, the interface will acquire charges, due to chemical bond dissociation or adsorption. This surface charge introduces an electrical potential distribution in the liquid. In the liquid, for example water, ions of the opposite polarity to the surface charge, named counter-ions, are attracted by the electro-static Coulomb force, forming the electrical double layer (EDL). According to Gouy-Chapman-Stern theory, the EDL can be divided into two layers (as shown in figure 1): a first layer of ions assembled at the interface, named the Stern layer, and another layer of counter-ions distributed in the liquid according to the equilibrium of thermal and electrical forces, named the diffuse layer.

2.2 Zeta potential and streaming potential

To well describe electrical kinetic phenomena, an artificial plane was introduced - called the slipping plane – at which the potential with respect to the bulk potential is called the zeta potential. It therefore describes the surface electrostatic potential

at the position of fluidic slipping plane. It is based on the assumption that only the counter-ions outside of the liquid slipping plane can be driven by fluid. Hence, the zeta potential dominates the electro kinetic properties near a charged object's surface.

When water flows through a surface-charged channel, counter-ions past the slipping plane move with the water and produce electrical current. When this current is picked up by two electrodes at the channel ends and there is no external load resistance connected between them, the current flowing through the circuit is maximal. This maximum current is called the streaming current. By increasing the load resistance, an electrical potential difference is generated between the ends of the channel, producing a conduction current in the channel with opposite direction to the streaming current. When the voltage produces a conduction current that totally balances the streaming current, the generated voltage reaches its maximum value, named the streaming potential.

2.3 Principle of energy conversion

In this thesis, we focus on energy conversion by the streaming current. In other words, energy conversion from mechanical energy of fluidic flow to electrical energy.

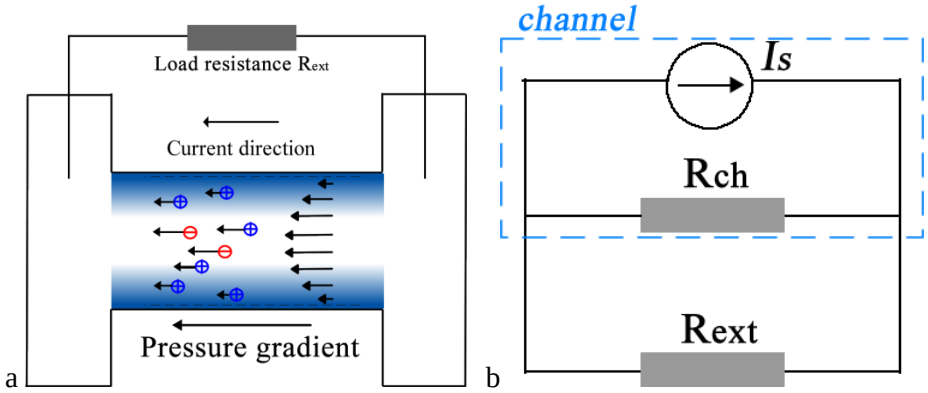

Figure 2. a. The principle of energy conversion from streaming current. Counter-ions move with the water flow producing electrical current. Output electrical power is generated by connecting an external electrical resistance, such as a lamp.

b describes the equivalent circuit of system. Maximal output power can be obtained when channel resistance equals to external load resistance.

As described above, a streaming current and streaming potential are generated by liquid flow through a surface-charged channel, as shown in figure 2. By placing two electrodes at the channel ends, the generated current can be collected, producing an electrical potential difference via a connected electrical resistance. Then the mechanical input energy delivered by the water flow and calculated as $\Delta P \times Q$ (with ΔP the applied pressure and Q the water volume flow rate), can be converted into electrical energy which can be calculated by $I \times V$.
Figure 2b shows the equivalent circuit of the system. Streaming current can be considered as a constant current source, which is function of the pressure gradient, zeta potential and area of channel. The electrical resistance of the channel solution, R_{ch} is connected in parallel with the external resistance R_{ext}. The current through R_{ch} indicates the conduction current and doesn't contribute to the output power. According to physical laws, we know that to obtain maximal output power from R_{ext}, the external resistance has to equal the internal resistance. This model has been proven valid in micro- and nano-fluidic systems. [18]
This method has many advantages: 1. It is quite simple. There are no moving parts needed for the energy conversion and it only needs water, an applied pressure difference and micro/nano structures.[3] 2. It doesn't produce any new chemicals, so that it is environmentally-friendly and provides an potential method of generating green energy. 3. Using the developing Lab on a chip technology and nanotechnology, it could be possible to integrate this method in small devices making it feasible for small scale or portable application.

3. Review of energy conversion from streaming potential

Since Osterle first proposed that electrokinetic phenomena can convert mechanical energy to electrical energy,[19, 20] many researchers worked on the fundamental and applied research on how to make the system more efficient.

3.1 Microfluidic channel and porous material

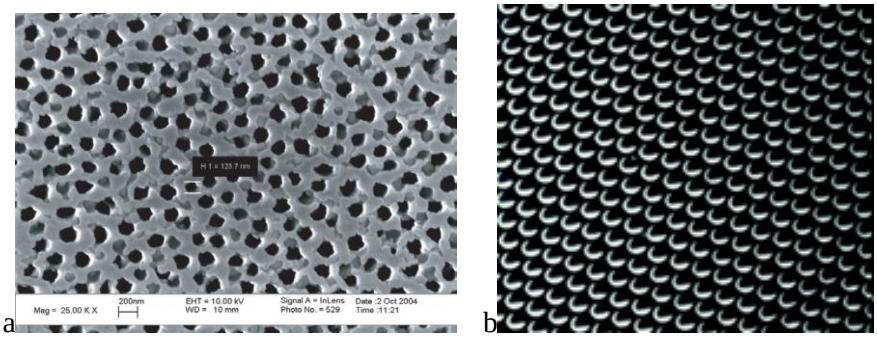

a b

Figure 3 a SEM pictures of a alumina membrane with 200 nm pores.[18] b. glass microchannel array consisting of an array of 3. 4×10^5 circular microchannels, each with a pore diameter of 10 μm, with its two faces coated with a 100 nm layer of gold[21]

With the developing micro/nanofluidic technology, where it is possible to obtain quite high surface to volume ratio devices, the energy conversion from the streaming current came back in the researchers sight. Many experiments and theories have been developed during the last decades. J. Yang and his colleagues used porous glass material to perform energy conversion, which has a pore size ranging from 10μm to 16μm.[22] They obtained an electrical output power of about 1.3 μW with an efficiency of less than 0.5%. Other experiments in parallel microfluidic channels also showed the efficiency in the same order. [18, 23] A recent study showed that the position of the electrodes can also influence the performance of energy conversion. By decreasing the resistance and the capacitance of the whole system, the electrical output power of a device with a 10 μm diameter pore array (Figure 3b) can reach one milliWatt and an energy conversion efficiency of 1.3%.[14, 21, 24]

3.2 Nanofluidic channel

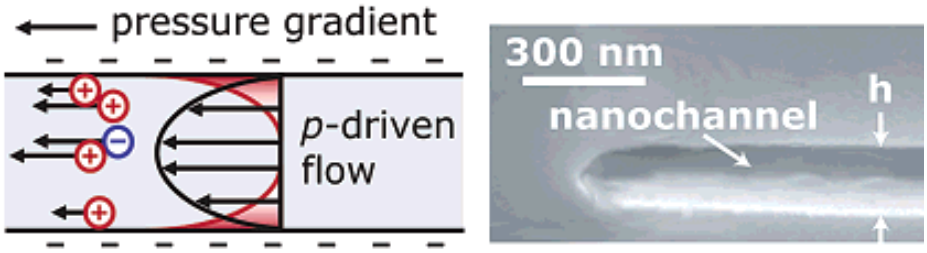

Figure 4 Schematic illustration of electrokinetic effects in nanochannel. Left: a pressure-driven flow carries counter-ions within the double layer, producing a streaming current. Right: Side view of a 200-nm-high silica nanochannel, imaged by scanning electron microscopy.[25]

Theoretical studies pointed out that a higher energy conversion efficiency can be achieved by using channels with EDL overlap.[25, 26] Unipolar solution of counterions will dominate the electrical properties, and a maximal efficiency can be obtained when the EDL fills half the channel height. [27-30] Van der Heyden performed experiments based on a one dimensional nanochannel, decreasing the height of the channel to 75nm. The efficiency reached around 2~3%. [15, 25] Other nanofluidic devices, such as nanopores, can also achieve similar efficiencies with a single circular track-etched pore. [13]

By using EDL overlap, maximal efficiencies of nanodluidic devices were theoretically predicted to be 12%. However, due to surface conductance [31], the position of electrodes[21], surface chemistry and other reasons[32, 33], it has not been achieved experimentally.

3.3 Slip boundary

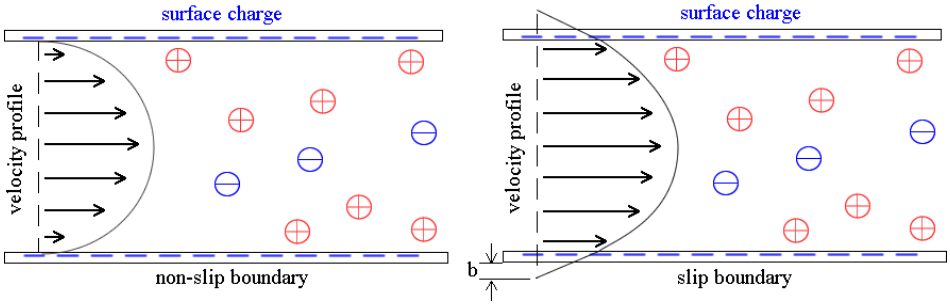

Figure 5 left: Pressure-driven velocity profile with a no-slip boundary in channel. Right: Profile at a slipping boundary. The water velocity at the inner wall of the channel now is not zero. According to EDL theory, the highest concentration of net charges is nearby the channel surface. Thus a slip boundary can help water flow to deliver charges more efficiently.

A slip boundary for energy conversion was then proposed to enhance the energy conversion efficiency. The streaming current is based on the counter-ions movement nearby the surface. A slip boundary can help to increase the transport flux of these ions, thus increasing the streaming current and output power.
Theoretical simulation shows in the same direction. Ren's theoretical study shows the efficiency can be enhanced to up to 40% with a reasonable slip length of 50nm. [34] Many theoretical researches showed that longer slip lengths shall help to increase efficiency. [16, 33-36] It has been observed that the apparent zeta potential can be increased by introducing a hydrophobic surface in nanofluidic channel.[37] However, increasing the surface potential is expected to decrease the hydrophobicity, shortening the slip length. Periodic patterns were proposed to keep the EDL and introduce slip at the same time. [32, 35, 38, 39] Moreover, by slip of water molecules is will be possible to increase the conduction current[40], which will lead to a lower streaming potential and efficiency.

3.4 Others

Ion sizes

Other methods and factors also have been considered or proposed to increase the energy conversion efficiency. Due to the oscillation of the ion distribution nearby the surface, the size and correlation of ions in narrow confined channels have significant effects on device properties over large parts of this parameter space. [41] Distribution of large ions in quite narrow confined channels can't be described by traditional EDL theory. Oscillation of the ion concentrations induces a higher concentration of net charges far from the wall where the water speed is higher. This could then increase the streaming current and energy conversion efficiency.

Polymer solution

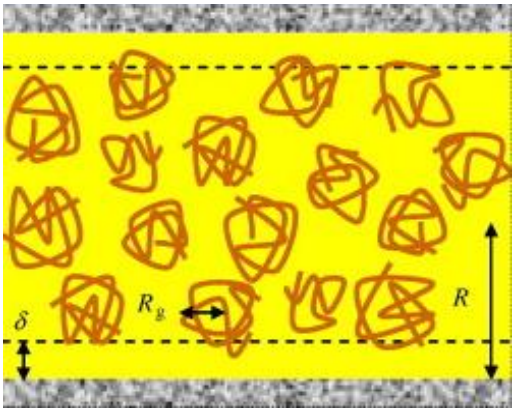

Figure 6 Schematic representation of a solution of non-adsorbing polymers in a microchannel[42]

With addition of non-adsorbing polymers in the channel solution, polymers will be at bulk concentration in the center of the channel but will form a depletion layer containing no polymer near the channel surface. A polymer solution can thus effectively increase the flow resistance in the polymer filled area while keeping the velocity in the depletion zone nearby the channel wall (where also the EDL is located) unaltered. Thus, the efficiency can be enhanced by changing the flow profile compared to a simple electrolyte solution. The theoretical enhancement

ratio of the efficiency can be over 200 times larger with absolute efficiency around 1%.[42] Recent experiments in our group confirm the theoretical predictions. [43]

Graphene

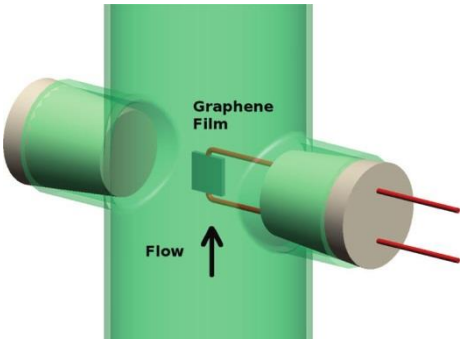

Figure 7 Water flow along a graphene surface, generating electrical energy due to moving the charges near the graphene surface. [44]

Graphene is a nanosheet which has only a single layer of atoms and has many unique excellent properties. [45] Newaz et.al studied the streaming potential for graphene in an electrolyte solution by using a graphene field effect transistor. [44] They found that the sensitivity varied dependent on the fluidic flow and ionic concentration. They successfully detected the flow as small as 70nL/min and detect the change of ion concentrations as low as 40nM. [44] P.Dhiman et. al found that the streaming potential is of a similar order of magnitude as a carbon nanotube. The harvested electrical power was 85nW in a $30\times16\mu m^2$ graphene surface, corresponding to the power density of $175W/m^2$. [46]

Jet flow

Duffin and Saykally used a metal orifice to create a microjet and to generate electrical energy. They obtained an energy conversion efficiency exceeding 10%.[47, 48] The liquid jet shot out from a micron-sized pore, breaking up into many droplets, which carried the streaming current but were isolated by the surrounding air. The conduction current could as a result totally be eliminated and the setup thus prevented any energy dissipation by the conduction current. The authors still employed a classical streaming potential model to interpret their data

and as a result attributed the high efficiency due to preventing backflow of current as occurs in the classical electrokinetic energy conversion experiments referred to above. In this thesis we develop a comparable experiment and give an analysis on the limitations of the energy conversion efficiency for liquid jet-based systems in chapters 3 to 6.

4. Aim of the project

$$\text{Efficiency} = \frac{I \cdot V}{\Delta p \cdot Q}$$

For an energy conversion device, the efficiency of system will be of prime importance. The energy conversion efficiency is defined by electrical output power (current times voltage $I \cdot V$) divided by mechanical input power (pressure difference times flow rate $\Delta P \cdot Q$), shown above. The equation shows many possibilities to increase the conversion efficiency.

The first direct way is to increase streaming current I, such as by increasing zeta potential or introducing a slip boundary, to increase the output power and efficiency.

The second way to increase the output power is to increase the streaming potential, which is usually related to the internal resistance of the system. An example of this method is by using two phase flow to increase internal resistance, so that the streaming potential can be increased. This approach will be fully discussed in Chapter 2.

It is also possible to decrease the flow rate, in other words, to increase flow resistance, and at the same time keep the same fluid motion in the EDL. Then the output power is still been kept in the same order of magnitude, but due to the decrease of flow rate the efficiency can be enhanced. An example approach to increase the flow resistance is by introducing polymer solutions, which can decrease the flow velocity in the ion neutral area, but create a depletion zone nearby surface.

The power density (W/m^2) and the total output power (W) are another two important factors for energy conversion devices. It is especially important for daily use. Micro systems provide possibilities to develop small, portable and low-cost green energy sources.

5. Outline of the thesis

Chapter 1 describes the principle of energy conversion from fluidic flow, the aims of this project and reviews the previous work on energy conversion by the streaming current.

Chapter 2 shows that the energy conversion efficiency can be enhanced by the addition of gas bubbles. Gas bubbles can increase the internal electrical resistance and decrease the conduction current, thus increasing the output power compared with traditional single phase flow.

Chapter 3 shows a high efficiency energy conversion device by micro water jet. Droplets created by jet breakup contain charges which are collected by a bottom target, while a voltage is produced via an electronic circuit. Power conversion happens when droplets travel against the electrical field and convert kinetic energy into electrical energy.

Chapter 4 provides a theoretical understanding of the micro-jet system. We theoretically estimate the energy loss factors in the system, such as the fluidic friction before jet creation, and energy losses in surface tension and air friction. We predict the theoretically maximum efficiency and ways to improve the performance.

Chapter 5 introduces another method to induce charges in the droplets, namely by applying a gate voltage. We fundamentally study the induced current as function of applied gating voltage, pressure, salt concentration and so on. A model of the induced current is established for prediction and understanding of the system.

Chapter 6 introduces a self-gated system by using two jets. The idea comes from 'Kelvin's thunderstorm': his droplet energy generator. A gating voltage does not need to be supplied by an external voltage source, but can instead be supplied by another target of opposite polar voltage. This system can produce a high electrical power just by applying a pressure difference.

Chapter 7 summarizes the work on energy conversion from fluidic flow. Preliminary devices are proposed for real applications. The outlook proposes more possibilities for further improvement of the system and applications.

6. References

1. Weisz, P.B., *Basic choices and constraints on long-term energy supplies.* Physics Today, 2004. **57**(7): p. 47-52.
2. Hoffert, M.I., et al., *Energy implications of future stabilization of atmospheric CO2 content.* Nature, 1998. **395**(6705): p. 881-884.
3. Pennathur, S., J.C.T. Eijkel, and A. van den Berg, *Energy conversion in microsystems: is there a role for micro/nanofluidics?* Lab on a Chip, 2007. **7**(10): p. 1234-1237.
4. Lee, C.H., et al., *Design and fabrication of a micro Wankel engine using MEMS technology.* Microelectronic Engineering, 2004. **73-4**: p. 529-534.
5. Wu, S., et al., *Micro heat exchanger by using MEMS impinging jets.* Mems '99: Twelfth Ieee International Conference on Micro Electro Mechanical Systems, Technical Digest, 1999: p. 171-176.
6. Majumdar, A. and J. Varesi, *Nanoscale temperature distributions measured by scanning joule expansion microscopy.* Journal of Heat Transfer-Transactions of the Asme, 1998. **120**(2): p. 297-305.
7. Mitrovski, S.M., L.C.C. Elliott, and R.G. Nuzzo, *Microfluidic devices for energy conversion: Planar integration and performance of a passive, fully immersed H2-O2 fuel cell.* Langmuir, 2004. **20**(17): p. 6974-6976.
8. Glockner, P.S. and G.F. Naterer, *Recent advances in nano-electromechanical and microfluidic power generation.* International Journal of Energy Research, 2007. **31**(6-7): p. 603-618.
9. Bermejo, S. and L. Castaner, *Dynamics of MEMS electrostatic driving using a photovoltaic source.* Sensors and Actuators a-Physical, 2005. **121**(1): p. 237-242.
10. Gur, I., et al., *Hybrid solar cells with prescribed nanoscale morphologies based on hyperbranched semiconductor nanocrystals.* Nano Letters, 2007. **7**(2): p. 409-414.

11. LaVan, D.A. and J.N. Cha, *Approaches for biological and biomimetic energy conversion.* Proceedings of the National Academy of Sciences of the United States of America, 2006. **103**(14): p. 5251-5255.
12. Amari, M., V. Gusev, and N. Joly, *Transient unidirectional acoustic streaming in annular resonators.* Ultrasonics, 2004. **42**(1-9): p. 573-578.
13. Xie, Y.B., et al., *Electric energy generation in single track-etched nanopores.* Applied Physics Letters, 2008. **93**(16): p. -.
14. Mansouri, A., L.W. Kostiuk, and S. Bhattacharjee, *Streaming Current Measurements in a Glass Microchannel Array.* Journal of Physical Chemistry C, 2008. **112**(42): p. 16192-16195.
15. van der Heyden, F.H.J., et al., *Power generation by pressure-driven transport of ions in nanofluidic channels.* Nano Letters, 2007. **7**(4): p. 1022-1025.
16. Davidson, C. and X.C. Xuan, *Electrokinetic energy conversion in slip nanochannels.* Journal of Power Sources, 2008. **179**(1): p. 297-300.
17. Hunter, R.J., *Zeta potential in colloid science: principles and applications.* Colloid science, 1981. **2**.
18. Lu, M.C., et al., *A mechanical-electrokinetic battery using a nano-porous membrane.* Journal of Micromechanics and Microengineering, 2006. **16**(4): p. 667-675.
19. Osterle, J.F., J. Appl. Mech., 1964. **31**: p. 161.
20. Yang, R.J., L.M. Fu, and C.C. Hwang, *Electroosmotic entry flow in a microchannel.* Journal of Colloid and Interface Science, 2001. **244**(1): p. 173-179.
21. Mansouri, A., S. Bhattacharjee, and L. Kostiuk, *High-power electrokinetic energy conversion in a glass microchannel array.* Lab on a Chip, 2012. **12**(20): p. 4033-4036.
22. Lu, F.Z., J. Yang, and D.Y. Kwok, *Flow field effect on electric double layer during streaming potential measurements.* Journal of Physical Chemistry B, 2004. **108**(39): p. 14970-14975.
23. Olthuis, W., et al., *Energy from streaming current and potential.* Sensors and Actuators B-Chemical, 2005. **111**: p. 385-389.
24. Chang, C.C. and R.J. Yang, *Electrokinetic energy conversion in micrometer-length nanofluidic channels.* Microfluidics and Nanofluidics, 2010. **9**(2-3): p. 225-241.
25. van der Heyden, F.H.J., et al., *Electrokinetic energy conversion efficiency in nanofluidic channels.* Nano Letters, 2006. **6**(10): p. 2232-2237.
26. Huang, K.D. and R.J. Yang, *Electrokinetic behaviour of overlapped electric double layers in nanofluidic channels.* Nanotechnology, 2007. **18**(11)

27. Daiguji, H., et al., *Electrochemomechanical energy conversion in nanofluidic channels.* Nano Letters, 2004. **4**(12): p. 2315-2321.
28. Stein, D., M. Kruithof, and C. Dekker, *Surface-charge-governed ion transport in nanofluidic channels.* Physical Review Letters, 2004. **93**(3): p. -.
29. Daiguji, H., et al., *Theoretical study on the efficiency of nanofluidic batteries.* Electrochemistry Communications, 2006. **8**(11): p. 1796-1800.
30. Hughes, B.T., et al., *One-dimensional axial simulation of electric double layer overlap effects in devices combining micro- and nanochannels.* Microfluidics and Nanofluidics, 2008. **5**(6): p. 761-774.
31. Davidson, C. and X.C. Xuan, *Effects of Stern layer conductance on electrokinetic energy conversion in nanofluidic channels.* Electrophoresis, 2008. **29**(5): p. 1125-1130.
32. Zhao, H., *Streaming potential generated by a pressure-driven flow over superhydrophobic stripes.* Physics of Fluids, 2011. **23**(2).
33. Zhao, C.L. and C. Yang, *On the competition between streaming potential effect and hydrodynamic slip effect in pressure-driven microchannel flows.* Colloids and Surfaces a-Physicochemical and Engineering Aspects, 2011. **386**(1-3): p. 191-194.
34. Ren, Y.Q. and D. Stein, *Slip-enhanced electrokinetic energy conversion in nanofluidic channels.* Nanotechnology, 2008. **19**(19): p. -.
35. Squires, T.M., *Electrokinetic flows over inhomogeneously slipping surfaces.* Physics of Fluids, 2008. **20**(9): p. -.
36. Garai, A. and S. Chakraborty, *Steric effect and slip-modulated energy transfer in narrow fluidic channels with finite aspect ratios.* Electrophoresis, 2010. **31**(5): p. 843-849.
37. Bouzigues, C.I., P. Tabeling, and L. Bocquet, *Nanofluidics in the debye layer at hydrophilic and hydrophobic surfaces.* Physical Review Letters, 2008. **101**(11): p. -.
38. Bocquet, L. and J.L. Barrat, *Flow boundary conditions from nano- to micro-scales.* Soft Matter, 2007. **3**(6): p. 685-693.
39. Goswami, P. and S. Chakraborty, *Energy Transfer through Streaming Effects in Time-Periodic Pressure-Driven Nanochannel Flows with Interfacial Slip.* Langmuir, 2010. **26**(1): p. 581-590.
40. Vermesh, U., et al., *Fast Nonlinear Ion Transport via Field-induced Hydrodynamic Slip in Sub-20-nm Hydrophilic Nanofluidic Transistors.* Nano Letters, 2009. **9**(4): p. 1315-1319.
41. Gillespie, J.H.a.D., *Ion Correlations in Nanofluidic Channels: Effects of Ion Size, Valence, and Concentration on Voltage- and Pressure-Driven Currents.* Langmuir, 2013. **4**(29): p. 4.

42. Berli, C.L.A., *Electrokinetic energy conversion in microchannels using polymer solutions.* Journal of Colloid and Interface Science, 2010. **349**(1): p. 446-448.
43. Trieu Nguyen, Y.X., Lennart J. de Vreede, Albert van den Berg and Jan C.T. Eijkel *Highly Enhanced Energy Conversion from the Streaming Current by Polymer Addition.* Lab on a Chip, 2013.
44. Newaz, A.K.M., et al., *Graphene Transistor as a Probe for Streaming Potential.* Nano Letters, 2012. **12**(6): p. 2931-2935.
45. Castro Neto, A.H., et al., *The electronic properties of graphene.* Reviews of Modern Physics, 2009. **81**(1): p. 109-162.
46. Dhiman, P., et al., *Harvesting Energy from Water Flow over Graphene.* Nano Letters, 2011. **11**(8): p. 3123-3127.
47. Duffin, A.M. and R.J. Saykally, *Electrokinetic Power Generation from Liquid Water Microjets.* Journal of Physical Chemistry C, 2008. **112**(43): p. 17018-17022.
48. Duffin, A.M. and R.J. Saykally, *Electrokinetic hydrogen generation from liquid water microjets.* Journal of Physical Chemistry C, 2007. **111**(32): p. 12031-12037.

Chapter 2

Strong enhancement of streaming current power by application of two phase flow

The performance of a streaming-potential based microfluidic energy conversion system can be strongly enhanced by the use of two phase flow. Injection of gas bubbles into a liquid channel increases both the maximum output power and the energy conversion efficiency. While in single-phase systems, the internal conduction current induced by the streaming potential limits the output power, in a two-phase system the bubbles reduce this current and increase the power. The addition of bubbles enhanced the maximum output power of the system by a factor of 74 and the efficiency of the system by a factor of 163 compared with single phase flow. To study the enhancement effect in a single channel, the output power and efficiency were also quantitatively derived from the experimental results.

Modified from: Yanbo Xie and John D. Sherwood and Lingling Shui and Albert van den Berg and Jan C.T. Eijkel "Strong enhancement of streaming current power by application of two phase flow." Lab on a chip, 11 (23). 4006-4011.

1. Introduction

As described in Chapter 1, streaming current can convert mechanical energy of water flow into electrical energy, by moving net charges in electrical double layer.[1] Many research has been done by micro/nano channels, with maximum efficiency around 3-5%.[2, 3] From the equivalent circuit of current in nanochannel (Chapter 1 figure 1.2b), the output power and efficiency could be enhanced by internal resistance increasing. Hence, increasing the channel resistance will help to increase the energy conversion performance.

Streaming currents or potentials generated by multiphase flow have been studied for geophysical, mineral and petroleum applications involving large length scales.[4-7] In this chapter, we investigate the effect of two-phase flow on energy conversion at the microscopic scale, and show that the injection of bubbles into a liquid channel strongly increases both the maximum output power and the conversion efficiency. Both hydrophilic and hydrophobic channels were used to study the energy conversion enhancement.

2. Principle

A streaming potential generates both a current I_{ext} through the external circuit, and an internal conduction current I_C flowing in the channel in the opposite direction to the streaming current $I_S = I_{ext} + I_C$ (see Fig.1). In the two-phase flow system, gas bubbles with almost zero conductivity are injected into the moving liquid phase. The gas bubbles occupy most of the cross-sectional area of the channel, leaving little space for ion transport[8-11]. As a consequence the electrical resistance of the channel increases, decreasing I_C and making I_{ext} higher than in single phase flow. As a result, the power delivered to the external circuit increases. At the same time the input power needed to generate the flow is not significantly affected, so that the power conversion efficiency increases. We used one of the simplest ways to generate gas bubbles in our system, namely a T junction (shown in Figure 1a).

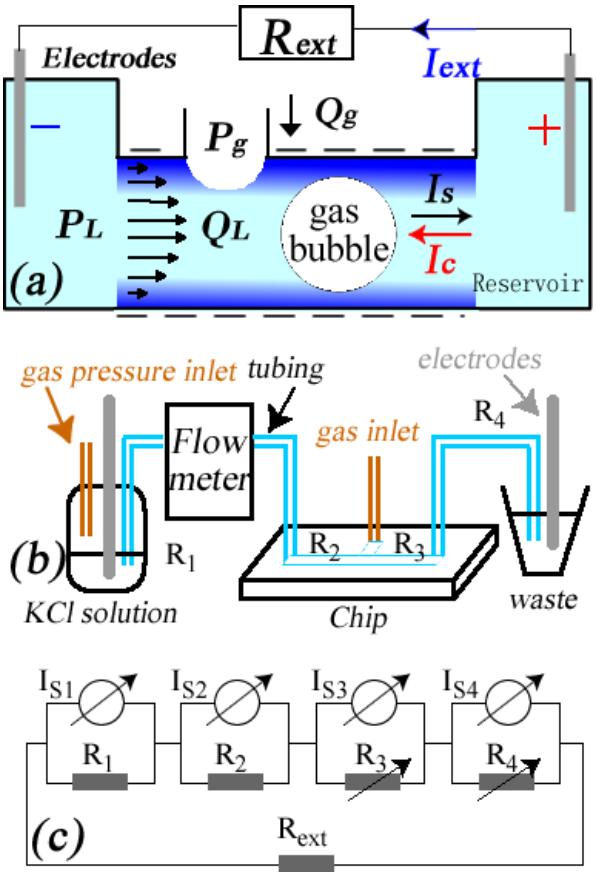

Figure. 1. (a) Schematic of the experiment. (b) The main sections of the experimental setup. (c) The equivalent circuit of the energy generation system, divided into 4 sections. I_{S1} and R_1 refer to the inlet tubing; I_{S2} and R_2 to the chip channel before the T junction; I_{S3} and R_3 to the chip channel after the T-junction and I_{S4} and R_4 to the outlet tubing.

3. Experimental setup

A gas source (99% purity N_2) was used both to drive the liquid flow and to generate gas bubbles. The gas source was connected to a gas-tight bottle filled with a liquid solution that was forced into a microfluidic chip via fused silica tubing (44 cm long, 150 μm ID) (Figure 1b). The chip outlet was connected to a waste reservoir via fused silica tubing (15 cm long, 100 μm ID). A flow meter (Fluigent Maesflo) measured the liquid flow rate Q_L. The gas source was furthermore directly connected to the chip in order to generate gas bubbles. The pressures of the two gas paths were controlled individually using a high accuracy gas pressure pump (Fluigent MFCS). The resulting gas/water two-phase flow was collected in the waste bottle. Two Ag/AgCl electrodes inserted into the gas-tight solution bottle and the waste bottle allowed electrical measurements. Voltages were applied by a Keithley 2410 voltage source, and currents were measured by a Keithley 6485 pico-ammeter. A 1mM KCl solution (bulk conductivity 140±10 μS/cm) was prepared from diluted 1M KCl and the pH adjusted to 9.2. Nonionic surfactant Tween 20 at critical micellar concentration (9.23×10^{-5} M) was added to the solution to assure the reliable generation of gas bubbles. A chip with a T junction channel for bubble generation was fabricated by wet etching in borofloat wafers, containing channels of width w =40 μm, height h =10 μm. and length L=3.8 mm with the T junction in the middle.

Equivalent circuit

Suppose that fluid of viscosity η flows along a channel of length L, width w and height h due to a pressure difference ΔP between the ends of the channel. If charge clouds are thin compared to the channel dimensions (w, h), the electrical streaming current generated by convection of the ionic charge cloud adjacent to the charged walls of the channel is

$$I_S = -\varepsilon\varepsilon_0\zeta wh\Delta P / \eta L \qquad (1)$$

where ε_0 is the permittivity of free space, ε the relative permittivity of the fluid and ζ the electrical (zeta) potential at the shear plane of the channel walls. The flow circuit, depicted in Figure 1(b), consists of four different channel sections

connected in series, and an equivalent circuit of the energy conversion system is shown in Figure 1(c). Each section (numbered i) can be considered as a constant current source with an internal electrical resistance R_i, the latter determined by the channel cross section, length and solution conductivity. The channel system is finally connected in series with the external resistance R_{ext}. The resistance of the Ag/AgCl electrodes to charge transport is neglected. When gas bubbles are injected into the system, the electrical resistances R_3, R_4 after the T junction vary with the volume fraction of gas, and are therefore marked as variable resistors. From Kirchhoff's laws, we obtain the streaming current of the entire system:

$$I_S = \frac{I_{S1}R_1 + I_{S2}R_2 + I_{S3}R_3 + I_{S4}R_4}{R_1 + R_2 + R_3 + R_4} \tag{2}$$

If no current flows in the external circuit, the streaming potential of the system can be expressed as:

$$U_S = I_{S1}R_1 + I_{S2}R_2 + I_{S3}R_3 + I_{S4}R_4 \tag{3}$$

Assuming all of the resistances obey Ohmic laws, the output power attains its maximum value when $R_{ext}=R_1+R_2+R_3+R_4$ [12], so that the external current is $I_S/2$ and the output power is

$$P_{o,\max} = \frac{(I_{S1}R_1 + I_{S2}R_2 + I_{S3}R_3 + I_{S4}R_4)^2}{4(R_1 + R_2 + R_3 + R_4)} \tag{4}$$

Equations (2) and (4) indicate that the streaming current and output power of a single section become dominant when its resistance is much larger than that of the other sections. After injection of gas bubbles, R_3 and R_4 increase and the streaming current generated in these two sections becomes more important, which will explain our experimental results shown below. Due to the large diameter of the tubing in section 4, the bubbles in this tubing at moderate gas flow rates occupy only a small part of the cross-sectional diameter in the outlet tubing, so that R_4 changes little. At high gas pressure however, gas bubbles start to fuse to form slugs in the outlet tubing, thereby increasing R_4. We shall ignore this effect in our theoretical analysis of energy conversion in the chip (section b below), in which R_4 will be considered constant and equal to its value in single phase flow.

4. Results and discussion

4.1 Characterization of the entire system

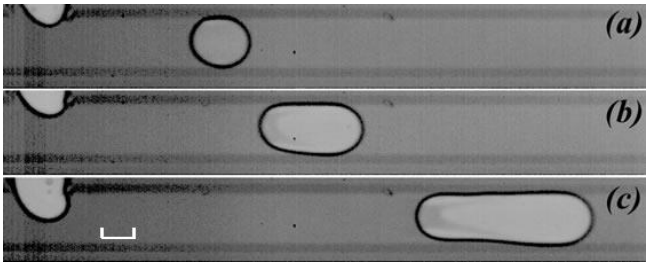

FIG. 2. Gas bubbles injected at gas injection pressure P_g = (a) 650 mbar, (b) 750 mbar, and (c) 900mbar. Bubble volume increases with gas injection pressure. The T junction is located at the top left of each figure. Scale bar in (c) indicates 20μm distance.

We maintained a constant inlet liquid pressure P_L = 1 bar in the gas-tight bottle connected to the liquid inlet tubing, and gradually increased the gas injection pressure P_g so as to introduce gas bubbles. Snapshots of gas bubbles were taken by a high-speed camera (Photron SA3). The volume of the gas bubbles was seen to increase with P_g (Figure 2). From the measured length, frequency and velocity of the gas bubbles, we estimated the gas volumetric flow rate and volume fraction, as discussed below. Since the gas volume fraction varies within the different sections of the system, we first discuss the electro-kinetic behavior of the entire system as a function of the measured gas inlet pressure P_g; then in section b we focus upon the chip, and consider the electro-kinetic behavior of 2-phase flow within the chip as a function of the estimated gas volume fraction f_g.

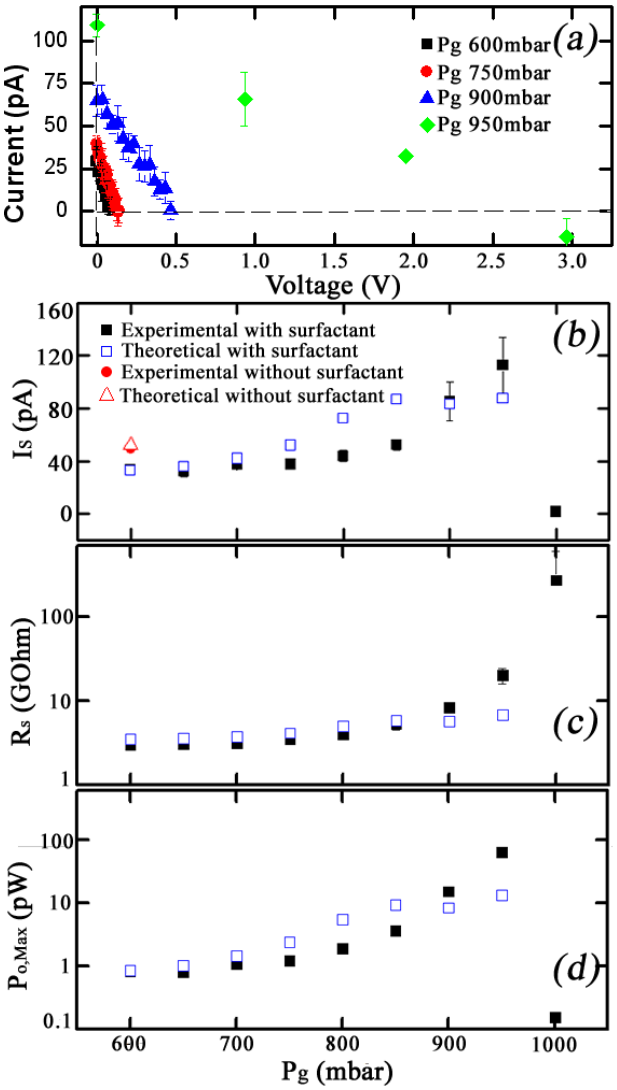

FIG. 3. (a) I-V characterization of the system during single-phase water flow (black squares) and two-phase gas/water flow (red, blue, green); (b) streaming current of system as a function of gas injection pressure P_g; (c) electrical resistance of system as a function of P_g; (d) maximum output power of system as a function of P_g. Open blue symbols indicate theoretical values.

To establish the maximum output power of the system, we performed an I-V characterization of the system by applying different voltages against the streaming potential between the electrodes, a procedure equivalent to introducing larger load resistances (see Figure 3a). When the voltage imposed across the electrodes was zero, the current in the external circuit I_{ext} equaled the streaming current of the system I_S. When the voltage was increased, I_{ext} decreased and the conduction current I_C (in the opposite direction to the streaming current) increased. When the current I_{ext} through the external circuit was reduced to zero, the conduction current balanced the streaming current and the applied voltage equaled the streaming potential U_S. We thus obtained the streaming current I_S, the streaming potential U_S and the electrical resistance $R_S = R_1+R_2+R_3+R_4 = U_S/I_S$ of the entire system. The maximum output power then follows from Equation (4). We will show that R_S, and consequently $P_{O,max}$, strongly increase following the introduction of bubbles.

At a gas injection pressure P_g=600 mbar no gas bubbles were generated. The streaming current in the resulting single phase flow was measured. The experimental data are shown as solid black squares on Figure 3b, whereas blue open squares indicate theoretical predictions. Results for single-phase flow indicated that in the solution of Tween 20 non-ionic surfactant the zeta potential on the microchip wall was -40 mV (solid black square and open blue square at P_g=600 mbar). Without surfactant the streaming current measured in 1 mM KCL solution indicates a zeta potential of –60 mV (solid red dot, together with open red triangleat P_g=600 mbar). The presence of Tween 20 thus decreases the zeta potential: a similar tendency has been observed for glass surfaces in soy bean protein [13] and in other non-ionic surfactant solutions [14]. Data points and error bars in Fig. 3(b) indicate averaged values and standard deviations from at least three independent experiments. The streaming current increased slowly with gas inlet pressure for P_g < 800 mbar and then more rapidly for P_g > 800 mbar. This increase is to be expected by equation (2): the pressure gradient in the chip is much larger than in the tubing (due to the smaller channel cross-section in the chip), and so the streaming currents I_{S2} and I_{S3} generated in the chip are much larger than I_{S1} and I_{S4} in the tubing. The increase of resistance R_3 by injection of gas bubbles makes the (high) streaming current in the chip dominant in equation 2, which leads to the observed streaming current increase of the system. At P_g = 950 mbar, I_S was

found to oscillate between 100 pA and 2 pA (approximately the values of I_{S3} and I_{S4}). We attribute this to random fusion of gas bubbles, and when P_g reaches 1000 mbar the continuous fusion of gas bubbles causes R_4 to dominate the electrical resistance of the entire system, so that I_{S4} (1.6 pA theoretically compared with 1.52 pA experimentally in single phase flow) becomes the measured system streaming current according to equation (2).

The predictions for the streaming current, electrical resistance and output power in Figure 3 (open blue squares) were obtained as follows. The ΔP over sections 1 and 2, which contain only water, can be predicted from the measured flow rate Q_L and the hydraulic resistance, which for the rectangular channel of section 2 is based on [15]:

$$Q = \frac{\Delta p}{64\eta L}\{wh^3[\frac{16}{3} - 3.36\frac{h}{w}(1 - \frac{h^4}{12w^4})]\} \quad (5)$$

The streaming current in sections 1 and 2 can then be estimated by equation (1). We assume that the streaming current generated by 2-phase flow in section 3 is the same as for single phase flow (as suggested by the results of section b below). Assuming that gas bubbles do not coalesce in the outlet tubing, the streaming current in section 4 changes little from that for single phase flow at the new flow rate(and I_{S4} is in any case so small that it has negligible effect in equation (1)). Changes in the electrical resistance R_4 of the section are negligible as long as P_g is sufficiently small for gas bubble coalescence not to occur. The electrical resistances R_1, R_2 of sections 1 and 2 are unchanged, and the electrical resistance R_3 of section 3, containing bubbles, is estimated using the bubble dimensions, as discussed in section (b) below. The total electrical resistance R_S of the system could therefore be predicted from the channel geometry and water conductivity and hence the streaming current of the entire system could be estimated by means of equation (2). Figure 3 shows the predicted streaming current, electrical resistance and output power (open blue squares).

The two phase flow electrical resistance R_S of the entire system was measured, as described above. Figure 3(c) shows that R_S strongly increased with gas injection pressure P_g. This is to be expected: as P_g increases, the volume of gas bubbles occupying the liquid channel increases and the conductive area of the channel is

reduced. It should be noted that theoretical prediction is smaller than the experimental value at high P_g. This is probably due to fusion of gas bubbles, which form slugs in the outlet tubing as already mentioned above, thereby increasing R_4.

We conclude that gas bubbles increase both the streaming current and the electrical resistance of the system. The maximum output power can be predicted from equation 4, using the resistance and streaming current measured when no bubble fusion occurred in section 4. When P_g= 950 mbar, $P_{O,max}$ was found to be greater than for single phase flow by a factor of 74.

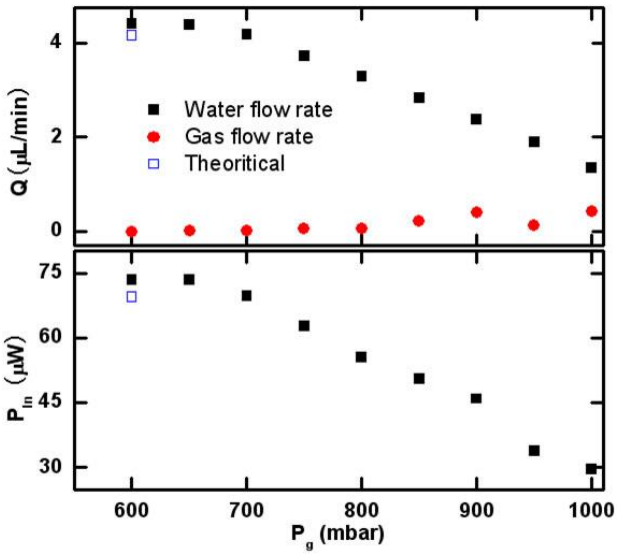

FIG. 4. (a) Gas flow rate Q_g (red) increases with increasing gas volume fraction and liquid flow rate Q_L (black) decreases. (b) The total input power P_{in} (defined by Eq.6) decreases when gas bubbles are injected into the liquid system.

To calculate the system efficiency, the input power P_{in} was determined as the sum of the gas input power and liquid input power:

$$P_{in} = \sum_i \Delta p_i \cdot Q_i = \Delta p_g \cdot Q_g + \Delta p_L \cdot Q_L \qquad (6)$$

The liquid flow rate Q_L was measured by a flow meter; the size and frequency of gas bubbles (and hence the gas flow rate Q_g) could be obtained from hi-speed camera movies. The volume of each gas bubble increased with the gas injection

pressure (Fig 2). At P_g=600 mbar no gas bubbles were generated, and Q_g=0. With increasing gas pressure, the gas flow rate increased, but the presence of gas bubbles led to a reduction in Q_L at constant liquid pressure. [16] Our experimental results indicate that Q_g was much smaller than Q_L, so that the total input power was dominated by the liquid phase according to equation (6).

Figure 4(b) shows that the input power gradually decreased with gas injection pressure, being halved at 950 mbar. Also shown is a theoretical prediction of the input power for single phase flow, calculated using equations (5) and (6).

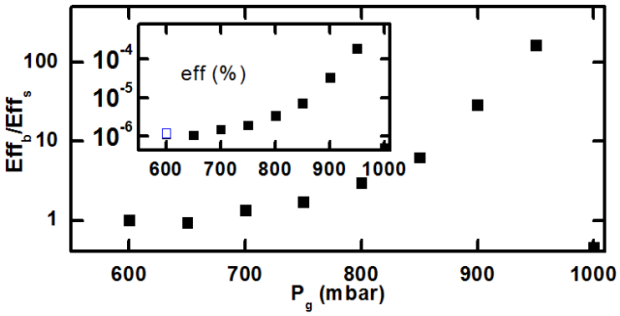

FIG. 5. The efficiency enhancement ratio (ratio of maximum efficiency in two-phase gas/water flow to that in single phase flow (Eff_b/Eff_S)). Inset figure represents the absolute value of the maximum efficiency.

The energy conversion efficiency (*Eff*) is the ratio of the maximum electrical output power $P_{O,max}$ to the mechanical input power P_{in}:

$$Eff = \frac{P_{O,Max}}{P_{in}} = \frac{I_S^{\,2} R_S / 4}{Q_g P_g + Q_L P_L} \tag{7}$$

The combined effect of increased maximum output power and decreased input power massively enhanced the system energy conversion efficiency by a factor 163 above that for single phase flow.

4.2 Characterization of the chip channel

The strong enhancement of the maximum electrical power output for the system as a whole is partly due to the increasing output power of flow section 3 (see figure 1)

and partly due to the increasing dominance of section 3 in the system efficiency. Both are caused by the introduction of bubbles and the resulting increase of R_3 (see equation 4). Since section 2 of the system (channel before T junction) is occupied only by single phase water, the gas bubbles do not influence its electrical resistance R_2. The part of the system of greatest theoretical interest therefore is the chip channel past the T-split where bubbles are injected. With suitable assumptions, discussed below, we can determine the increase of output power and efficiency for this section of the system separately. We can thus determine how the maximal output power and efficiency in a microfluidic channel are influenced by two-phase flow.

4.3 Electrical resistance increase by two phase flow

Gas bubbles decrease the conductive area of the channel, thereby increasing the channel resistance. To estimate this resistance, we neglect the spherical end-caps of the bubbles, and consider the contribution of the body of the gas bubbles.

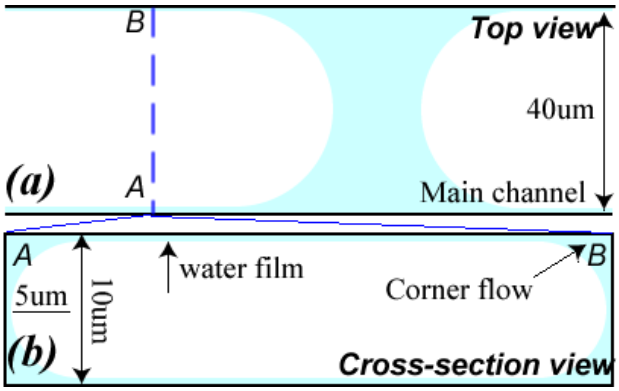

FIG. 6 A schematic (not to scale) of gas bubble flow in the channel of gas bubbles flowing in the main chip channel. Top view (a) and cross-section (b). The cross-sectional area of the liquid film near the wall can be ignored compared with the area of the liquid-filled corners.

A schematic gas bubble flow in channel is illustrated in Figure 6(a) and a cross-sectional view through a bubble is shown in Figure 6(b). The rectangular cross-section is an approximation of the actual channel shape, which has two corners rounded off as a result of the isotropic etching procedure for manufacturing. The

contribution of the liquid film near the wall to the conductive area can be ignored compared with the area of the liquid-filled corners, which was estimated as $h^2(1-\pi/4)$. From our calculation the conductive area (KCl solution) occupies 5.4% of the total cross-sectional area, which indicates that the resistance R_b per unit length of a bubble-filled channel will be about 18.6 times the resistance R_s of the solution-filled channel.

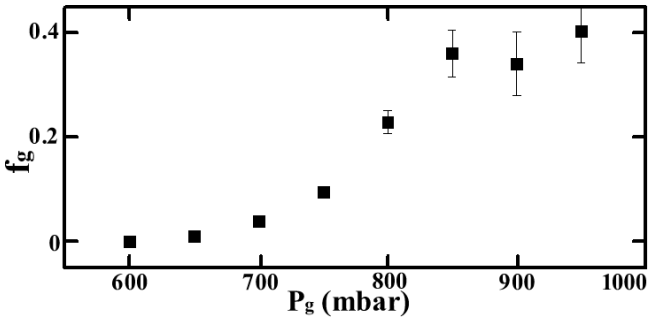

Fig 7. Observed gas volume fraction f_g as a function of gas injection pressure P_g. Error bars indicate the inhomogeneous gas bubbles.

From a movie of gas bubble flow, we measured the length (and hence the average volume) of the gas bubbles close to the T-junction. According to Boyle's law, the gas bubbles expand by a factor approximately 1.5 as they move from the T junction to the channel exit. We therefore assume the average length L_b of the gas bubbles to be a factor 1.25 greater than their length near the T-junction. The average bubble velocity u and generation frequency f were estimated from the movie, and the distance between the leading edges of two consecutive gas bubble was taken to be u/f. The number of gas bubbles (and liquid slugs of length $L_S=u/f-L_b$) in the channel of length L_S was therefore $n=L_3f/u$. We neglect the volume of the bubble spherical end-caps and the liquid volume in the corners, and estimate the gas volume fraction in section 3 as $f_g=nL_b/L_3$. The gas volume fraction in the liquid channel increases with gas injection pressure as shown in Fig 7. The error bars at higher pressure are caused by increasing variation in the generation process. At low gas injection pressure, the deviation of the bubble dimension is quite small; while at high gas injection pressure, the size variation of gas bubbles becomes larger. We attribute this to the random fusion of gas bubbles in the outlet tubing (section 4), which

causes feedback to the generation of gas bubbles via the fluidic resistance of the system. The total electrical resistance of section 3 of the channel was estimated as $R_3=(R_bL_b+R_SL_S)n=[R_bf_g+R_S(1-f_g)]L_3$. The predicted electrical resistance thus increases linearly with gas volume fraction f_g .

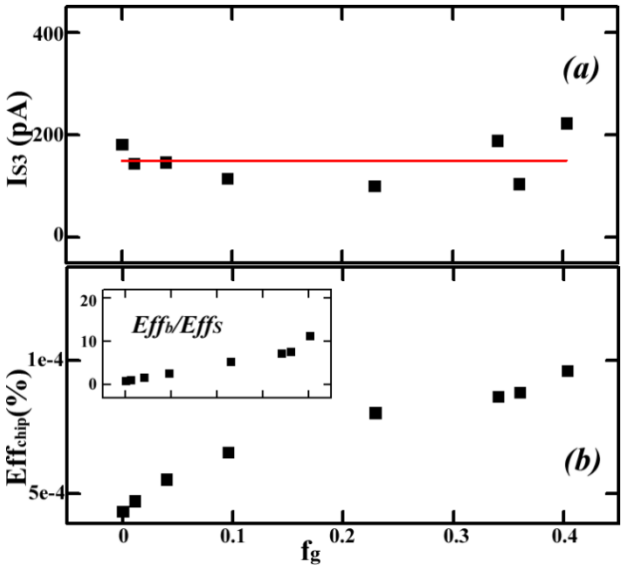

FIG. 8 (a) predicted streaming current I_{S3} in section 3 of the chip; the red line is a linear fit; (b) efficiency as a function of the gas injection pressure P_g; inset figure: efficiency ratio in section 3 (assuming a constant streaming current of 150 pA).

From the calculated resistance increase in section 3 and the experimental results for the resistance variation in the whole system, the streaming current in the chip channel past the T-junction I_{S3} could also be predicted using equation (2) for both single phase flow and two-phase flow. The result is shown in figure 8(a). As can be seen, the streaming current in section 3 stays almost constant and equal to the value in single phase flow.

We now take the average value of I_{S3} (150 pA) (figure 8a) and the theoretically derived value for R_3 as input for calculating the efficiency of section 3. To determine the efficiency of section 3, the input power for the section must be

estimated. Sections 1 and 2 contain only water flowing at the measured flow rate Q_L, so that ΔP_1 and ΔP_2 can be computed. Assuming gas bubbles remain small (no bubble fusion) the pressure drop ΔP_4 in section 4 can be approximated by that of water flowing at a volumetric flow rate Q_L+Q_g. The pressure drop over section 3 could therefore be estimated as $\Delta p_3 = \Delta p_L - (\Delta p_1 + \Delta p_2 + \Delta p_4)$. The liquid and gas flow rates are the same as those for the entire system (Fig. 4), so that the input power P_{in3} can be estimated as $P_{in} = \Delta p_3 \cdot Q_L + \Delta p_g \cdot Q_g$, with ΔP_g taken equal to the injection pressure P_g. By equation (7), we could then estimate the efficiency in section 3 as $Eff = I_{S3}^2 R_3 / 4P_{in3}$.

Taking a constant streaming current and an observed eight-fold increase of electrical resistance, we found that the total output power of section 3 was enhanced by 8 times with respect to single phase flow (figure 8b). (figure 8b). Moreover, due to the increase of the pressure drop over section 3 and the decrease of the liquid flow rate, the input power decreases slightly. Hence, the maximum efficiency of section 3 will increase 11.3 times with respect to single phase flow (figure 8b inset).

5. Discussion on efficiency

Though the absolute efficiency is strongly increased by the two phase flow, it is still very low in our system. There are several ways by which it might be increased. Methods adopted in single–phase flow are to reduce the salt concentration in the solution, thereby reducing its electrical conductivity, and to decrease the channel cross section.[17] An approach specific to our two-phase flow system would be to use cylindrical channels instead of rectangular ones. As shown in figure 6, in our chip the corners of the rectangular channels are always wetted by water, and provide a continuous path for electrical conduction even when the gas volume fraction is high. In a cylindrical channel the liquid film between the bubble and the capillary walls will be thin at low flow rates,[18] leaving only surface conductivity.[10] The electrical resistance R_b will therefore be larger, as will be the maximum power output.

6. Energy conversion by bubble flow in hydrophobic channel

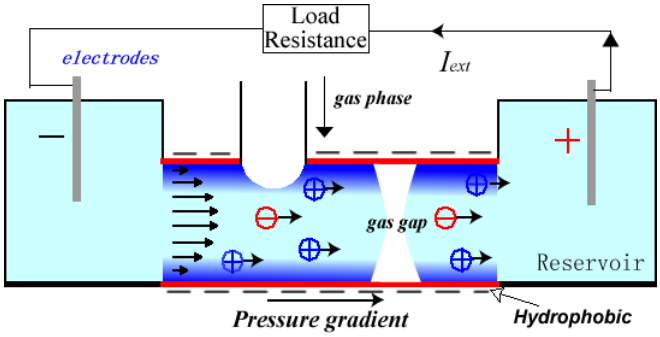

Figure 9 shows the principle of energy conversion by bubble flow in a hydrophobic channel. When gas bubbles penetrate in a hydrophobic channel, they will contact the channel surface. The aqueous solution as a result becomes totally isolated into pieces ('slugs') so that a gas gap is produced to totally prevent the conduction current in channel, thus increasing streaming potential and output power.

As discussed above, the corner flow of aqueous solution still leaves some space for ion transport, contributing to a conduction current of channel. To totally isolated the channel by gas bubbles, a hydrophobic channel was a good option to test. A 40μm wide and 25μm high borofloat microchannel was treated by FDTS (Perfluorodecyltrichlorosilane) to become hydrophobized. The fused silica tubing were not hydrophobized, so that the electrical resistance of tubing with bubbles wasn't increased much. 1mM KCl solution with adjusted pH 9.2 was used for aqueous phase. Gas phase (N_2) flow was applied in the side channel, to insert and isolate the water flow in the main channel. High speed images were recorded by Photron SA3 camera, and they clearly indicate a contact angle of more than 90 degrees as well as the fact that the water phase been cut into isolated slugs.

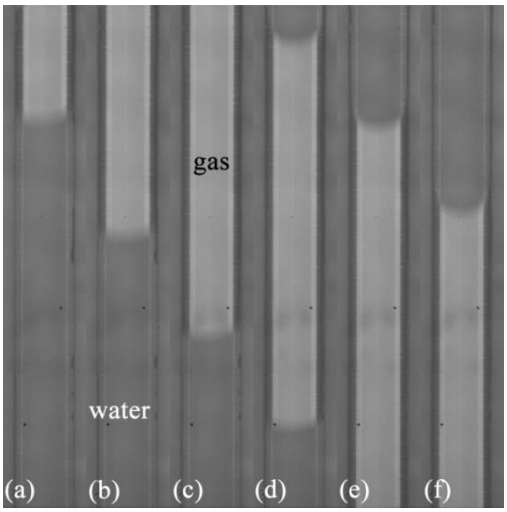

Figure 10 (a) – (f) indicate the gas bubble flow in the hydrophobic channel. Bright color indicates the gas bubble while dark area indicates the water phase. The time interval between images is 0.005s. The liquid inlet pressure during experiments stayed constant at 0.5bar and the gas pressure at 0.3bar.

When the gas phase penetrated the main channel occupied by the liquid phase, due to the hydrophobic surface, the gas bubble will contact the channel surface creating isolated water slugs. In figure 10 the refractive index (1.33) of water is quite close to glass (1.47), so that the brightness of the glass area (outside of the channel) is close to that of the liquid-filled channel. When gas occupied a part of channel, we can clearly see it became brighter. In addition, the channel side wall was tilted due to chemical wet etching. The background light source will be reflected more when it penetrates from glass to gas bubble at etched side wall with an angle close to 45 º. So, the area of side wall will be darker when the channel is gas occupied.

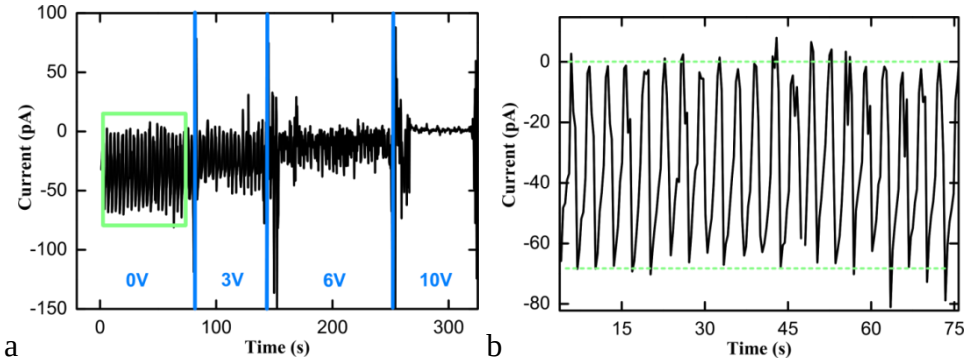

Figure 11 Electrical measurements with a single gas bubble in the hydrophobic channel as function of time. a) At different applied voltages. Blue solid lines separate the areas with different voltages applied to the system. B) The enlarged picture in the green square of figure a.

As we can see in figure 11a, the current oscillated as function of time. This is because there will be only single gas bubble penetrate in the liquid channel in time scaling, This indicates that the continuous current signals in single (water) phase and bubble flow in hydrophilic channel has been totally changed to "digital" signals. At 0V applied, the current oscillating from -65nA to 0nA (ground state) indicates that the current was produced when the water slug flowing through the channel was collected by electrode. However, the droplet frequency (9.3Hz) is higher than the measurement frequency limit in Keithley 6485 recording (2.7Hz) with the best noise level and as a result the current measurement is averaging and aliasing.

Different voltages are applied between the endings of system (including the fused silica tubing) to generate a conduction current and determine the streaming potential. As shown in figure 11a, the peak of oscillating current start to decrease with increasing external voltage. With 10 Volts applied on the system, there is almost no current flowing through, so that the streaming potential by use of a hydrophobic channel wall will be enhanced to 10 Volts.

The result indicates that the system resistance R_S increased about 100 times compared with single phase flow. Since the resistance in tubing is unknown, it is

very difficult to extract the electrical resistance R_{ch}. If we assume the there is no fusion of bubbles in the fused silica tubing and gas bubbles have no contribution on the electrical resistance of the tubing. According to equation (2), we can now calculate the maximum electrical resistance of the channel. The calculation will thus give the upper limit of the resistance increase inside the channel, which is over 300 times larger than single phase flow.

With the measured flow rate of 0.6 μL/min, we can now calculate that the enhancement of efficiency in a hydrophobic channel is 10 times with respect to single phase flow. The absolute efficiency is lower than 0.01%. (6×10^{-3}%) There are still more space to improve the efficiency since we still can use more diluted solution to increase Debye length and decrease system resistance, which can increase approximately two orders by using DI water. Another reason is we still need to decrease the dimension of liquid channel, so that the current density (per volume) will increase, then increase efficiency. A better design for water in gas flow (w/g) is required, such as using focusing flow. It might be possible to improve the stability of the gas gap generation in the system and make fraction of gas phase adjustable.

7. Conclusion

In conclusion, we successfully operated a two-phase flow streaming energy conversion system. Both the streaming current and the electrical resistance were increased by injecting gas bubbles and the output power and energy conversion were strongly enhanced. We analyzed our results in hydrophilic channels and extracted the energy conversion performance. In addition, hydrophobic channels were used, since this system can produce water slugs in a gas (w/g) flow. In the hydrophobic channels the water phase was separated into Slugs and an oscillating streaming current was observed. Streaming potential and output power were enhanced.

8. References

1. Hunter, R.J., *Zeta potential in colloid science: principles and applications.* Colloid science, 1981. **2**.
2. van der Heyden, F.H.J., et al., *Power generation by pressure-driven transport of ions in nanofluidic channels.* Nano Letters, 2007. **7**(4): p. 1022-1025.
3. Xie, Y.B., et al., *Electric energy generation in single track-etched nanopores.* Applied Physics Letters, 2008. **93**(16): p. -.
4. Linde, N., et al., *Streaming current generation in two-phase flow conditions.* Geophysical Research Letters, 2007. **34**(3): p. -.
5. Morgan, F.D., E.R. Williams, and T.R. Madden, *Streaming Potential Properties of Westerly Granite with Applications.* Journal of Geophysical Research-Solid Earth and Planets, 1989. **94**(B9): p. 12449-12461.
6. Antraygues, P. and M. Aubert, *Self Potential Generated by 2-Phase Flow in a Porous-Medium - Experimental-Study and Volcanological Applications.* Journal of Geophysical Research-Solid Earth, 1993. **98**(B12): p. 22273-22281.
7. Revil, A. and A. Cerepi, *Streaming potentials in two-phase flow conditions.* Geophysical Research Letters, 2004. **31**(11): p. -.
8. Sherwood, J.D. and E. Lac, *Streaming potential generated by two-phase flow in a polygonal capillary.* Journal of Colloid and Interface Science, 2010. **349**(1): p. 417-423.
9. Sherwood, J.D., *Streaming potential generated by a small charged drop in Poiseuille flow.* Physics of Fluids, 2009. **21**(1): p. -.
10. Sherwood, J.D., *Streaming potential generated by a long viscous drop in a capillary.* Langmuir, 2008. **24**(18): p. 10011-10018.
11. John. D. Sherwood, Y.X., Albert. van den Berg, Jan. C. T. Eijkel, *Theoretical aspects of electrical power generation from two-phase flow streaming potentials.* Microfluidics and Nanofluidics, 2013.
12. Daiguji, H., et al., *Electrochemomechanical energy conversion in nanofluidic channels.* Nano Letters, 2004. **4**(12): p. 2315-2321.
13. Malhotra, A. and J.N. Coupland, *The effect of surfactants on the solubility, zeta potential, and viscosity of soy protein isolates.* Food Hydrocolloids, 2004. **18**(1): p. 101-108.
14. Fagerholm, H.M., C. Lindsjo, and J.B. Rosenholm, *Physical Characterization of E-Glass Fibers Treated with Alkylphenylpoly (Oxyethylene) Alcohol Fibers Conditioned in Solutions of Different Ph.* Journal of Materials Science, 1995. **30**(9): p. 2420-2424.
15. Oosterbroek, E., *Modeling, Design and Realization of Microfluidic Components* 1999, University of Twente.

16. Vanapalli, S.A., et al., *Hydrodynamic resistance of single confined moving drops in rectangular microchannels.* Lab on a Chip, 2009. **9**(7): p. 982-990.
17. Stein, D., M. Kruithof, and C. Dekker, *Surface-charge-governed ion transport in nanofluidic channels.* Physical Review Letters, 2004. **93**(3)
18. Bretherton, F.P., *The Motion of Long Bubbles in Tubes.* Journal of Fluid Mechanics, 1961. **10**(2): p. 166-188.

Chapter 3

High efficiency ballistic energy conversion by a micro-jet

We report an electrostatic generator operating by a new principle to convert mechanical to electrical energy. The design is extremely simple as it contains no moving parts, solely consisting of a membrane with a single pore and a metal target. Conversion occurs in a two stage acceleration-deceleration cycle ('ballistic conversion'). Water is accelerated by mechanical energy of pumping it through a micropore to form a jet that breaks up into fast-moving charged droplets. Kinetic energy is then converted to electrical energy when the charged droplets decelerate in the electrical field that forms between membrane and target by collection of electrical energy. We demonstrate conversion efficiencies of up to 33%, opening up new perspectives for low-cost and robust renewable energy conversion.

Manuscript submitted

1. Introduction

In this chapter, we report on the performance of an energy conversion system based on a water microjet and find maximum conversion efficiencies of mechanical to electrical energy of 33%. The system is extremely simple as it contains no moving parts, consisting of a membrane with a single pore through which water is pumped and a metal target. Droplet kinetic energy is converted to electrical energy (‘ballistic conversion’) when charged droplets move in the electrical field generated between membrane and target. Since frictional losses can be limited, the efficiencies obtained are by far the highest for electrokinetic conversion systems and open up new perspectives for low-cost energy harvesting.

In 1992, Faubel and Steiner reported on large streaming currents obtained from high speed water microjets. [1] Aqueous solutions were forced through a metal membrane orifice under high pressure, forming a jet breaking up into droplets on exit in vacuum. The charged droplets were collected by a downstream target. More recently, Duffin and Saykally investigated this system for energy conversion, and found an energy conversion efficiency of almost 11%.[2, 3] They still employed a classical streaming potential model to interpret their data and as a result attributed the high efficiency found to the occurrence of entrance flow in the pore as well as to the electrical isolation offered by the air, preventing backflow of current as occurs in the classical electrokinetic energy conversion experiments referred to above.

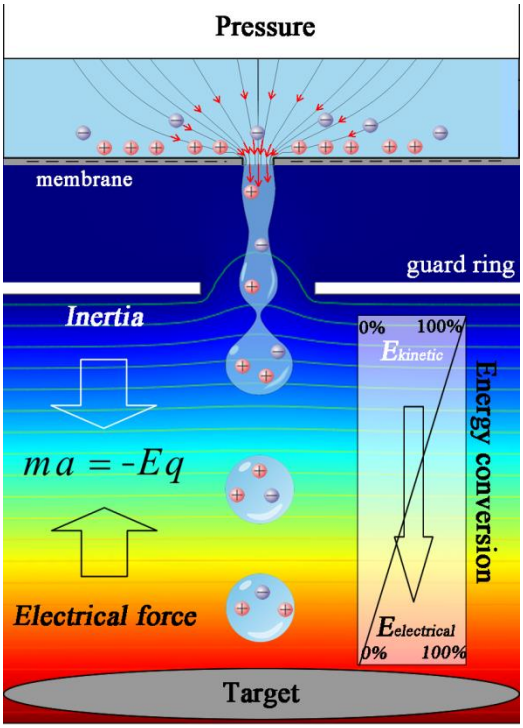

Figure 1 Conceptual illustration of the conversion principle. By application of pressure, water is forced through a membrane pore forming a microjet. The microjet, which is charged due to water transport through the electrical double layer at the membrane surface, breaks into droplets. On their trajectory through the air towards the metal target, the inertia of the droplets performs work against the electrical force, thereby converting kinetic energy to electrical energy.

Here we report that the conversion mechanism of a microjet-based system is radically different from streaming-potential based conversion processes and instead has some similarity with the Kelvin droplet generator. [4] However, instead of directly converting gravitational energy to electrical energy as the Kelvin generator does, it directly converts kinetic energy to electrical energy. Water is accelerated to a high speed (> 10 m/s) microjet by pressure-driving it through a micropore in a very thin (500 nm) membrane. The microjet breaks up into a stream of droplets which are charged due to the streaming current phenomenon or by induction using a guard ring at the pore exit. The droplets are decelerated by the electrical force during their air trajectory towards a high potential target, thereby converting inertia to electrical energy. Since the (mostly frictional) losses in the pore and air trajectory can be much more easily reduced than the frictional and electrical losses in the liquid ducts of classical streaming-potential based systems, much higher conversion efficiencies can be obtained. Interestingly, the procedure opposite to the one we apply, namely accelerating charged droplets by applied electrical fields, is well known. It is used for many and diverse applications such as electrostatic painting and printing[5], FACS (fluorescence activated cell sorting) [6], electrospray ionization[7] and colloid thrusters[8]. Here the first instance is provided where instead droplet inertia performs electrical work and use it for energy conversion. We term this principle ballistic energy conversion since the charged droplets can be seen as charge-laden projectiles that are ‘shot’ to a location of high electrical potential.

2. Materials and Methods

2.1 fabrication of Micropore chips

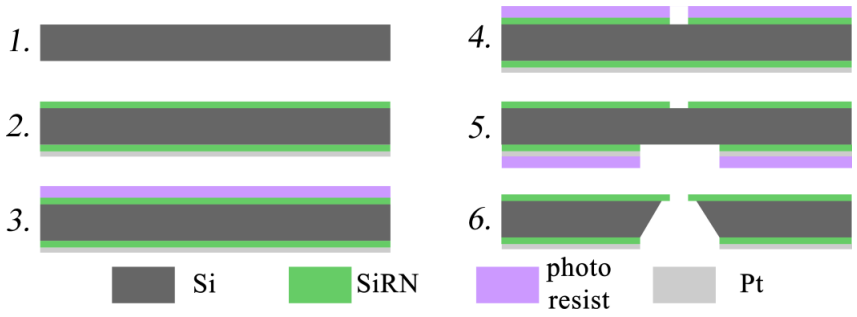

Figure 2. Fabrication workflow of pore chips

Figure 2 shows the fabrication work flow of the micropore chips. Plasma-enhanced chemical vapor deposition (PECVD) was used to grow a 500nm thick Silicon enriched Silicon Nitride (SiRN) membrane on a silicon wafer. Photoresist was spun on one side of the wafer and after photopatterning a single 10μm ID pore was etched through the SiRN membrane by reactive ion etching. Using the same photolithography a window was defined in the SiRN (1.5 by 1.5 mm) on the other side of the wafer. Then the wafer was immersed in a 25% KOH solution at 75 degree C for overnight, to ensure the wafer was etched through. Finally, the wafers were diced into small square chips (16.3mm×16.3mm). A photomicrograph and a SEM picture of a membrane pore are shown in figure 3.

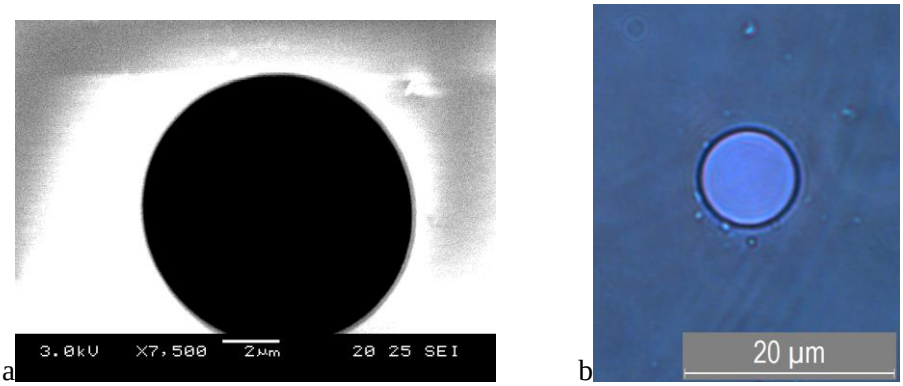

a b

Figure. 3. Scanning Electron Micrograph (left) and photomicrograph (right) of a 10 µm diameter pore in a SiRN membrane

Single chips were hydrophobized by first washing them with organic solvent (aceton and isopropanol) and subsequently DI water. They were then put into a vacuum chamber to evaporate all the water on the chips. A liquid solution of FDTS ((Heptadecafluoro-1,1,2,2,-tetra-hydrodecyl)trichlorosilane) was placed in the vacuum chamber and allowed to evaporate in the whole chamber. The chlorosilane groups will react with the SiRN surface making it hydrophobic, resulting in a typical contact angle between 90 and 100 degrees.

2.2 Setup

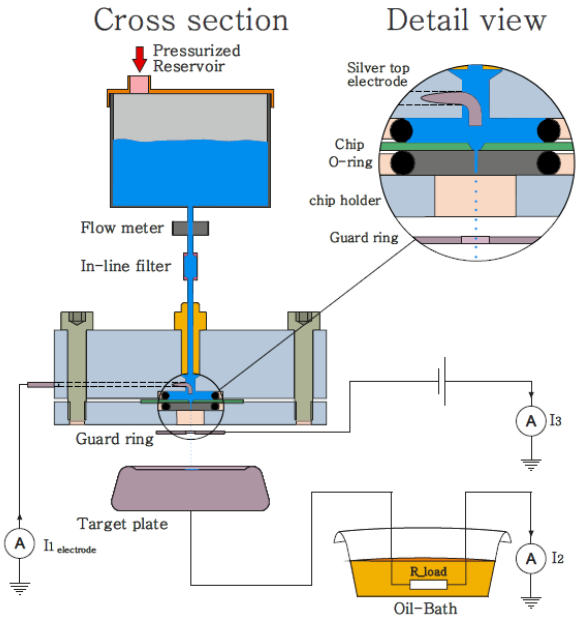

Figure 4 Schematic of the setup used. Ultrapure degassed water of pH 6.5 is pumped by 1.4 bar applied air pressure from a closed reservoir through a 10 μm diameter circular pore in a 500 nm thick silicon nitride membrane clamped in a holder. A grounded platinum wire electrode is inserted in the liquid inside the holder, close (~1 mm) to the pore opening. The exiting solution under the proper conditions forms a jet, after a certain length breaking up in droplets. The droplets travel through the air and land on a hollow stainless steel target placed at variable distance (typically 15 mm) from the pore opening. On the inside the target is connected to electrical ground via a high value load resistance (typically 1-10 TΩ). A metal guard ring with an opening of 2 mm diameter is placed at 1.5 mm from the pore exit, and maintained at ground potential. The current can be measured between ground and platinum reservoir wire (denoted I_1), between target and ground (I_2) and between metal guard ring and ground (I_3).

Figure 4 shows the schematic of our experimental setup. A silicon nitride membrane containing a single cylindrical pore with a diameter of 10 μm was mounted in a pressurized PMMA reservoir using rubber O-rings. The reservoir contained degassed ultrapure demineralized water of pH 6.5. A silver wire electrode (diameter 1 mm, inserted length 10 mm) was inserted in the top reservoir up to a distance of 1-1.5 mm from the pore opening and connected to ground via a pico-ammeter (Keithley 6485) to measure the current from ground to electrode (I_1). The water was expelled through the pore using a pressurized gas source (99% N_2) controlled with pressure regulator (Norgren R07-100-RNKG) and pressure sensor (Sensortechnics CTE 8016 GY7). A particle filter (2μm) was placed in the fluid line to exclude all particles that could block the pore. The volume flow rate of water was measured by a flow meter (Bronkhorst Mini Cori M12) in real time. The flow meter at the applied flow rates caused a pressure loss of about 0.07 bar, which was accounted for in the applied pressure. The flow rate in two experiments was measured by observing the displacement of the solution meniscus in a calibrated solution conduct inserted between reservoir and pump. A piece of aluminum foil (less than 0.1mm thickness) with a 2mm diameter hole was placed as metal guard ring at 1.5 mm from the pore exit to shield the jet from the electrical field generated between target and reservoir. The ring was maintained at ground potential. In some experiments the current was measured from ground to the ring (I_3) using a multi-meter in the voltage range. The droplets generated by the breakup of the liquid jet were collected on a hollow stainless steel target. The target was on the inside connected to a high-voltage cable (HSW Silicone cable) to prevent corona discharge. The cable was connected to ground via series-connected load resistors (six Ohmite 1TOhm resistors, four 400GOhm resistors and four 500GOhm resistors). The resistors were used in different combinations to regulate the target potential, which was determined according to $V_{target}=I_2 \times R_{load}$. The resistors were immersed in insulating oil (Shell Diala S2-ZU-I) to prevent losses by corona discharge. A Teflon plate was furthermore placed in the oil bath to prevent the resistors from contacting each other. Another Teflon table was placed under the oil bath to isolate the bath from the Faraday cage. At the grounded terminal a series-connected pico-ammeter (Keithley 6487) measured the current (I_2) from target to ground.

Three types of resistors were used in the experiments: six resistors with a nominal resistance of 1TOhm (Ohmite MOX-3-12, 10% accuracy; 30kV voltage rating), four 400GOhm resistors and four 500GOhm resistors (Ohmite RX-1M Hi-Meg) with a 1% accuracy and 1kV voltage rating (1.5kV in a dielectrical oil bath). The resistance of every resistor was calibrated separately using a Keithley source meter and Keithley pico-ammeter for high accuracy (Table 1).

Table 1 *The values of the resistance found by calibration*

Number	type	Resistance (TOhm)	Voltage rating (kV)	Power rating(W)
1	MOX-3-12	1.08	30	7.5W
2	MOX-3-12	1.07	30	7.5W
3	MOX-3-12	1.08	30	7.5W
4	MOX-3-12	1.00	30	7.5W
5	MOX-3-12	0.99	30	7.5W
6	MOX-3-12	1.06	30	7.5W
7	RX-1M Hi-Meg	0.40	1.5 (in Oil)	0.5W at 25℃
8	RX-1M Hi-Meg	0.39	1.5 (in Oil)	0.5W at 25℃
9	RX-1M Hi-Meg	0.40	1.5 (in Oil)	0.5W at 25℃
10	RX-1M Hi-Meg	0.40	1.5 (in Oil)	0.5W at 25℃
11	RX-1M Hi-Meg	0.50	1.5 (in Oil)	0.5W at 25℃
12	RX-1M Hi-Meg	0.50	1.5 (in Oil)	0.5W at 25℃
13	RX-1M Hi-Meg	0.50	1.5 (in Oil)	0.5W at 25℃
14	RX-1M Hi-Meg	0.49	1.5 (in Oil)	0.5W at 25℃

3. Experimental results and Analysis

Figure 4 shows the setup used, and figure 1 conceptually illustrates the conversion principle. The typical experimental data shown in figure 5a are traces of the current from ground to the reservoir electrode ('upstream current' I_1) and the current measured from the metal target to ground ('downstream current' I_2). At t = 230s pressure is applied to the system and jetting starts, creating a stream of droplets impacting on the target. Current I_1 directly reaches a stable value of 3.9nA, while I_2 exponentially increases to 3.3nA, the exponential increase being determined by the RC time of the target capacitance and load resistance. The steady state difference between both currents which is seen in this case is caused by loss of charged droplets, which can have various causes as will be discussed later. In a typical experiment the value of I_2, once stable, is recorded after which the load resistance is changed to a new value, at which again the steady state currents are recorded. Figure 5b displays currents I_1, I_2 and I_3 (the current through the guard ring, which in this case is grounded) against load resistance for a typical measurement sequence. It is seen that I_1 remains approximately constant, while the harvested current I_2 decreases with load resistance and the current through the guard ring increases from initially zero to higher values. The target voltage can be calculated from the harvested current I_2 and the value of the load resistance as $V_{target} = I_2 R_{load}$ and is plotted against the load resistance in figure 5c. It is seen to increase with load resistance up to a value between 10 and 12 kV where it saturates to a value which does not show a clear relation to the upstream current. For a typical current density of 5 nA and a typical initial droplet diameter of 20 μm, each droplet carries about 10^5 elementary charges. Since demineralized water is used and a positive current is obtained, the charges must be provided by an increase in the proton concentration and a decrease in the hydroxyl ion concentration in the droplets. It can be calculated that this will result in a slight decrease of the droplet pH with 0.1 unit to about pH = 6.4. Notably, the charge per droplet is 100 times less than the Rayleigh limit, which describes the droplet charge at which Coulomb repulsion will overcome surface tension and the droplet will become unstable. It can be calculated as $8\pi (\sigma\varepsilon_0 d^3)^{1/2}$ Coulomb, where σ is the surface tension (0.07 N/m), ε_0

the permittivity of free space and d the droplet diameter. [9, 10] During the experiments the guard ring was grounded.

The experimental conversion efficiency is $eff = I_2 V_{target}/p\,Q$, where p (Pa) is the applied pressure and Q (m^3/s) the volume flow rate. Figure 5d plots the conversion efficiency obtained in different experiments as a function of load resistance. The conversion efficiency is seen to increase with load resistance, with typical experiments showing maximal efficiencies of around 30% with the highest value reached in all experiments 33%. Figure 5e plots the conversion efficiencies in an alternative way, namely against target voltage, this time as a function of the charge density of the droplets in order to correct for variations in the flow rate (charge density = $q/m = I_1/(Q\,\rho)$, where ρ is the specific weight of water). It is seen that a higher droplet charge density allows reaching high efficiencies at lower target voltages. The observed data are in accordance with the theoretical predictions shown in the graph which will be discussed later. The distance between pore and target is also of influence to the efficiency obtained, since it will change the droplet air friction. Figure 5f show the currents I_1 and I_2 in a typical experiment as a function of distance between pore and target, at constant load resistance. Below a distance of 7mm arcing occurred between ring and target, strongly reducing I_2. Up to a distance of 10mm occasional arcing would still reduce I_2. Above this distance a maximal I_2 was reached. At distances of more than 15mm I_2 was found to decrease again, vanishing at a distance of 40mm. At these distances most of the droplets were seen to be reflected from the target. The efficiency obtained in this experiment is shown in figure 5g, and reaches a peak at a distance of 15mm. The upstream current was found to differ between experiments. As shown in figure 5e, higher upstream currents are favorable since they reduce the target voltage needed to reach a certain efficiency.

Membrane thickness	500 nm
Pore diameter	10 μm
Droplet diameter	20 μm
Applied pressure	1.5 bar
Flow rate	1 μL/s
Initial droplet speed	10 m/s
Droplet deceleration towards target	$5 \cdot 10^{3}$ m/s^{2}
Distance to target	15 mm
Current	5 nA
Target voltage	7.5 kV
Field	500 kV/m
Droplet charge	10^{5} e
Charge/mass	$5 \cdot 10^{-3}$ C/kg
Droplet frequency	250 kHz

Table 2 Typical experimental parameters. Ultrapure vacuum degassed water was used (pH 6.5).

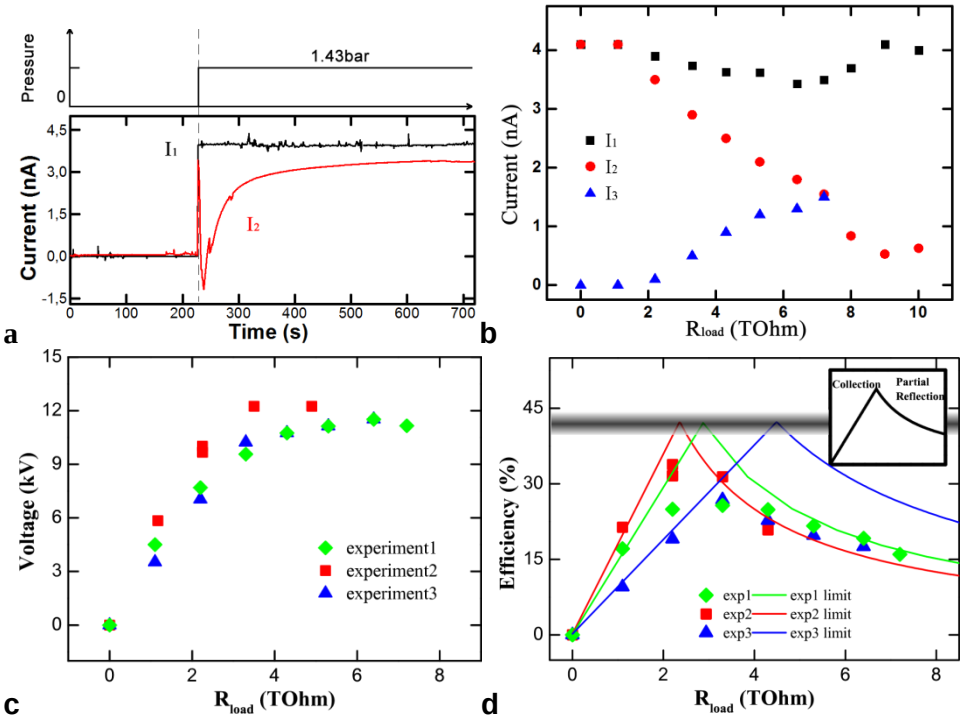

Fig. 5A. Upstream and downstream current on application of pressure. The guard ring was grounded during this experiment. B. Upstream, downstream and guard ring current with increasing value of the load resistance. C. Generated target voltage as function of load resistance for different upstream currents. D. Conversion efficiency as function of load resistance for different values of the upstream current. Experimental values (symbols) as well as theoretical predictions (lines) are shown, as well as the theoretical maximum efficiency of 40%(average) by the grey area. The variation of the maximum theoretical efficiency is due to differences of flow rate the in measurements, inducing variations of the droplet speed.

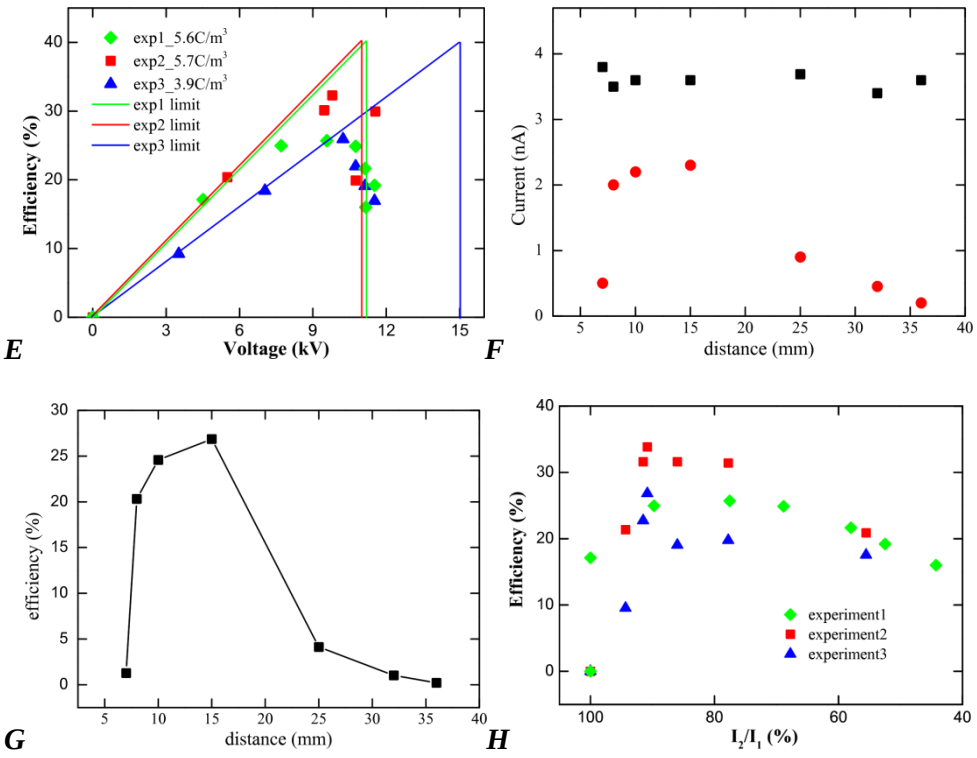

Fig. 5E Conversion efficiency as function of target voltage for different values of the droplet charge density (= $I_1/(Q\,p)$ compared to theoretical predictions of the maximum efficiency. F. Upstream current I_1 (black) and downstream current I_2 (red) as function of the distance between pore and target. G. Conversion efficiency as function of the distance between pore and target. H. The efficiency as a function of the ratio of harvested and upstream current for the different experiments.

The measurement data can be interpreted as follows. At pH 6.5 the silicon nitride surface of the membrane is negatively charged due to dissociation of surface-bound groups, chiefly silanol groups. [11] The electrical double layer formed has a typical thickness of 300 nm in 10^{-6} M 1:1 electrolyte solution. The solution that flows towards the pore and that ultimately forms the jet, partly passes through the electrical double layer on the membrane surface close to the pore opening which layer contains an excess of positive charge. The current through the pore that is thus generated is equivalent to a streaming current and we will further refer to it in

that way. The pore region in a functional description now is a *charge gate* for passage of positive ions and the current that flows through the pore is positive in the direction of solution flow. Upstream in the reservoir this current is provided at the grounded platinum wire electrode by redox reactions occurring. The solution that exits the pore forms a jet at sufficient velocity, which after a certain length breaks up into droplets due to the Rayleigh-Plateau instability.[12, 13] On their trajectory to the target, air isolates the charged droplets and prevents conductive backflow of charge. During this trajectory the droplets of mass m and charge q_d move through the electrical field E between pore and target that exerts a force on their ionic charge in a direction opposite to their direction of movement. For the moment neglecting frictional forces, the force balance on this trajectory is given by inertia and the electrical force

$$ma = -q_d E$$

On the droplet trajectory, the work done by the electrical force against inertia as described by this force balance converts kinetic energy to electrical energy. The electrical field E originates from the electrical charging of the metal target by the arriving droplets. The steady state magnitude of the target electrical potential is thereby determined by the value of the current and the load resistance through which the target is connected to ground potential. Describing the system behavior, we can distinguish a first regime at low values of the load resistance (and hence low target potential $I_2 R_{load}$), where the kinetic energy of the droplets is incompletely converted to electrical energy. As a result all droplets arrive at the target with some kinetic energy left and currents I_1 and I_2 are equal (figure 5b). In this regime the target potential increases linearly with the load resistance, $V_{target} = I_2 R_{load} = I_1 R_{load}$. (figure 5c) and this also holds for the efficiency $eff = (I_2)^2 R_{load}/p\ Q$ (figure 5d). Since I_1=I_2, the initial slope of the theoretical predictions of the maximum efficiency in figure 5d equals $(I_1)^2/(p\ Q)$ and higher upstream currents I_1 will result in a steeper slope. This reflects the fact that a droplet with a higher charge to mass ratio q/m will feel a stronger electrical force converting its kinetic energy to electrical energy. We found that I_2 already becomes smaller than I_1 before the maximum voltage and efficiency were reached. We ascribe this to a

variation in the charge over mass ratio of the droplets, *q/m*. Figure 5h shows that the maximal efficiency generally is reached when $I_2/I_1 \approx 0.85$. This implies that about 20% of the droplet charge is not harvested, causing the efficiency to fall below 40%.

At some value of the load resistance, the target reaches a potential where the kinetic energy of the droplets is exactly sufficient to reach it. We will call this the optimal target potential, V_{opt}, at which all kinetic energy is converted to electrical energy and maximum efficiency is obtained. The theoretical optimal potential (and corresponding resistance value R_{opt}) will depend on the cumulative losses occurring in the process which will described further in this paper and in the supporting information. The measured optimal potential can differ from the calculated one because additional loss processes such as corona discharge from the target can occur. For the system reported in this paper, theory estimates that cumulative losses are about 55% of the input energy, so that the maximal theoretical efficiency is 40%. Above the optimal target potential droplets are partly reflected from the target (figure 6) and a second operating regime begins. In this regime V_{target} is seen to remain approximately constant (figure 5c) and I_2 is observed to become increasingly smaller than I_1 (figure 5b). The loss of charged droplets represented by the difference I_2-I_1 implies that the efficiency decreases in this regime. The magnitude of this decrease can be theoretically predicted by the condition that V_{target} remains equal to V_{opt}, since this represents the potential at which droplets have exactly sufficient kinetic energy to reach the target. Since $V_{target} = I_2 R_{load}$, I_2 will be inversely proportional to R_{load} at resistance values above R_{opt}. The efficiency in this 'droplet loss' regime is then equal to $(V_{opt})^2/(R_{load}\, p\, Q)$. Figure 5d shows the theoretical predictions of the efficiency in this regime as well as the measured efficiencies. Both are in satisfactory agreement. It is obvious that the measured efficiencies are mostly lower than the theoretical maxima. We attribute this to excess current losses due to corona discharge, occasional arcing between target and guard ring, and instability of the liquid meniscus of the water collected on the target leading to electrospraying.[14-16] Water collecting on the guard ring also decreased the effective distance between guard ring and target and thereby led to increased arcing.

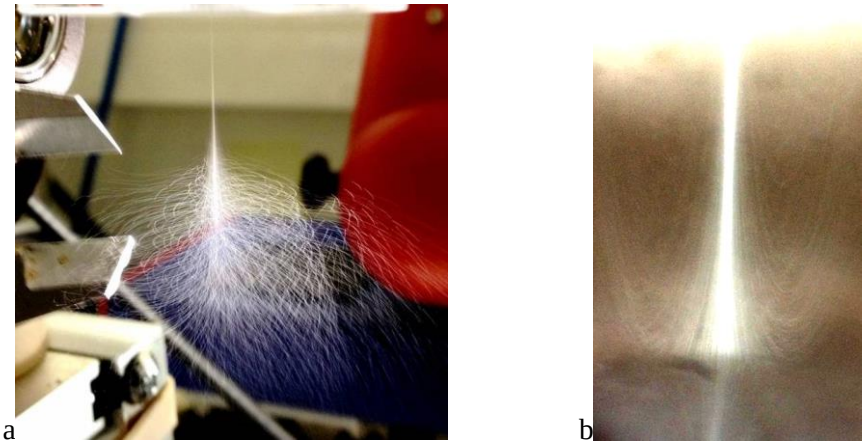

a b

Figure 6. Water jet shooting in open air (left) and onto the target (right). a shows the water jet shooting in the open air. The droplet train close to the pore exit was quite narrow, and widened at a larger distance from the pore. For this configuration we ascribe the widening of the droplet train to consumption of the kinetic energy of droplets by air friction followed by droplet diffusion. b. shows a close-up of the droplet train impacting the target. In this case the target potential was above the optimal potential V_{opt} and the droplets were partly reflected from the target.

The field along the droplet path is expected to be largely uniform, with its exact shape determined by the target shape and the shape of the grounded guard ring placed close to the pore exit. This ring will electrically shield the jet from the electrical field and prevent a decrease of droplet charge by field feedback. The target is placed as close to the ring as allowed by dielectric breakdown through the air, which typically is at about 15 mm distance. A shorter distance is favorable as it will decrease air friction. An optimal conversion of kinetic to electrical energy is obtained when the load resistance and hence the target voltage are such, that the velocity of the droplets on target impact is exactly reduced to zero. Figures 5f and 5g show the dependence of the downstream current and the efficiency on the distance between pore and target at a fixed value of the load resistance. At small distance the kinetic energy is incompletely converted to electrical energy, and the

droplets arrive with considerable kinetic energy on the target. At larger distance an optimum is reached, when all kinetic energy is converted. At still larger distances the air friction of the droplets starts consuming a larger and larger part of the kinetic energy, resulting in a decrease of the number of droplets arriving at the target (represented by I_2) and hence a lower efficiency. Gravity can be safely neglected in the considerations since the gravitational energy over the typical trajectory length of 1 cm is equivalent to less than 0.1% of the typical applied pressure of 1.4 bar.

Energy loss – main factors

Multiple loss factors can be identified in the conversion process. To discuss them we will distinguish two consecutive conversion stages. The first stage concerns all electrohydrodynamic processes up to and including droplet formation. The input power $P_{in} = p\,Q$, with p the applied pressure and Q the resulting flow rate. Around the pore entrance and during pore passage energy is lost to hydrodynamic friction. Subsequently energy is needed for the formation of the droplet air/water interface. This interfacial energy is converted to thermal energy on impact with the target and lost. Together these factors decrease the efficiency of the first conversion stage, Eff_1, defined as the ratio of droplet kinetic energy power P_{kin} over input power.

The second stage concerns the losses occurring during the air trajectory of the droplets and the conversion of ionic to electronic current at the target. The harvested electrical power $P_{el} = V\,I_2$, where V (V) is the target potential and I_2 (A) the electrical current flowing through the load. Assuming that no kinetic energy is left on impact, we can define the efficiency of this second stage as $eff_2 = P_{el}/P_{kin}$. The conversion efficiency of the entire process can be obtained by multiplying the efficiencies of the two separate stages: $eff = eff_1\,eff_2$.

Energy loss – minor factors

Minor losses in stage 1:

Power is also consumed for transport of the electrical current, which is determined by the resistance to charge transfer at the electrode/water interface and the power consumed for current conduction in the solution (Ohmic loss). However, we estimate these losses to be negligibly small under the operating conditions. The voltage needed for electrolysis of water namely is only about 2 V. Furthermore an upper limit to the Ohmic potential drop can be calculated as the potential drop over a truncated cone with 1mm top diameter (the Pt wire electrode) and 10 μm bottom diameter (the pore) and a length of 1 mm (the distance between wire electrode and pore). For a solution conductivity of 0.18 MΩm and a current of 5 nA this voltage drop is approximately 100V. Both values are negligible compared to the total voltage drop of about 10kV.

Minor losses in stage 2:

Air friction losses were modeled by a friction model based on Stokes' law for the air friction, the electrical force qE and Newton's second law. The resulting efficiency of the second stage, Eff_2, was 90% for a target distance of 15mm.

Other losses in stage 2 include Ohmic losses in the water covering the target, the resistance to charge transfer at the target/water interface and corona discharge and electrospraying from the target when at high potential and electrical losses to maintain the guard ring at constant potential.

The Ohmic and charge transfer losses can be neglected in view of the fact that both the voltage needed for electrolysis of water (about 2 V) and the voltage drop in the water over the large target area are negligibly small compared to the total voltage drop of about 10kV. The losses due to corona discharge and electrospraying finally occur occasionally at short distances and will not be considered in this analysis.

When current flows through the guard ring, I_3, it forms part of the total loss of charged droplets and therefore represents no extra loss.

Coalescence between droplets was observed during the droplet flight process, and will lead to loss of kinetic energy. This loss was estimated from the size and velocity distribution, and calculated as less than 2%.

4. Further discussion

The conversion method we demonstrate has interesting parallels with the Kelvin droplet generator (or 'Kelvin's thunderstorm').[4, 17] The Kelvin droplet generator generates electrical energy from gravitational energy, when charged droplets fall down from a reservoir towards a receiving vessel at high electrical potential. The receiving vessel gradually acquires this high potential due to the collective droplet charges received. To charge the droplets the principle of electrical induction is applied. To do this, there are actually not one but two separate droplet streams exiting from the same reservoir. The droplets are collected in two receiving vessels, whereby each vessel is connected to an induction ring located close to the other droplet stream exit. In Kelvin's droplet generator the action of gravity on the droplets is during the droplet trajectory continuously opposed by the electrical force, thereby converting gravitational energy to electrical energy. It thus by principle differs from our generator where during the droplet trajectory inertial force is opposed by electrical force and kinetic energy is converted to electrical energy, which we term ballistic conversion.

Practical applications of a ballistic conversion device can be in areas where high voltages are needed in stand-alone applications such as in high-voltage microfluidics. The extremely simple structure of the device carries the promise of low maintenance. Also, in several ways it can be further developed by engineering. The current obtained can be increased, and the necessary load impedance decreased, by increasing the number of pores. This is simply possible using micromachining techniques. [18] Ten thousand pores for example will increase the harvested current to 50 μA and decrease the load impedance to 10 MΩ, values suitable for microchip capillary electrophoresis. [19] For application in other areas it will be helpful if the generated voltage can be reduced. At present we demonstrated 20% efficiency at 6kV by a current of 5 nA. The Rayleigh limit as discussed above in principle still allows about 100 times higher droplet charge over mass ratios, *q/m*,

in the present device, which would result in an operating voltage of 60 V. Induction charging as we already applied is one of the possible ways to increase *q/m*, but also use of other solvents or ionic liquids such as applied for colloid thrusters.[8] Further engineering targets can be to reduce the hydrodynamic pore resistance and the air resistance, for example by working under partial vacuum. Finally continuous operation in a small package will necessitate incorporating structures for collection and recycling of the water inside the device. A wide variety of potential applications such as energy conversion, FACS sorting, inkjetting, and micropropulsion may benefit from gained insight.

5. Conclusion

In this chapter, we demonstrate a simple and straightforward method of energy harvesting from liquid microjet, termed "ballistic energy conversion". The water is pushed out of a single micropore and forms a liquid microjet containing net charges from the electrical double layer. Due to the Rayleigh Plateau instability, the jet breaks up into droplets which contain net charge. The droplets move with high kinetic energy, and deliver charge to a bottom target. A high electrical potential can be produced at the target via resistors connecting the target to ground, so that droplets move against the electrical field created and convert kinetic energy to electrical energy. A maximum efficiency of 33% was found in our experiments. The distance between guard ring and target was also found to be important. In our experiment, the optimal working distance between target and membrane was found to be around 15mm. mainly due to the inhomogeneous charge to mass ratio of the droplets, we found that the maximum efficiency was achieved when $I_2/I_1 \approx 0.85$.

6. References

1. Faubel, M. and B. Steiner, *Strong Bipolar Electrokinetic Charging of Thin Liquid Jets Emerging from 10 Mu-M Ptir Nozzles.* Berichte Der Bunsen-Gesellschaft-Physical Chemistry Chemical Physics, 1992. 96(9): p. 1167-1172.
2. Duffin, A.M. and R.J. Saykally, *Electrokinetic Power Generation from Liquid Water Microjets.* Journal of Physical Chemistry C, 2008. 112(43): p. 17018-17022.
3. Duffin, A.M. and R.J. Saykally, *Electrokinetic hydrogen generation from liquid water microjets.* Journal of Physical Chemistry C, 2007. 111(32): p. 12031-12037.
4. Thomson, W. Vol. 16. 1867: Proc. Roy. Soc. London.
5. Castle, G.S.P., *A Century of Development in Applied Electrostatics; Nothing Static Here*. Vol. 18. 2011, IEEE Trans. on Dielectr. and Electr. Insul. 1361-1365.
6. Julius, M.H., T. Masuda, and Herzenbe.La, *Demonstration That Antigen-Binding Cells Are Precursors of Antibody-Producing Cells after Purification with a Fluorescence-Activated Cell Sorter.* Proceedings of the National Academy of Sciences of the United States of America, 1972. 69(7): p. 1934-&.
7. Fenn, J.B., et al., *Electrospray Ionization for Mass-Spectrometry of Large Biomolecules.* Science, 1989. 246(4926): p. 64-71.
8. Chiarot, P.R., P. Sullivan, and R. Ben Mrad, *An Overview of Electrospray Applications in MEMS and Microfluidic Systems.* Journal of Microelectromechanical Systems, 2011. 20(6): p. 1241-1249.
9. Peters, J.M.H., *Rayleigh's electrified water drops.* Eur. J. Phys., 1980. 1: p. 143.
10. Taflin, D.C., T.L. Ward, and E.J. Davis, *Electrified Droplet Fission and the Rayleigh Limit.* Langmuir, 1989. 5(2): p. 376-384.
11. Bousse, L. and S. Mostarshed, *The Zeta-Potential of Silicon-Nitride Thin-Films.* Journal of Electroanalytical Chemistry, 1991. 302(1-2): p. 269-274.
12. van Hoeve, W., et al., *Breakup of diminutive Rayleigh jets.* Physics of Fluids, 2010. 22(12).
13. C.Weber, Z. Angew. Math. Mech. , 1931. 11: p. 136-154.

14. Taylor, G., *Disintegration of Water Drops in an Electric Field.* Proc. R. Soc. Lond. A, 1964. 280(1382): p. 383-397.
15. *See Section 4.*
16. Eggers, J. and E. Villermaux, *Physics of liquid jets.* Reports on Progress in Physics, 2008. 71(3).
17. Melcher, H.H.W.a.J.R., *Electromechanical dynamics*1968: John Wiley and Sons, New York.
18. Kuiper, S., et al., *Development and applications of very high flux microfiltration membranes.* Journal of Membrane Science, 1998. 150(1): p. 1-8.
19. Blanes, L., et al., *High-voltage power supplies to capillary and microchip electrophoresis.* Electrophoresis, 2012. 33(6): p. 893-898.

Chapter 4

Theoretical investigation on ballistic energy conversion system

The ballistic energy conversion is calculated and analyzed both in theoretical and experimental aspects in this chapter. The energy conversion process is divided into two steps: the acceleration step from pressure to kinetic energy of the micro droplets, and the deceleration step from kinetic energy of droplets to electrical energy. Theoretical simulation predicts the energy loss factors in this acceleration-deceleration circle, and matched nicely with the experimental data obtained using two pore sizes. The upper limits of theoretical efficiency and optimal operational conditions are also predicted in this chapter.

Manuscript to be submitted

1. Introduction

As we described in the previous chapter, in a ballistic energy conversion system a liquid microjet is formed which breaks into charged droplets transporting charge through the air to the target. Subsequently electrical energy can be harvested by resistors, connected between target and ground. Duffin and Saykally first used the liquid jet to harvest electrical energy with nearly 11% efficiency.[1, 2] They attributed the enhancement of efficiency compared to classical electrokinetic conversion to the entrance flow near the thin orifice, and the fact that droplets are isolated in the air so that no conduction current can be generated from the bottom target.

Our analysis in the previous chapter shows that the energy conversion in such systems is different from traditional energy conversion by the streaming potential, and our experimental results show the maximum efficiency can be over 30%. The analysis in the previous chapter can be summarized as follows. Pressure pushes water through an orifice forming a jet. Due to the Rayleigh-Plateau instability[3], the water jet will break up into droplets, containing net charges from the electrical double layer (EDL). The charged droplets are collected at the target, creating a current and generating an electrical potential through a high ohmic (several Tera Ohm) resistance. The created potential will slow the charged droplets down, because they move against an electrical field. The kinetic energy of the droplets can overcome the force exerted by this electrical field. Now essentially the pressure mechanical energy is converted to electrical energy via kinetic energy. Because the basic system consists of only a membrane with micropore and a target, this is a simple and straightforward method to convert mechanical energy to electrical energy.

However, a quantitative analysis is needed for the ballistic energy conversion system, so that we can have a better understanding of the limits of the system and predict what the optimal operational conditions are for the conversion efficiency. In this chapter, we construct a theoretical model for the energy conversion system, and predict where the system still can be improved.

In this chapter we experimentally investigate the droplet speed as function of trajectory distance, applied pressure and analyze the energy loss in the two steps. We simulate the viscous losses in the micropore, and the air friction loss of droplets in air. Finally we predict the direction of efficiency improvement and the theoretical limit of the efficiency.

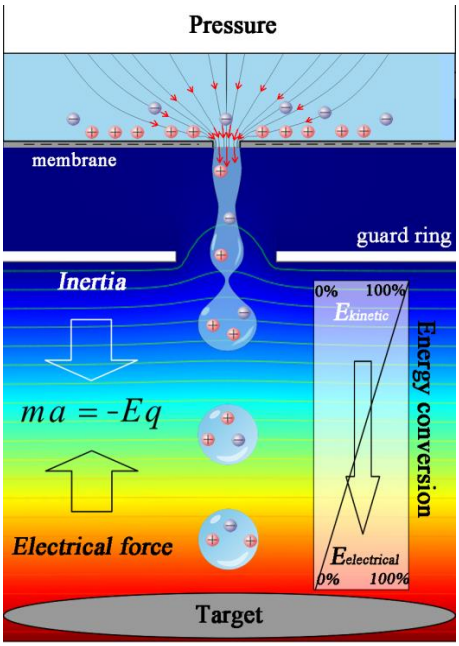

Figure 1 The conversion principle and setup. Droplets, from the break-up of a Rayleigh jet, are charged by EDL ions. The inertia of droplets moves them against the electrical field and converts (mechanical) kinetic energy to electrical energy.

2. Model

During the process of energy conversion from input pressure to electrical energy, there are many sources of energy loss. To estimate the limit of energy conversion efficiency, the energy losses are theoretically calculated in this chapter. We divide the energy conversion process in two steps: 1. Pressure to kinetic energy conversion of water. An applied input pressure difference pushes the aqueous solution out through a thin orifice where it forms a liquid jet, with defined

efficiency eff_{kin}. Viscous friction forces consume mechanical energy when the solution is moved at high speed to form the liquid jet via the micropore[4], so that only partially the pressure energy is converted to kinetic energy that is useful for electrical energy conversion. The formation of the cylindrical liquid jet also consumes part of the pressure energy to create air/water interface with a certain surface tension.[5] 2. Kinetic energy of droplets to electrical energy conversion, with defined efficiency eff_{el}. After jet breakup into droplets, the charged droplets move with an initially high speed against the electrical field and undergo air friction. Hence, partially the kinetic energy will be consumed by air friction. Finally, we can calculate the overall efficiency of ballistic energy conversion by $eff = eff_{kin} \times eff_{el}$. This should equals to the definition of electrical energy conversion efficiency $eff = I \times U/(p\ Q)$, where I, U, p, Q are measured current, voltage, applied pressure and flow rate in system. Figure 2 indicates the position where the main energy losses occur.

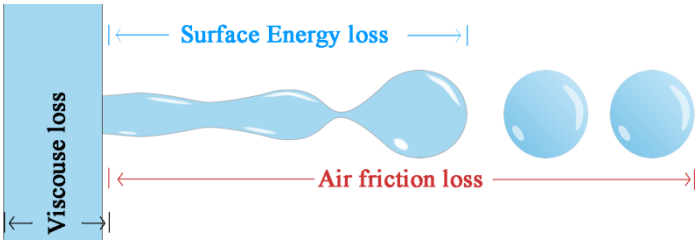

Figure 2 Categorization of losses in the model

Setup

To measure the energy loss of each step, the jet size and velocity of droplets are important to know. A custom setup was built that is able to capture double-illuminated images of droplets at certain desired distances from the micropore while applying a potential on the target or the guard ring and measuring pressure, flow rate and electrical current as shown in Figure 3a. The laser come from right side and camera will has a quite short time delay producing twice illumination on

the image. Litron Nano-PIV (Q-switched doubled NdYaq laser 532nm 6ns Dual cavity) used for the laser source and the images captured by Lumenera Lm135-io (4.65µm per pixel), via microscope Olympus BX-30MF. The laser time delay can be adjusted and controlled by a trigger Berkely delay generator BNC 575 (250ps accuracy). Droplet velocity information was extracted from the double-illuminated images by dividing displacement by the time step between illumination pulses. [6, 7] A sample image is shown in figure 3b. A high voltage source (*fug* - HCE 7 35000) was connected with a piece of metal at bottom, to decelerate charged droplets by producing an electrical field. Rest of the setup can be seen from chapter 3.

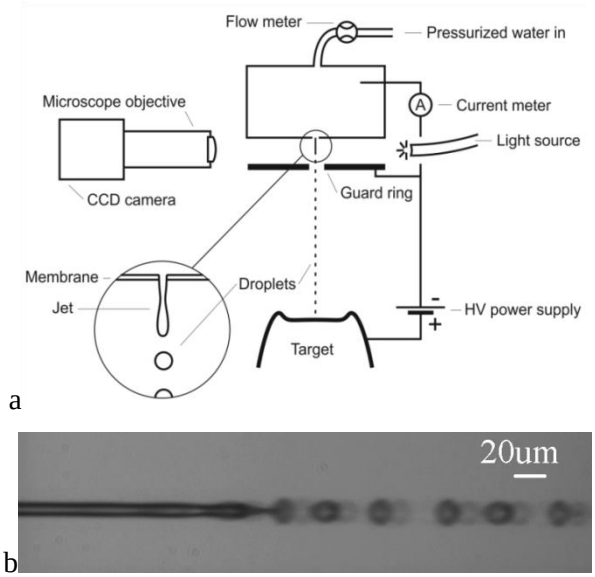

Figure 3. a. Setup for optical velocity measurements. Flow meter and water inlet are electrically isolated from the setup. Sample picture op droplets from the droplet stream. Images are taken with 10× objective and displayed on 4.65µm pixels. (scale bar indicates 20µm). Double laser illumination was used for measuring the movement distance within one pulse. The size and speed of droplets was analyzed by a Matlab script.

2.1 Loss factors in liquid

Liquid losses are defined as the ratio of kinetic energy of droplets (E_{kin}) after jet breakup to pressure-driven mechanical energy (E_{in}) :eff_{kin} = E_{kin}/E_{in}. In the liquid two main factors of loss are investigated: viscous losses due to the shear rate of water flow, and energy losses by generation of the water-air interface. In this section, we will discuss the viscous loss and surface energy loss separately.

2.1.1 Jet formation: viscous friction

The viscous energy losses of water flowing through an orifice can be analytically calculated by knowing the liquid flow velocity profile via the circular pore in the creeping flow model by Sampson.[8, 9] From empirical data on the head loss or pressure loss in a small opening into a circular pipe it is also possible to calculate the energy loss factor.[10] However, the Reynolds number is close to 100 in our system, not satisfying the creeping flow assumption for Sampson's Solution. In addition, the water passing through the micron-sized pore forms a free liquid jet in air, which is fundamentally different from the liquid flow in a pipe. Hence, it will be necessary to simulate the water flow to calculate the viscous energy loss in our experiments.

The input mechanical power is calculated by $p*Q$, where p and Q are input pressure and volume flow rate. Since the flow is continuous and constant at every position, we can separate the applied pressure energy into a fraction that is effectively used for driving the flow (p_{eff}), and the other two fraction that are lost due to viscous friction (p_{vis}) and surface tension (p_S).

$$p = p_{eff} + p_{vis} + p_S \tag{1}$$

The Bernoulli equation describes the conversion from pressure to kinetic energy of water flow without any viscous loss. With the simulation results of the liquid velocity, the fraction of applied pressure energy that is converted to kinetic energy (defined as eff_{kin}) can be calculated:

$$eff_{kin} = \frac{p_{eff}}{p} = \left(\frac{v_j}{v_b}\right)^2 \tag{2}$$

where v_j and v_b are the simulated mean velocity of liquid jet and the velocity calculated from the Bernoulli equation.

Energy loss factor

The first source of energy loss occurring during the conversion from pressure energy to kinetic energy of flowing water is viscous friction. The viscous friction force f_v during water flow through a pore is proportional to the area of the pore πr^2 with radius r. The product of force f_v and mean velocity v then gives the power consumed by the viscous force, $P = f_v v$. According to the theoretical calculation of flow rate in an orifice during single phase flow, the flow rate is proportional to r^3.[11] Hence, we can estimate that the fractional viscous energy loss equals f_v *v/p Q*, and thus is inversely proportional to *r*.

Above we defined an effective pressure that induces liquid flow: p_{eff}. To calculate this pressure we should realize that the pressure at pore exit isn't equal to atmosphere pressure, since the exiting solution forms a cylinder liquid jet that produces a local Laplace pressure. For the calculation of this pressure we have to use jet radius *a* instead of pore radius *r*, due to the contraction of the jet in air. Jet radius *a* determines the mean flow velocity under the applied flow rate. As a result, the effective pressure can be expressed as:

$$p_{eff} = p\,(1 - \frac{K}{a}) - p_S \tag{3}$$

where a is the jet radius, typically smaller than the pore radius due to jet contraction; p, K, p_S are the input pressure, viscous loss factor and Laplace pressure in the cylinder jet, respectively. The term K/a indicates the viscous loss, with the viscous loss factor K.. The loss factor K can be calculated from the flow profile obtained by simulation in Comsol using a two phase flow model.

The Bernoulli equation derived from conservation of energy describes the transition of pressure to flow rate without any energy losses. Conversely, an effective pressure can be calculated from the Bernoulli equation substituting the flow rate.

$$p_{eff} = {}^{1}/_{2}\,\rho_w v_j^2 \tag{4}$$

To separate the influence of surface tension, the surface tension was reduced by a factor of 20 in the simulations, so that by integration of surface only viscous friction played a significant role. Simulations then yielded a value for K of $1.30 \cdot 10^{-6}$m, determined as an average over simulations with several jet diameters (from 8μm to 30μm). This value is not valid for very small values of a where the flow rate is significantly influenced. The relation $a = 0.9r$ was taken from the 10μm pore simulations, which was confirmed by experiments. Many factors can influence the contraction ratio of liquid jet, such as pore size, surface roughness and velocity profile.[12] Experimentally we observed a larger contraction ratio approximately $a/r = 0.8$ in an experiment with a 30μm pore.

By knowing the velocity of the fluid through the pore we can calculate the flow rate:

$$Q = \pi a^2 \cdot v_j \tag{5}$$

By substituting Equations 3 and 4 in Equation 5 we find the theoretical flow rate. This theoretical flow rate satisfyingly matches our measurements as function of pressure for 10μm and 30 μm pores as shown in figures 4a and b.

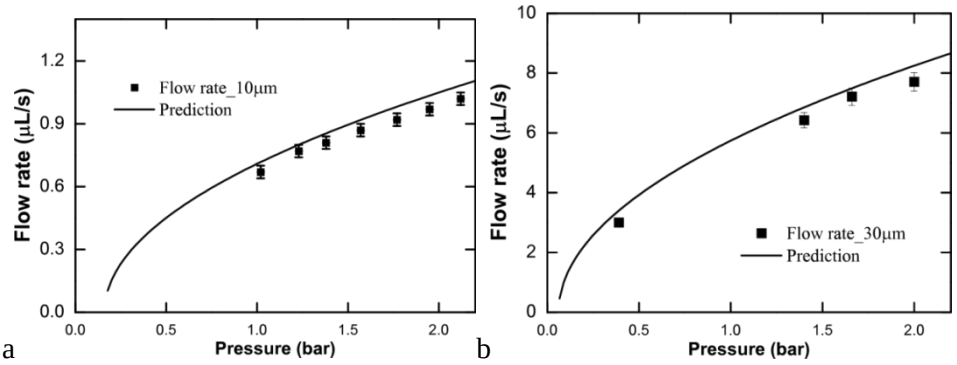

Figure 4 a. Observed and predicted flow rate for several pressures using a 10μm diameter pore. The theory is based on a jet radius of 4.5μm. b. the flow rate increase as function of applied pressure using a 30 μm diameter pore. The theory

is based on a jet radius of 11.9μm. A stronger contraction of the liquid jet was observed in the 30μm diameter pore.

2.1.2 Breakup: surface energies and the momentum balance

Surface effects are treated separately at the location of the pore and near the breakup of the jet, as illustrated in figure 5. The jet is formed out of the pore and the contraction ratio (*a/r*) of the jet determines the velocity v_j under constant flow rate, according to equation 5. In this jet formation section the surface forces are balanced and do not reduce the energy of the jet, but the Laplace pressure in the jet does reduce the net pressure exerted on the fluid. In the breakup section the Laplace pressure yields a positive contribution to the kinetic energy of the droplets, but the surface forces are not balanced and they form a negative contribution to the droplet kinetic energy[4].

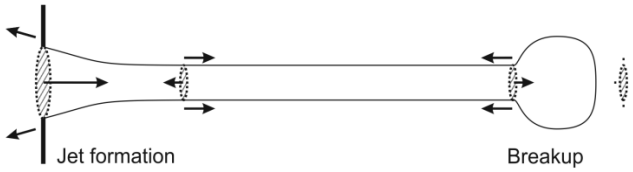

Figure 5 Illustration of surface forces and Laplace pressure effects

The liquid jet in air will break up into droplets according to Rayleigh-Plateau instability. Assuming the jet and droplets are perfectly axisymmetric, the surface forces in the radial direction are balanced, but are not in the movement direction. If we define an artificial surface at the position where jet pinches off, this surface "pulled" by the jet surface force but "pushed" by the droplet is not balanced (figure 5). This phenomenon was described and measured by Schneider et al. and the velocity was derived from the momentum balance [4]:

$$\frac{dm_j}{dt} = \frac{dm_{dr}}{dt} + \pi a \cdot \gamma \tag{6}$$

Where m_j, m_{dr} are the momentum of the liquid in the jet and in the droplets, respectively.

Working out the equation yields[4]:

$$v_{dr} = v_j \cdot (1 - \frac{\gamma}{\rho_w \, a \, v_j^2}) \tag{7}$$

Substituting Equation 3 and 5 in Equation 7 we can calculate the droplet velocity as function of the pressure. Dividing the droplet kinetic energy by the input energy $p \cdot V$ then yields the efficiency of pressure to kinetic energy conversion, $\mathrm{eff}_{\mathrm{kin}}$.

$$eff_{kin} = 1 - \frac{\rho_w v_{dr}^2}{2p} \tag{8}$$

Figure 6 shows the initial velocity of droplets (just after jet pinch-off). The data points indicate the measurements and the lines are from theory. A quite satisfactory agreement of theory and experiments is obtained. The left y-axis indicates the initial velocity of droplets, while the black solid points and blank points present the experimental measurements of velocity for 10μm and 30μm pores, respectively. From the initial velocity, we can calculate the energy conversion efficiency from pressure to kinetic energy for both pore sizes, shown as red dots from experiments and lines from theoretical predictions. A maximum eff_{kin} will be reached after pressure increase to a certain value. It is apparent that use of a larger pore can easily decrease the energy loss during generation of droplets.

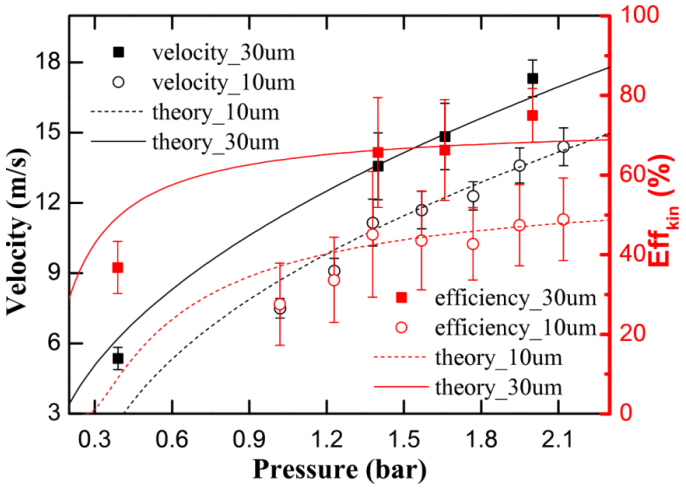

Figure 6 Velocity of the jet and efficiency of pressure to kinetic energy conversion (effikin) as function of applied pressure. The measurements and theory are shown for both 10μm and 30μm pores.

2.2 Loss factors in air

After jet breakup into droplets, the charged droplets move with inertial energy and deliver charges to the bottom target producing electrical energy. However, the air friction partially consumes kinetic energy so that not all the kinetic energy can be converted into electrical energy. The air friction loss factor will be discussed in this section.

The motion of droplets during the trajectory from pore to target is described by Newton's second law:

$$\vec{F} = m\frac{d\vec{v}}{dt} = \overrightarrow{F_{el}} + \overrightarrow{F_{dr}}$$

Then we can derive:

$$v \cdot \frac{dv}{dx} = \frac{F_{el}}{m} + \frac{F_{dr}(x)}{m} \tag{9}$$

The motion of the droplets can thus be calculated by the electric force F_{el} and the drag force F_{dr} as functions of the trajectory position x. The observed droplet size increases with distance x because of merging of the droplets in-flight, from approximately 8μm radius after jet breakup to 20μm radius at 13mm from the pore. The statistics of droplet sizes obtained for both 10 and 30μm pores are shown in figure 7. Both of them produce main droplets and satellite droplets.[6] However, since the satellite droplets from the 10μm pore are too small to be detected, only the main droplets are shown in the figure. Main and satellite droplets will coalesce very quickly after some travelling distance. Thus there were no satellite droplets observed at 1.5cm below the chip. The average droplet size increases as a function of distance.

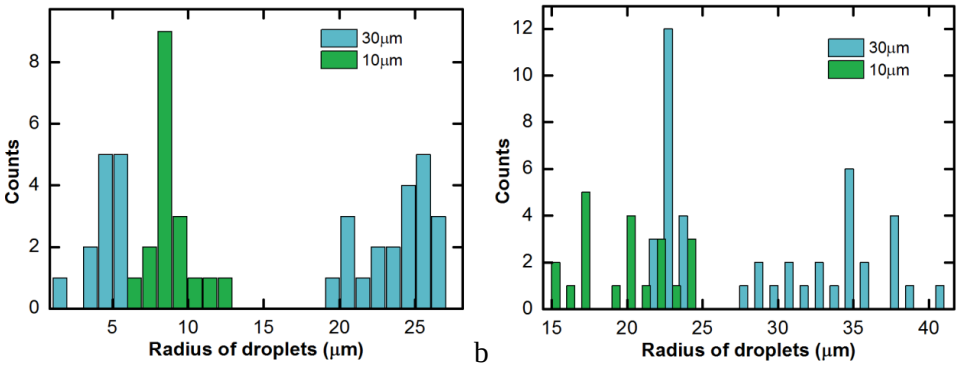

Fig. 7. Histograms of size variation of droplets. (A) the size distribution obtained with a 10μm diameter pore (green) and a 30μm diameter pore (blue), at the point where the jet breaks up into droplets. The data give a clear indication of a bimodal distribution with small satellite droplets and large 'main' droplets. (B) the size distribution of droplets at 1.3cm(10mm pore) and 1.5 cm(30mm pore) distance from the chip. Please note the change of scale in the x-axis.

The air drag force on a single droplet can be expressed as[13]:

$$F_{dr} = \frac{1}{2}\rho_{air} v_d^2 c_{dr} A \tag{10}$$

where ρ_{air}, v_d, C_{dr} are the mass density of air, the speed of the droplet relative to air, and the air friction coefficient. In our calculation, we assume the droplets are perfect spheres without any vibration.

Measurements of the droplet velocity as function of the distance from the pore are shown as points in Figure . Figure 8a indicates that the velocity of droplets from 10μm and 30μm pores decreases as function of the distance in the absence of an electrical field from the target. Dashed lines give the theoretical predictions when there is just a single droplet moving in air. These predictions are approximate. However, in our experiments the droplets break continuously from the jet with a certain spacing. This will induce a flow of the surrounding air with the droplets, and the decrease of the relative speed of droplets with respect to the surrounding air will induce less air friction energy losses. The solid lines present the velocity prediction with consideration of this air flow, which we will discuss later in this chapter.

In addition, we applied 7kV voltage on the target by a high voltage source (*fug*-HCE 35000). The solid points (including the square black points and grey circle points from two separate experiments) and green blank points indicate the measured droplet velocity as a function of trajectory distance without and with 7kV target potential applied, respectively. With the additional electrical force from the target, the velocity of the droplets decreased faster, converting kinetic energy to electrical energy.

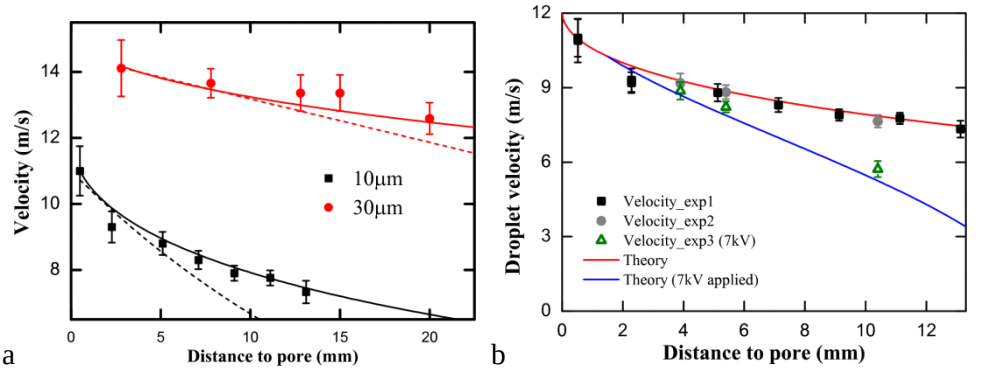

Figure 8 a. The velocity decrease as function of trajectory distance for liquid jet from 10µm pore (black points) and 30µm pore (red points) compared with two theoretical predictions, without (dashed lines) and with the air wake (solid lines). b Velocity measurements and predictions as function of distance from the micropore. The applied pressure is 1.4bar and the distance between pore and target (for dataset 3) is 13mm. In the measurements with applied electrical field, this field was applied between 3 (location of the guard ring) and 13mm (the location of the target).

The motion of air is not bounded by a nearby stationary wall, and therefore the vortex that is formed by the droplets can extend to unlimited space as shown in figure 9a. The air drag force is due to the relative velocity between air and droplets. Hence, in the simulation we can keep the droplets stationary and introduce moving air flow around these droplets. The force on the droplets was calculated by integration of the force on the droplet surface, and a coefficient of the air drag force was introduced in equation 9 to indicate this force decrease. All these simulations were performed using a FEM fluid flow model in Comsol. The results are shown in figure 9 below.

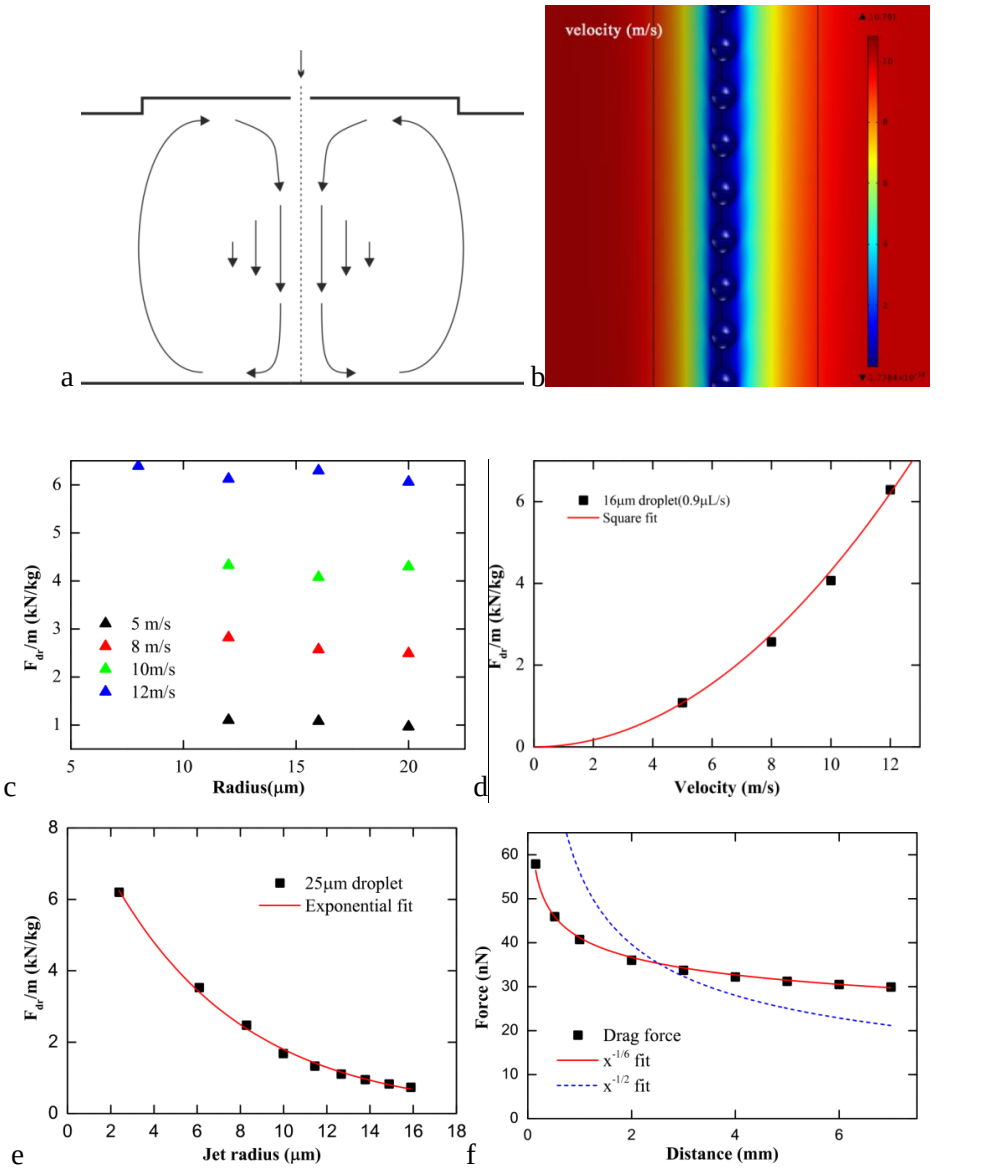

Figure 9: a. Illustration of a hypothetical far-extending wake of air nearby the liquid jet. b. The air velocity distribution around droplets. It can be clearly seen that the relative velocity between surrounding air and droplet decreases due to the air movement. c. Force per mass as function of droplet size for several velocities measured at 2.5mm from the start of the droplet stream. d. Force per mass as

function of velocity for several measured for 16µm droplets, Q =0.9µl s-1, at 2.5mm from the start of the droplet stream. e. Force per mass as function of r_{pore}, which represents the flow rate Q according to the Bernoulli equation. The simulations used r_{drop} = 25µm and 10m/s measured at 2.5mm from the start of the droplet stream. f. Friction force simulations with 14µm droplets and fitting lines for v = 10m/s as function of trajectory distance.

Simulations show that a representative wake of air is generated for distances larger than 2.5mm. Because of the coalesce of droplets, it would be more practical useful to calculate the force per mass ratio *F/m* instead of force, so that we can get rid of the influence on droplet size variation by coalesce. Different droplets sizes were introduced to calculate the air drag force per mass ratio, to investigate the influence of droplets coalescence (figure 9c). Simulation results in figure 9d show that the $\frac{F_{dr}}{m}$ coefficient is independent of the droplet size for constant mass flow rate over distance. This is mainly because the distance between two droplets become larger after merging, supplying more space for air flow in between. Hence, even though the merged droplets are larger, this does not influence the effect of air friction during the trajectory. A variation of flow rate however can change droplet velocity and the spacing of the droplet mass center, inducing changes of the $\frac{F_{dr}}{m}$ coefficient, as shown in figure 9e. For a stream of equal-sized and equal-distance perfectly spherical droplets the spacing of the droplet mass centers is:

$$d = v\frac{\frac{4}{3}\pi r^3}{Q} \tag{11}$$

where d, v, Q, r are distance between droplets center of mass, droplet velocity, flow rate and droplet radius, respectively.

The air friction force decreases with trajectory distance. Lower speed, shorter spacing of droplets and higher surrounding air velocity can induce this decrease. From non-linear fitting of the air drag force by simulation results (figure 9f), it can be seen that the force decrease as $x^{-1/6}$ fits well as a function of distance x. However, for simplicity to get an analytical equation, we adopt the force decrease as $1/\sqrt{x}$.

Hence, substituting this decrease factor $1/\sqrt{x}$ to $\frac{F_{dr}}{m}$ in Equation 9, the air force per mass ratio can be expressed as

$$\frac{F_{dr}}{m} = \frac{C_{dr}\, v^2}{\sqrt{x}} \tag{12}$$

where C_{dr} is a distance-independent coefficient obtained from simulations.

By surface integration of air drag forces from simulation, we could obtain the coefficient $\mathrm{C_{dr}} = 5.2\, e^{-\frac{a}{6.1[um]}}$ for different pore sizes. The maximum deviation is 0.18 when the droplet radius is varied from 8 to 20μm and the velocity from 5 to 12 m/s. We can substitute $\mathrm{C_{dr}}$ in Equation 9 and obtain the velocity distribution along the trajectory distance, $\mathrm{v(x)}$. For the initial droplet speed $\mathrm{v(0.5mm)} = 11\mathrm{m/s}$, as obtained from measurements, the theoretical predictions are drawn in Figure a.

The electrical force per mass ratio $\frac{F_{el}}{m}$ in Equation 9 can be calculated from the charge density of the droplets and the electrical field strength, assuming the electric field is constant:

$$C_{el} = \frac{F_{el}}{m} = \frac{U}{l}\frac{\rho_e}{\rho_w} \tag{13}$$

where $C_{el}, U, l, \rho_e, \rho_w$ are the coefficient of electrical force (defined), potential difference, length over which the electrical field exists, charge density in the droplets and mass density of water, respectively. The charge density is calculated from $\rho_e = \frac{I}{Q}$, where I is the upstream current in the reservoir. The theoretical prediction with an applied electrical field (7kV on target with 10mm distance) is also shown as the blue solid line in Figure b. The charge density value used was $3.4\mathrm{C/m^3}$ (2.9nA at 0.85μL/s). Because the electrical energy only can be harvested after droplets came out of the guard ring, the theoretical prediction was started from the position of the guard ring (3mm). With 7kV applied voltage over a distance of 10mm, a typical value of $\mathrm{C_{el}}$ is 2380 N/kg,

Solving Equation 9 by substitution of Equation 12 and Equation 13 with the initial condition $v(0) = v_0$ yields

$$v^2(x) = \frac{-C_{el}}{C_{dr}}\sqrt{x} + v_0^2\, e^{-4\,C_{dr}\sqrt{x}} + \frac{C_{el}}{4\,C_{dr}^2}\left(1 - e^{-4\,C_{dr}\sqrt{x}}\right) \tag{14}$$

In this equation the first term describes the converted electrical energy; the second term describes the energy loss by viscous friction, and the last term is a compensation energy due to electrical force. The last term is a compensation term accounting for a decrease in the energy loss by air friction in the presence of an electrical field. This is because the electric field slows the droplets down, and the lower velocity of the droplets causes less air friction. By addition of the third term, lower energy losses are expected to be observed relative to the theoretical prediction.

By equation 14, we can calculate the energy distribution along the trajectory distance. The remaining kinetic energy of droplets can be calculated from the velocity. The electrical energy per volume can be simply calculated by

$$\frac{E_{el}}{V} = \frac{x - x_0}{l}\, U\, \rho_e \tag{15}$$

where x_0 is the location of the guard ring. The effects of the compensation term can be seen in the figure 10: the total air friction loss is higher when droplets move without an electrical field.

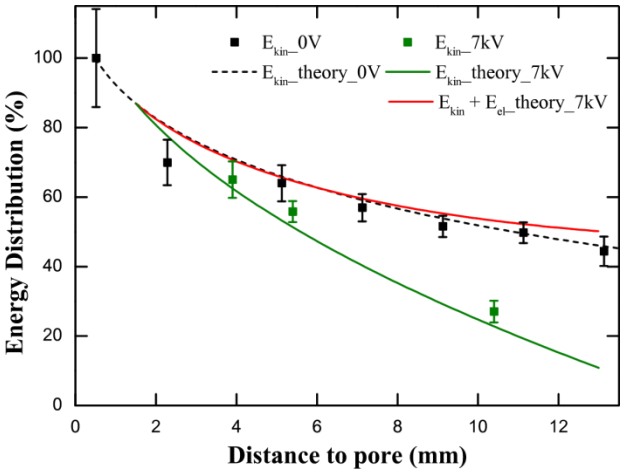

Figure 10 Energy distribution in the system as function of distance from the jetting micropore. The lines show the kinetic energy of the water as fraction of the initial kinetic energy. Additionally a line is shown with added electrical energy (red), to show that air friction losses are smaller when an electrical field is applied. In the measurements with applied electrical field, this field was applied between 3 and 13mm.

2.3 System efficiency

It is interesting to predict the efficiency of the ballistic energy conversion system. Combining the equations of energy loss in the two consecutive steps (see Figure 2), by substitution of equation 3 and 5 in equation 14, we can obtain:

$$v^2(x) = \frac{-C_{el}}{C_{dr}}\sqrt{x} + \frac{2\left(p\left(1-\frac{K}{a}\right)-\frac{\gamma}{a}\right)}{\eta_{water}}\left(1-\frac{\gamma}{2(p\,(a-K)-\gamma)}\right)^2 e^{-4\,C_{dr}\sqrt{x}} + \frac{C_{el}}{4\,C_{dr}^2}\left(1-e^{-4\,C_{dr}\sqrt{x}}\right) \quad (16)$$

The maximum output power can be gained when droplets convert all kinetic energy against air friction energy and electrical energy, and then land on target. Hence, we can calculate the maximum electrical field by defining that the final velocity equals zero $v(L)=0$, where L is the maximum distance droplets can reach under the electrical field force f_{el} and air friction force f_{dr}. Then we can calculate the required

maximum electrical field from the electrical drag term with constant charge density (3.4 C/m^3) as function of guard ring-target distance x:

$$C_{el,max} = \frac{x-x_0}{L} U\rho_e = \frac{4v_0^2 C_{dr}^2 e^{-4C_{dr}\sqrt{x}}}{-1+4C_{dr}\sqrt{x}+e^{-4C_{dr}\sqrt{x}}} \quad (17)$$

By substituting equation 17 in equation 16, we can obtain the energy distribution in electrical energy, air friction and compensation terms.

The energy loss in air friction can be expressed as eff_{el} which can be calculated by:

$$eff_{el} = 1 - \frac{E_{dr}}{E_{kin}} = 1 - \frac{2C_{dr}}{v_0^2}\int_0^L \frac{v(x)^2}{\sqrt{x}}dx \quad (18)$$

where E_{dr} is the energy loss by air friction.

Finally, the system efficiency can be calculated by

$$eff = eff_{kin} \cdot eff_{el}$$

The efficiency calculated from the energy loss factors is equivalent to the definition of the electrical energy conversion efficiency $eff = U \cdot \rho_e / p$.

With the above equations for the total efficiency we can determine the direction to optimize the system to achieve minimal energy losses. This predicted system efficiency is plotted against input pressure, pore-target distance and pore radius in Figure 11. In these system efficiencies the electrical force is assumed to be optimized such that the final velocity at the target is exactly zero, by solving Equation 16 at $v = 0$ and $x = L$ for C_{el}. This results in a required field strength which is also indicated in the figure, because in practical systems the field strength needs to be limited to prevent breakdown of air and corona discharges. The breakdown field strength of air is 2.3kV/mm (the maximum value occurring in the figure). However, corona discharge can happen at lower voltages, because of small curvature on the target. From Peek's equation[14], we can calculate that the maximum working voltage can be about 24kV with 3cm distance between guard ring and target.

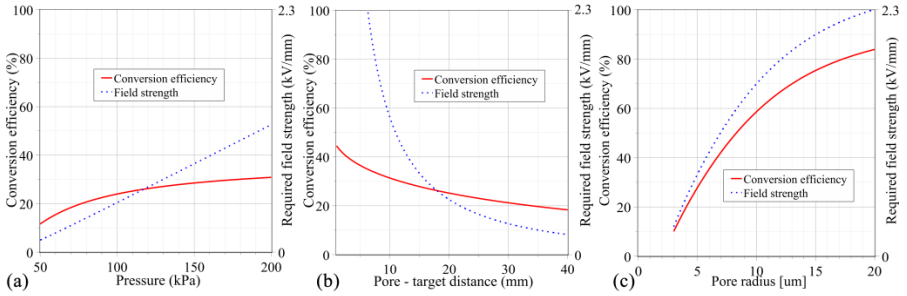

Figure 11 System efficiencies are predicted with variations of applied pressure (a), pore-target distance(b) and pore radius (c). Optimal electrical field strengths are shown as dashed lines, which are required for the maximum conversion efficiency (red solid lines). Parameters used in these calculations are a charge density of 3.4C/m^3, p=140kPa, d=15mm and r=5μm, where not stated otherwise.

3. Discussion and conclusions

We experimentally measured and theoretically modeled the energy losses during the conversion process from pressure energy to electrical energy. The energy conversion process is divided in two steps: 1. from pressure-driven input mechanical energy to kinetic energy of charged droplet flow; 2. Kinetic energy of charged droplet flow to electrical energy on target.

In experiments, we observed that the energy loss in the first step under 1.4bar pressure is 52% with a 10μm pore and 35% with a 30μm pore. In the theoretical analysis, the energy loss by viscous friction is over 30% for a 10μm pore, while the energy loss is 20% loss for surface creation. The final value of 50% loss is therefore in good agreement with the simulations. Also the lower viscous energy loss (25.3%) and surface energy loss (8.4%) from simulation and analytical calculation when using a 30μm pore is in good agreement with the measurements.
A lower air friction energy loss is observed in experiment than in simulations using the air drag force equations, and approximately 40% of the kinetic energy is lost in friction with air for a 15mm pore-target distance without electrical field. From the simulations, we found that the probable reason of lower air friction is the movement of surrounding air that decreases the air drag forces on the droplets. By fitting with the forces as function of trajectory distance, the velocity can be

predicted as function of travelling distance. Less air friction will also be produced when the droplets are moving in the electrical field generated by the target voltage, since the lower velocity of droplets causes less air friction forces.

The relation between losses and pore radius was modeled using a combination of predictions from simulation data for viscous losses in the pore, theory and literature data for the surface energy losses and simulation data for the air friction coefficients for various flow rates. The model that was developed based on this data predicts that substantially higher efficiencies can be obtained for larger pore sizes. It is therefore recommended to use larger pore size to have lower energy loss. This approach will be followed in Chapter 5.

4. References

1. Duffin, A.M. and R.J. Saykally, *Electrokinetic Power Generation from Liquid Water Microjets.* Journal of Physical Chemistry C, 2008. **112**(43): p. 17018-17022.
2. Duffin, A.M. and R.J. Saykally, *Electrokinetic hydrogen generation from liquid water microjets.* Journal of Physical Chemistry C, 2007. **111**(32): p. 12031-12037.
3. Rayleigh, L., *On the Capillary phenomena of Jets*, in *Proc. R. Soc. Lond.*1879. p. 196-199.
4. Schneide.Jm, et al., *Stability of an Electrified Liquid Jet.* Journal of Applied Physics, 1967. **38**(6): p. 2599-&.
5. White, H.E., *Modern College Physics.*1948: van Nostrand.
6. van Hoeve, W., et al., *Breakup of diminutive Rayleigh jets.* Physics of Fluids, 2010. **22**(12).
7. van der Bos, A., et al., *iLIF: illumination by Laser-Induced Fluorescence for single flash imaging on a nanoseconds timescale.* Experiments in Fluids, 2011. **51**(5): p. 1283-1289.
8. Sampson, R.A., *On Stokes's Current Function.* Philosophical Transaction of Royal Society of London. A, 1891. **182**: p. 449-518.
9. Sisavath, S., et al., *Creeping flow through an axisymmetric sudden contraction or expansion.* Journal of Fluids Engineering-Transactions of the Asme, 2002. **124**(1): p. 273-278.
10. Lienhard, J.H. and J.H. Lienhard, *Velocity Coefficients for Free Jets from Sharp-Edged Orifices.* Journal of Fluids Engineering-Transactions of the Asme, 1984. **106**(1): p. 13-17.
11. Rijm, C.J.M.v., *Nano and Micro Engineered membrane technology*2004.
12. Ernest Frederick Brater, H.W.K., James E. Lindell, C. Y. Wei,, *Handbook of Hydraulics*1996, McGraw-Hill, New York, N. Y.
13. Rayleigh, L., *Sur la resistance des spheres dans l'air en mouvement.* C R. Acad. Sci. Paris, 1913. **156**: p. 109.
14. Peek, F.W., *Dielectric Phenomena in High Voltage Engineering*1929: McGraw-Hill.

Chapter 5

Gate induced energy conversion by liquid jet

Here we show that the efficiency of a ballistic energy conversion system can be further improved by gate control. With gate control the electrical current generation is enhanced a hundred times with respect to the current generated from the zeta potential. A maximum efficiency of 48% is obtained using a 30μm pore. Energy was still lost on viscous flow, surface production and air friction. The higher droplet charge density by using gate control can also be used to decrease the required target voltage. Thus a 12% efficiency was achieved with 500V target voltage using a 10μm pore and voltage gating. The different induction modes, as a consequence of the efficiency, are discussed and modelled in this chapter.

Manuscript to be submitted

1. Introduction

As we discussed in chapter 3, by connecting a guard ring the electrical field generated by the target potential can be very well shielded, so that the upstream current or charge density of droplets can be made independent of target voltage. However, many factors can influence the streaming current generation such as pH changes and surface contamination, thus inducing unstable energy harvesting. As theoretical predictions in Chapter 4 showed, a larger pore size will induce less energy loss during the droplet generation and less air friction energy loss. This is mainly due to the decrease of surface-bulk ratio of flow in larger pores. However, a larger pore size will also decrease the net charge density in the droplets stemming from the electrical double layer. Thus, higher target voltages are required for high efficiency energy conversion, inducing more chance of electrical energy losses. In addition, highly charged droplets are preferable, since then a lower target voltage is required to produce the same output power. This is be preferable for practical applications because several hundred volts instead of kilo-Volts are commonly used in our daily life.

By applying external voltages on the guard ring, we can not only shield the target electrical field, but also further adjust the electrical field between guard ring and chip. This electrical field will attract additional or even reversed net charges in the liquid jet so that the droplet charge density can be tuned. In this chapter, we will experimentally and theoretically investigate the gate controlled ballistic energy conversion process. Two different induction modes are discussed for current generation. Theoretical models are setup for prediction of current generation and the influence on energy conversion.

2. Principle and setup

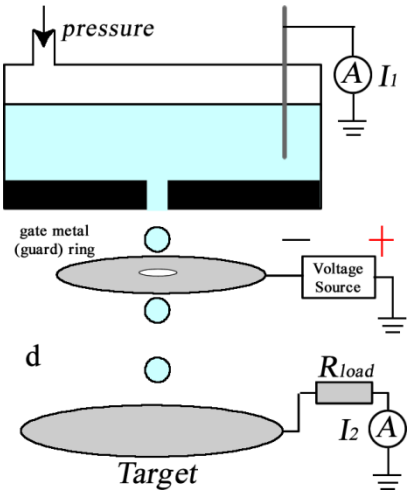

Figure 1 Schematic of the gated setup. Charges are introduced in the droplets by a gate metal ring connected to a voltage source.

Figure 1 shows the schematic picture of the setup. A silicon-enriched silicon nitride membrane (less than 1μm thickness) machined with a single micropore was mounted in a chip holder. Pressure drives aqueous solution through this pore which forms a liquid jet in air. After jet breakup into charged droplets, a metal target collects all charged droplets and the current runs via a resistor (ranging from GOhm to TOhm) to ground. Hence, electrical power will be produced. An external voltage source (Keithley 2410) is connected to this guard ring giving it either a positive or negative voltage, and thus provide additional polarization of liquid jet. This setup is quite comparable with an electrospray setup.[1, 2] It must be remarked that there is no current passing through this gate ring (unless droplets are deflected to the gate), so that there will be no electrical energy dissipated by a gate ring current. The energy conversion efficiency is then as normal defined as the ratio of electrical output power to mechanical input power.

3. Results

3.1 Energy conversion optimization by gating using a 10μm pore

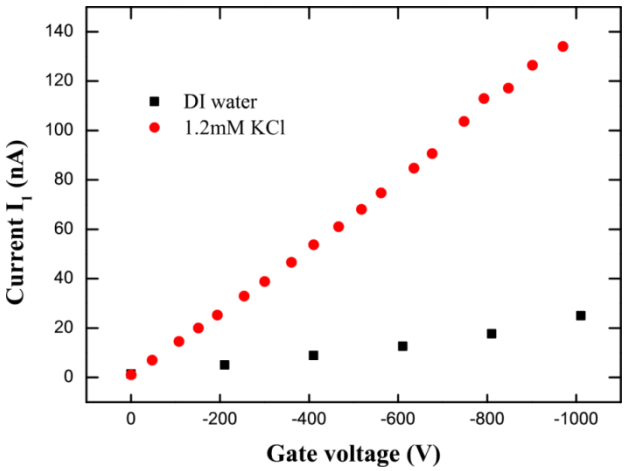

Figure 2. The upstream current I_1 linearly increases with gate voltage without a load resistance connected. Higher currents are obtained with a salt solution than with demineralized water. A 10 μm pore was used and a pressure of 2.2 bar was applied.

Figure 2 shows that the upstream current I_1 increases linearly with gate voltage when 2.2 bar pressure was applied over a 10μm diameter pore. Two different solution (DI water and 1.2mM KCl) were used in the measurements. Here, we define the induction rate C_{ind} as the induced current per applied gate voltage $C_{ind} = I/U_g$. A high conductivity of solution helps to increase the induction rate, which is the slope of the data points obtained by a linear fit. We will explain this observation later in this chapter. Assuming droplets of homogeneous size are generated with a volume flow rate of 1.1μL/s, the maximum droplet charge density ρ_e is calculated as current divided by observed volume flow rate (I/Q) of droplets and is 123C/m^3 which is close to the Rayleigh limit of 153C/m^3 in 10μm diameter droplets. The Rayleigh limit describes the maximum quantity of charge in a droplet before breakup as a result of repulsive force occurs,

$$q^2 = 64\pi^2 \varepsilon \gamma R_{dr}^3 \quad (1)$$

where q, ε, γ are the quantity of charge, vacuum permittivity and surface tension. [3, 4] Higher droplet charge quantities will induce an unstable droplet or will even cause an explosion of the droplet due to the Coulomb force.[5] Our working current shown below is generally much lower than this limit, so the effects of a high charge density on droplets will not further be discussed in this chapter.

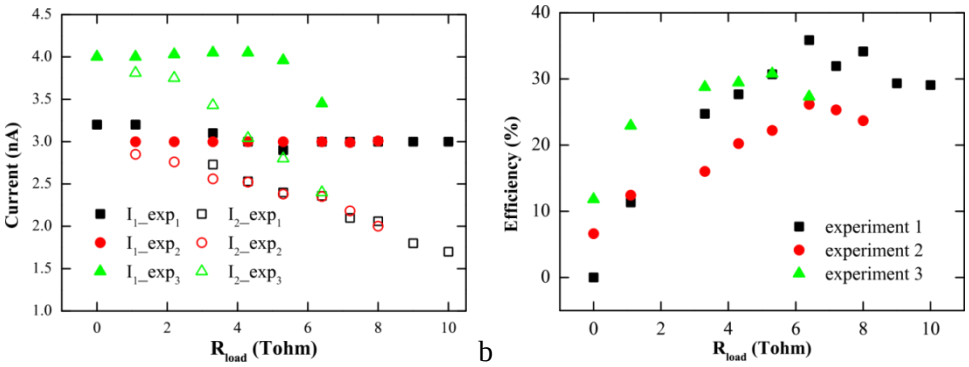

a b

Figure 3. a. Current changes as function of load resistance. A small negative voltage (see table 1) was applied to the guard ring to adjust the charge density of droplets to keep upstream current I_1 constant. b The efficiency as function of load resistance; maximal efficiency is around 35%. Demineralized water was used in these experiments.

Figure 3a shows for three typical measurements with a 10μm diameter pore that I_2 (open symbols) changes with a load resistance increase. Demineralized water was used in these experiments. The difference between these experiments and the experiments from chapter 3 is that in this case small gate voltages (relative to target voltage) were applied so that we are able to keep the upstream current I_1 constant (at 3nA or 4nA). As a result, a constant charge density was maintained in the droplets when load resistance increased. The gate voltages of three different experiments can be seen in table 1. The gate voltage was introduced originally because of the instability of upstream current generation in these three experiments , which totally depended on the charges from the EDL, was lower than 1nA. Hence, these relatively small voltages applied to the gate ring can induce and stabilize the

current generation. Downstream current I_2 decreases gradually with load resistance due to deflection of droplets and electrical losses (electrospraying and corona discharge). By measurement of pressure and flow rate, we calculated the energy conversion efficiency as shown in Fig3b. Finally, we obtain a maximum 35% efficiency from a 10 μm pore with this gate controlled induction system.

Rload(Ohm)	1.1 T	2.2 T	3.3 T	4.3 T	5.3 T	6.4 T	7.2 T	8.0 T	9.0 T	10.0 T
Exp1	**-250V**	**-250V**	**-250V**	**-250V**	**-250V**	**-250V**	**-250V**	**-250V**	**-250V**	**-250V**
Exp2	**-215V**	**-235V**	**-241V**	**-252V**	**-260V**	**-265V**	**-274V**	**-280V**		
Exp3	**-342V**	**-342V**	**-342V**	**-342V**	**-342V**	**-342V**	**-342V**	**-342V**		

Table 1. Voltage applied on the guard ring for three independent experiments.

3.2 Energy harvesting by gating using a 30 μm pore

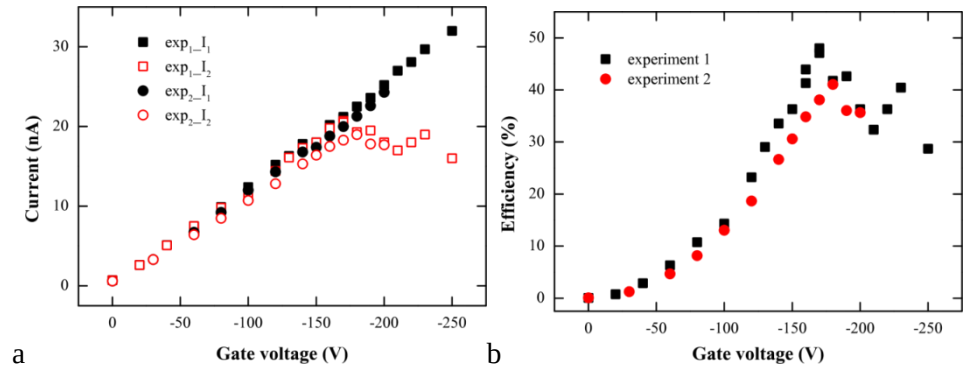

Figure 4 a. Both the variation of upstream current I_1 and downstream current I_2 as a function of gate voltage. b The efficiency as function of gate voltage. A 10mM KCl solution was used in these experiments and a 30 μm diameter pore.

From the theoretical analysis presented in chapter 4 figure 11, we know that the liquid jet generated from a larger pore is expected to has less energy loss by lower viscous friction forces, lower surface energy and lower air friction during travelling, due to the smaller surface-bulk ratio. However, use of larger droplets will also decrease the net charge density from the electrical double layer, thus higher target voltages will be required for high efficiency conversion, inducing more energy losses by corona discharge or electrospraying from the target. A gate-controlled system is therefore preferably used to increase droplet charge density, especially for large pore.

Figure 4a shows two typical measurements using a 30μm pore with addition of KCl (10mM) in the aqueous solution. A 1.01TOhm resistor was connected in the downstream circuit. The negative gate voltage was tuned from 0V to -250V to increase upstream current I_1. Downstream current I_2 increases with I_1 at increasing gate voltages and then starts to decrease around a target voltage of 20kV. The deflection of droplets and electrojetting were then observed from target to gate ring. We ascribe this to electrical breakdown (corona discharge) between target and guard ring occurring at high field strengths, as can be calculated Peek's equation

$U_c = m_v g_v r ln(^d/_r)$, which describes the voltage breakdown limit between two targets, where U_C, m_v, g_v, d and r are the corona inception voltage, irregularity factor of surface smoothness, "visual critical" electric field, distance between objects and radius of target, respectively.[6] With the minimum radius of curvature on the target electrode 1.4mm and distance of 3cm, the limit of target voltage in our system is about 24kV. The efficiencies of these two experiments are shown in figure 4b. The maximum efficiency is close to 50% (48%), which is slightly lower than the theoretical prediction as shown in figure 11 of chapter 4. A possible explanation is that the required target voltage is higher than the actual limit of our target collector.

3.3 Energy harvesting at lower target voltage

In the previous experiments, high efficiency was obtained at quite high target voltages (typically ten kilovolts), which is not convenient for application. By application of high gate voltages we will now aim to strongly increase the droplet charge, so that we can much decrease the required target voltage. A 10 Gohm resistance was used to replace the TOhm resistors for energy conversion.

A 2.2bar applied pressure drives 0.1M KCl solution out of a 10μm pore. By gradually increasing the negative gate voltage, droplet charge density was adjusted. The current variation as function of gate voltage is shown in figure 5a. The energy harvesting results are furthermore shown in figures 5a and 5b. It is seen in figure 5a that the downstream current I_2 initially increases with I_1, and then decreases due to droplet reflection. Efficiencies were calculated and are shown in fig 5b.

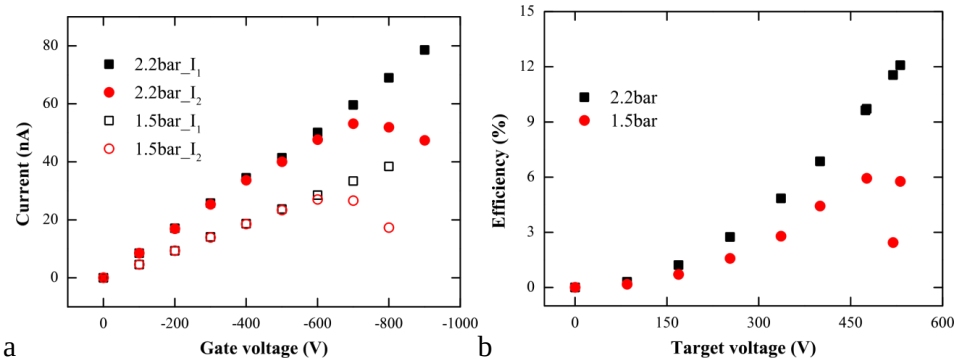

Figure 5. a The efficiency increase as function of gate voltage. b The efficiency increase as function of generated voltage.

The maximum efficiency obtained with the 10GOhm resistor is 12% with an applied pressure of 2.2bar and -700V gate voltage. Such low efficiencies are partly due to the fact that part of the kinetic energy is consumed to overcome the potential from the gate (-700V), as we will discuss later in this chapter. Another reason for this low efficiency is that the droplets were highly charged thus repelling each other during travelling. Under some circumstances, a droplet cone was formed when the droplets came out through the induction ring. As a result, the droplets can't form a straight air wake and lose more kinetic energy against air friction than calculated value in the theoretical prediction in chapter 4. Besides, the flat target surface will induce a different transport distance for the droplets at the inside of the cone and at the outside of the cone. The droplets that need to travel a longer distance will be more easily deflected by the target voltage, thus the inhomogeneous distance will cause a smaller energy conversion efficiency. A positive aspect is that it can be seen that the maximum efficiency was obtained around 500V target voltage, which is in the range of the daily used voltages.

4. Theoretical models of current induction

We have shown that the current generation can be well controlled by the applied gate voltage. It is quite interesting to theoretically investigate the induction models, so that we can have a better understanding on the influence of the energy conversion performance. Prediction of the current generation and optimal operational conditions for energy conversion using gating will be discussed in this section. We found that it would be possible to induce the current by placing the induction ring in two different positions. We termed the accompanying induction modes plate mode and cylinder mode.

4.1 Plate model of current induction

Current induced by an infinite large plate

If we place the induction ring below the jet end, the induction of charge can be modeled as a cylindrical rod ending in a spherical droplet opposite to an infinitely large plate. The air capacitance in our droplet – induction ring system can then be described as a sphere-plate capacitor.

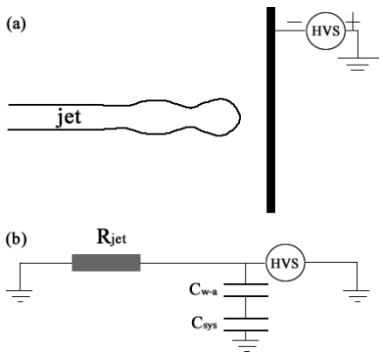

Figure 6 Electrical model of current induction in plate mode.

The droplet is connected to the ground via the water jet. We assume that the water jet can be approximated as a resistance R_{jet}. We can distinguish two capacitors in the system: the capacitance of the air-water interface ($C_{w\text{-}a}$) and the capacitance of

the jet-plate system in series connected. The capacitance of the water-air interface ($0.2F/m^2$) is much larger than the capacitance of the jet-plate system due to the large distance between the plates of the latter.[7, 8] Hence, the final capacitance will be dominated by the capacitance of jet-plate gating system. To simplify the problem, we can consider that the droplets are perfectly spherical. The capacitance of the system in plate mode (C_p) can then be modeled as the capacitance of an "infinitely" long cylinder (jet) with a perfect sphere at the end.

$$C_p = C_{rod} + 4C_1\pi\varepsilon_0 R_{drop} \tag{2}$$

where ε_0 and R_{drop} are vacuum permittivity and initial droplets radius; C_{rod} and C_1 are the capacitance of the liquid jet and a correction coefficient of capacitance on initial droplets. The correction factor stems from the fact that the droplet formation is a dynamic process. During the droplet pinch-off process, the size will continuously increase which influences the capacitance of the induction gate and liquid jet. So, a factor C_1 was introduced for a more precise analytical estimation, which will be discussed in the appendix of this Chapter.

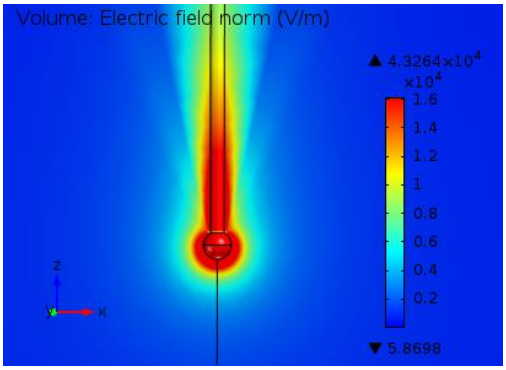

Figure 7. The simulation results of the electrical field at the end of the liquid jet (Comsol).

From our simulation results of the electrical field as shown in figure 7, it can be clearly seen that the field strength nearby the tip is the strongest indicating how the capacitance is distributed. During a droplet pinch-off process, the droplet size increases gradually, thus the capacitance of the system changes as function of the

pinch-off time (see Appendix). Here, we take the average size of the droplets over the pinch-off time. Hence, the correction factor C_1 is estimated from this simulation and used in the calculation later. The capacitance of the cylinder rod equals 3×10^{-16} F from our simulation, and the capacitance of the spherical droplet was analytically calculated, with a correction factor C_1 from simulation (discussed in Appendix).

In addition, we will not attempt to extensively describe the time-dependent charging process, since it will be rather complicated because jet shape and droplet size varies with time. To simplify the model, we assume that the size of the droplets is homogenous and the formation process is exactly repeatable. Furthermore, the liquid jet was modeled as a single capacitor connected with a single resistor (R_{jet}).

The electrical resistance of a cylinder water jet with radius a is $R_{jet} = \frac{l}{\pi a^2} \cdot \kappa$, where a and κ are jet radius and conductivity of the solution. The electrical resistance of the water jet (typical length 500μm and radius 4.45μm from a 10μm diameter pore) ranges from 1MOhm to 1TOhm when using a 1MKCl solution and DI water, respectively.

The induction current can be calculated from the gate voltage and capacitance of the system:

$$I = {}^{q}/_{\tau} = U \cdot C_p/\tau \tag{3}$$

where q, τ, U, C_p are the charge quantities on single droplets, droplet formation time, voltage difference between jet tip (U_{tip}) and gate voltage (U_g) and capacitance in plate mode. By substituting the voltage difference, we can obtain:

$$I_1 = C_p\,(U_g - U_{tip})/\tau \tag{4}$$

Assuming the liquid jet is an Ohmic resistor, the jet tip voltage $U_{tip}(\tau)$ is $I(\tau)\cdot R_{jet}$. Hence, we can substitute $U_{tip}(\tau)$ in the above equation to calculate the pinch-off time (τ) dependent induced current per gate voltage change as a function of the solution conductivity. Depending on the jet resistance, I(τ) can be very large and flow for a much shorter time than the droplet formation time, or very small and

flow for the entire droplet formation time. U_{tip} (τ) can be calculated using the following considerations.

The Ohmic resistance of the liquid jet and the capacitance of the jet and gate ring ('system capacitance') together form a RC circuit. This system will have a RC charging time, determining the charging of the droplets before breakup. If the jet breaks up prior to the charging time, the droplets will not be fully charged by the gating mechanism. The system capacitance will charge the tip of the jet until it is pinched off. So, the time-dependent potential at the jet tip is:

$$U_{tip} = R_{jet} I_1 [1 - exp\left(\frac{-\tau}{R_{jet} C_p}\right)] \tag{5}$$

In the above equation, τ indicates the pinch off time of the droplets. By substituting the above equation into equation (4), we can obtain a final equation to calculate the induced current as function of the induction voltage.

$$I_1 / U_g = 1/(\tau/C_p + R_{jet}[1 - exp\left(\frac{-\tau}{R_{jet} C_p}\right)]\,) \tag{6}$$

The theoretical calculations are shown in figure 9 as dashed lines for two difference pore sizes. The induction rate increases rapidly with solution conductivity and reaches a saturated value which is determined by the capacitance of the system. In the first stage, the induction rate is governed by jet resistance. When the solution conductivity increases, U_{tip} decreases so that the effective induction voltage (equation 5) increases causing more charging of the jet tip. As a result, the induction rate will increase with solution conductivity. When the conductance of the solution is over 0.01 S/m, the electrical resistance of the liquid jet will not play a role any more since the voltage produced on liquid jet can be ignored compared with the applied voltage. The capacitance of the induction system will then dominate the induction rate on the droplets. A larger droplet size has a higher induction rate in general, due to the larger system capacitance (euqation 2). However, the induction rate per volume is lower than with the jet from a smaller pore.

4.2 Cylinder mode of induction

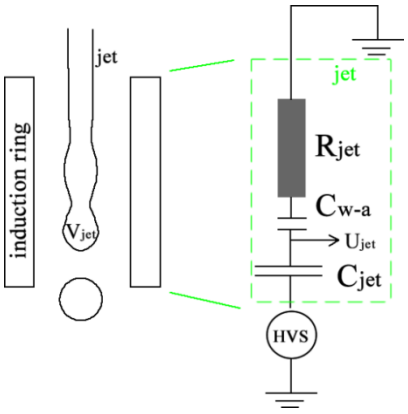

Figure 8 Schematic picture of liquid jet and equivalent circuit of current induction in 'cylinder mode'.

Many experiments studied the charge induction effects in a liquid jet, and many of them used a cylinder bucket as induction gate.[9] Also in our case, the induction ring is often placed close to the pore with a sufficient thickness, so that most of the liquid jet will be surrounded by the gate cylinder instead of being located under the jet opposite to its axis. The schematic image of figure 8 shows this position of the guard (induction) ring, which now surrounds most of the area of the jet. The capacitance of the system can now be simplified as a two-cylinder capacitance, with inner jet radius (a) and outer radius the ring opening (R_r). The capacitance of this cylinder system is known as:

$$C_c = \frac{2\pi\varepsilon l}{\ln(R_r/a)} C_2 \tag{7}$$

where l is the length of jet surrounded by the gate electrode. Because the electrical field in our case is not an “infinite” long cylinder, so that the field strength in our measurements is smaller than the field strength in an “infinite” long cylinder, thus a coefficient of capacitance C_2 is introduced in the equation and will be discussed later in the Appendix.

The charge quantity on the jet can again be calculated by a capacitance in cylinder mode C_C and the voltage difference between jet and gate U: $q = C_c \cdot U$. Then, the volume charge density in a cross section of the cylinder is:

$$\rho_e = q/(\pi r^2 l) \tag{8}$$

The generated streaming current will be calculated by multiplying flow rate and volume charge density,

$$I = \rho_e \cdot Q = \frac{2\pi\varepsilon_0 u_0}{\ln(R_r/a)} lU \tag{9}$$

where R_r and u_0 are the radius of gate ring and the velocity of the water jet. Substituting the voltage difference between the jet end and the applied gate voltage, we can obtain the current:

$$I = \frac{2\pi\varepsilon_0 u_0}{\ln\left(\frac{R_r}{R_j}\right)}[U_g - IR_{jet}] \tag{10}$$

Considering the fact that the charges are continuously transported from the reservoir to the tip of the jet, the voltage difference between gate and jet tip can be expressed as: U_g-R_{jet}×I. Substituting this voltage in equation 10 for U_g, we can calculate the induction current:

$$\frac{I}{U_g} = 1 \Big/ \frac{\ln\left(\frac{R_r}{a}\right)}{2\pi\varepsilon_0 u_0 C_2} + R_{jet} \tag{11}$$

Here, we didn't consider the RC charging time on the jet tip. This is because the liquid jet will be charged from the jet as it comes out of the pore, and not charged only at the jet end like in plate mode. So, the charges won't need to be transported through the entire jet and then charge the breaking-up droplets.

Measurements

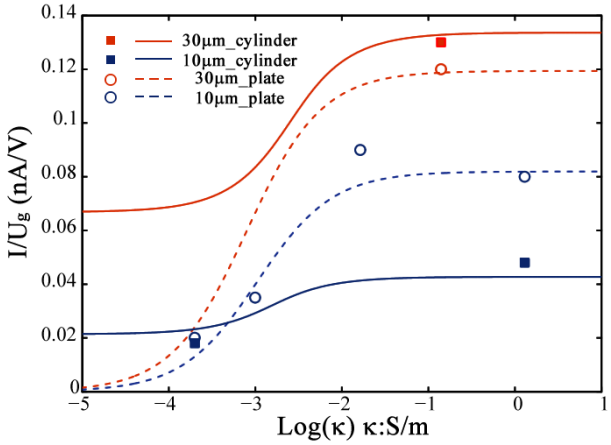

Figure 9. a. comparison of the induction rate (I/Ug) in cylinder mode and plate mode. The plate mode was calculated as an infinite large plate in front of jet, which is the upper limit of induction rate. However, it is not possible to reach this limit, since a hollow plate has to be used as induction electrode to allow passage of the liquid jet.

Two induction models of theoretical predictions are plotted in figure 9. The solid lines and dashed lines indicate the cylinder mode and plate mode of induction, respectively. The theoretical predictions are calculated under 1.4bar with a flow rate of 0.84μL/s in a 10μm pore and 6.3μL/s in a 30μm pore. The data points are either directly from measurements or from fitting of data points under different pressures of experimental results. From the above figure, we can clearly see that a high conductivity solution is more efficient for current induction. Since a larger pore will produce a larger radius of the liquid jet, the induction rate for a larger radius jet will increase. However, due to the larger flow rate, the induced charge density will be decreased.

Besides the conductivity of solution, the velocity of water jet or flow rate can also influence the induction current, mainly because of the mass flow and jet breakup time. Measurements were performed both in gate and cylinder induction mode of

the induced current as a function of flow rate and salt concentration and are shown in figure 10. The induction rate almost remains constant as a function of flow rate for DI water, but increases with flow rate with KCl solutions. The cylinder mode is generally more efficient to induce charges in droplets, as predicted above. This is mainly the case because in cylinder mode under our working conditions, a higher system capacitance can be obtained. By rescaling the hollow pore size of the ring, the length of the gate ring and/or the length of the liquid jet, the capacitance can be changed and as a result the induction rate.

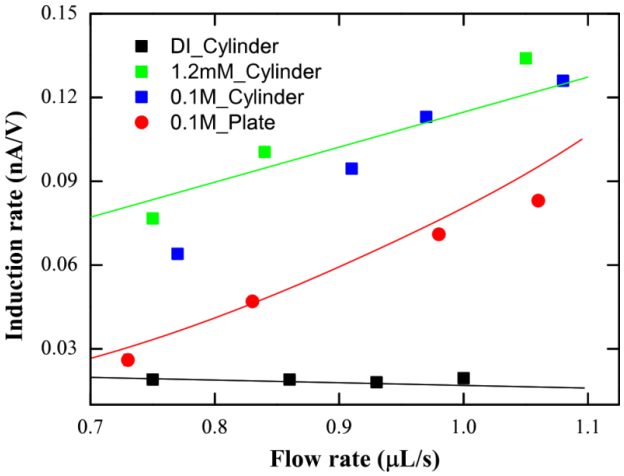

Figure 10 Induction rate as function of flow rate in a 10μm pore in two modes.

4.3 Discussion on effects of energy conversion

Induction of current can increase charge density in droplets, thus lowering the required target voltage for maximum energy conversion efficiency. This is quite useful for applications, since it might allow operating the device at lower voltages, close to the few hundred volts typically used in daily life, as we showed in the above measurements. However, the gate voltage can introduce additional losses and the comparison of two induction modes will be discussed below.

4.3.1 Plate mode

In plate mode, charged droplets are accelerated after jet breakup by the induction ring, and then decelerated between the induction ring and target electrode. According to the conservation of energy, the induction voltage does not increase or decrease the kinetic energy of droplets. However, the velocity increase of droplets due to the increased speed will lead to consumption of more energy by air friction.

The figure below briefly shows the energy distribution as function of traveling distance. Here we give an extreme example of low induction rate (10nA/2.25kV), to show clearly the energy decrease due to the acceleration of the droplets. The yellow area indicates the energy produced and consumed by the gate voltage, while the green area indicates the harvested energy by the target voltage. All the kinetic energy increase caused by the applied gate voltage will be consumed when the droplets fly out of the gate ring. Finally, around 70% of kinetic energy can be converted to electrical energy, which is lower than the over 80% with no voltage on the gate ring.

The jet itself before breakup will also be accelerated. The acceleration of water in the liquid jet can be calculated by the electrical forces due to charge density and electrical field. We will assume that the charge density is homogeneous along the liquid jet, and equal to the droplet charge density (typically $4C/m^3$). Considering that the typical applied voltage is 1kV for a distance between gate ring and chip of 1mm, the power used in electrically accelerating the jet by the induction gate is $P_{gate} = F_{el} * v$, with a typical jet length 500μm and radius of 5μm in the mean velocity v of the water jet (10m/s). Finally, the electrical power used to accelerate the liquid jet is approximately 1.6μW, which can be ignored compared with the typical input power of 100μW in 10μm pore. An additional argument that electrical forces on the jet can be neglected is, that no flow rate changes were observed when gate voltage was applied.

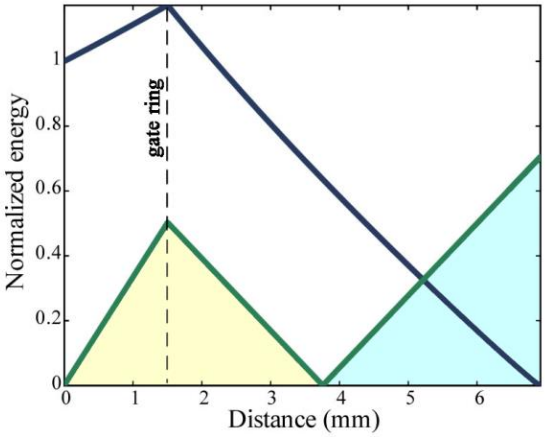

Figure 11. Schematic (normalized) energy distribution as function of travelling distance using plate mode induction. Droplets are accelerated by the gate ring and decelerated when droplets have past the gate ring. Blue lines indicate the kinetic energy variation as distance; green lines indicate the energy consumed or generated by electrical field. The yellow area indicates the kinetic energy increase and decrease by the gate ring, and the blue area indicates the energy gained at the target electrode.

4.3.2 Cylinder mode

We will assume 20μm diameter droplets with an initial velocity of 11.3m/s, and furthermore for simplicity that all kinetic energy is converted into electrical energy. This is impossible when droplets travel in air, but it can predict the upper voltage limit in the system. Using a high concentration solution (0.1M KCl) for the prediction we obtain $I = 0.126*U_g$.

The induction gate in cylinder mode will introduce additional loss factors. The droplets need to move against the field created by both induction voltage and target voltage, but the electrical energy is only harvested by moving against the target voltage. We define the gate efficiency as the efficiency for converting kinetic energy to electrical energy on the target:

$$eff_{gate} = \frac{U_{target}}{(U_{target}+U_g)} \quad (12)$$

As a result, the efficiency during transport of droplets shall be the result of both air friction and gate-target potential ratio.

$$eff_2 = eff_{air} \times eff_{gate}$$

Figure 12a shows the percentage of kinetic energy that can be converted to electrical energy.

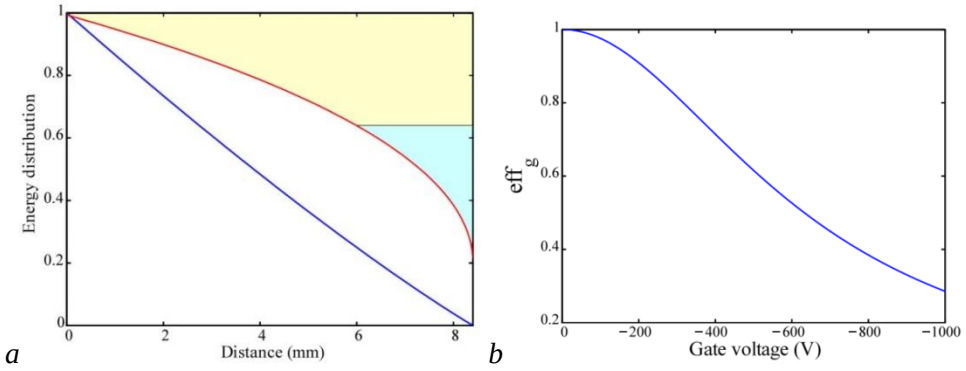

Figure 12. a. The energy distribution in the cylinder induction mode. In case of 50nA generated current induced by -396V gate voltage, we can obtain 440V volts on the target. The yellow area indicates the energy consumed by gate voltage and the blue area indicates the harvested electrical energy. B. The efficiency eff_{gate} *is defined in equation 12.*

Comparison between plate and cylinder mode

In principle, the energy conversion efficiency can be quite high for both modes, by using low gate voltages. However, as we discussed above, highly charged droplets and lower target voltages are preferable in practical applications. Hence, the induction rate and energy conversion performance in case of high induced currents will be discussed here. In our existing induction setup, the plate mode worked better than the cylinder induction mode, due to the effects of electrical field. We

experimentally found that the current is also easily influenced by the target voltage in cylinder mode. With increasing target voltage, the upstream current I_1 was seen to be lower in the cylinder mode at the same applied gate voltage. This can be explained by the fact that the electrical field more easily penetrates the induction ring in the cylinder mode due to the larger opening. Hence, higher induction voltages are required to keep the current constant. However, high induction voltages additionally consume the kinetic energy as we described above eff_{gate}. However, the energy conversion performance in cylinder mode can be improved by downscaling the hollow pore size of the gate electrode. A small spacing between jet surface and gate electrode can increase the capacitance of the system so that a much lower voltage is required to induce high currents from the reservoir. Since the opening then becomes smaller, the electrical field will additionally not easily penetrate into the pore and influence the charge induction. In conclusion it can be stated that further studies on design of the induction gate are still needed.

5. Conclusion

In this chapter, we successfully investigated gate controlled ballistic energy conversion systems, both experimentally and theoretically. We showed that the upstream current, determining the charge density of droplets, can be enhanced hundreds of times with respect to the current generated from the zeta potential. This provides a quite stable, surface potential independent system for ballistic energy conversion. In addition, there is no current flow through the gate so that we expect to have quite high efficiencies with relatively low target voltages. The efficiency with 10μm pores maximally reached 35%. The maximum efficiency with a 30μm pores was 48% due to less energy losses on viscous flow, surface production and air friction. A higher charge density in droplets can also be used to decreases the required target voltage for maximal energy conversion efficiency. Thus a 12% efficiency was achieved with 500V target voltage with a 10μm pore using voltage gating. We presented a theoretical analysis and set up two induction models which could both be compared to experimental data. By placing the gate at different positions we could induce charges more efficiently in the cylinder mode than in the plate mode. We experimentally studied and analyzed the charge induction rate as function of position, gate voltage and liquid flow rate. However, both modes will introduce additional energy losses. To obtain an optimal efficiency in system, a small gate voltage is preferred.

6. References

1. Vanberkel, G.J. and F.M. Zhou, *Characterization of an Electrospray Ion-Source as a Controlled-Current Electrolytic Cell.* Analytical Chemistry, 1995. **67**(17): p. 2916-2923.
2. Taylor, S.G., *Disintegration of Water Droplets in an Electric Field.* Proceedings of the Royal Society of London A: Mathematical, Physical & Engineering Sciences, , 1964. **291**: p. 145-158.
3. Rayleigh, L., *On the Equilibrium of Liquid Conducting Masses charged with Electricity.* Philosophical Magazine, 1882. **14**: p. 184–186.
4. Gomez, A. and K.Q. Tang, *Charge and Fission of Droplets in Electrostatic Sprays.* Physics of Fluids, 1994. **6**(1): p. 404-414.
5. Duft, D., et al., *Coulomb fission - Rayleigh jets from levitated microdroplets.* Nature, 2003. **421**(6919): p. 128-128.
6. Peek, F.W., *Dielectric Phenomena in High Voltage Engineering*1929: McGraw-Hill.
7. Yates, D.E., S. Levine, and T.W. Healy, *Site-Binding Model of Electrical Double-Layer at Oxide-Water Interface.* Journal of the Chemical Society-Faraday Transactions I, 1974. **70**: p. 1807-1818.
8. Dynarowicz, P. and M. Paluch, *Studies on the Electrical Double-Layer Structure at the Water Air Interface.* Colloid and Polymer Science, 1992. **270**(4): p. 349-352.
9. Schneide.Jm, et al., *Stability of an Electrified Liquid Jet.* Journal of Applied Physics, 1967. **38**(6): p. 2599-&.
10. van Hoeve, W., et al., *Breakup of diminutive Rayleigh jets.* Physics of Fluids, 2010. **22**(12).

7. Appendix

Correction on plate induction mode – formation of droplets

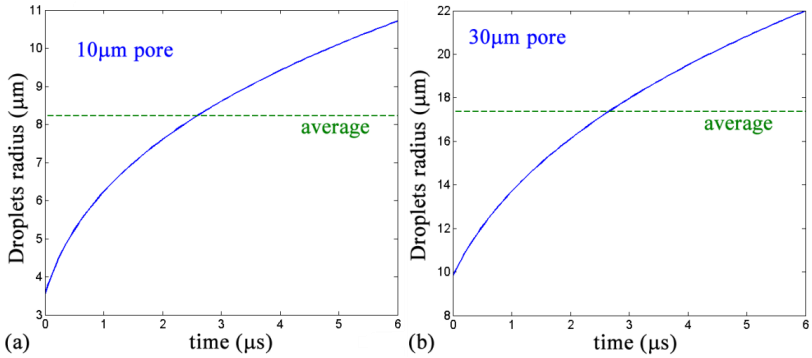

Figure 13. The droplet radius increases as function of time, changing the system capacitance and inducing a change of the induction rate as function of time. Since the capacitance is linearly proportional to radius, we can take the average value of the radius and use it for calculating the final capacitance.

The system capacitance is proportional to the droplet radius. However, the size of droplets keeps changing during the jet pinch-off process and thus system capacitance will also change according to equation 2. We assume the droplet radius starts at the the jet radius and ends at the radius of the droplets that we measured (see chapter 4). Since the volume flow rate is constant, we can calculate the droplet size increase as function of time by:

$$R^3 = \frac{3Q}{4\pi}t - \frac{r^3}{2}$$

The system capacitance is linearly proportional to droplet radius. Hence, we can take the average value of the capacitance within one pinch off cycle. According to equation 7, the average droplet size in one pinch-off cycle is a function of flow rate, shown in figure 14.

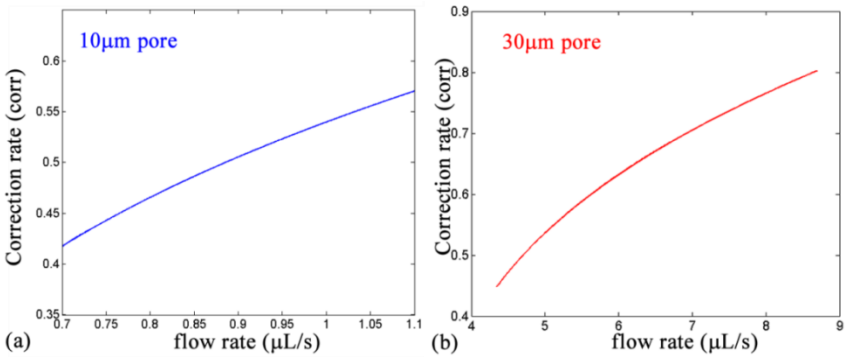

Figure 14. the correction coefficient C_1 on capacitance of plate mode by averaging droplet size over pinch-off circle.

Since we work with a Rayleigh- jet, the droplet size is indepent of flow rate.[10] So, a high flow rate will induce a high droplet pinch off frequency, so that the time for jet breakup is shorter. Capacitance correction values for jets from both 10μm and 30μm pores are show in figure 14. We find that the average droplet radius (time scaling) and correction coeffcienct C1 in equation 2 within pinch-off time cycle increases with flow rate. By substituting this correction coefficient, we can calculate the induction rate as function of the solution conductance.

Correction of Cylinder model – side effect

The capacitance in equation 8 is suitable for an infinite long cylinder. However, in our liquid induction system, a fringe effect of the electrical field in the cylinder inductor can't be ignored. As known, the electrical field on the edges of a cylinder is smaller than inside the cylinder, decreasing the capacitance of our system according to Gauss' law. The electrical field distributions for both an "infinite" cylinder and our system are shown in figure 15. Using these simulations we can obtain a correction value for the induction capacitance.

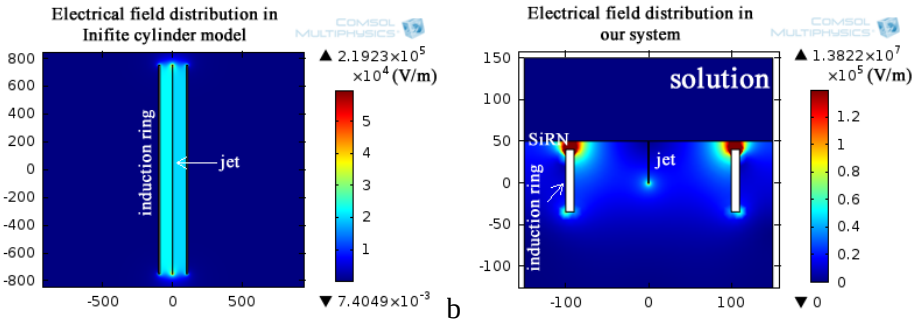

a b

Figure 15 a. The electrical field distribution in an "infinite" long cylinder. Warm color and cold color indicate the high and low electrical field. b. the electrical field distribution in our system.

This correction factor will change as function of jet length. After introducing this factor, the induction rates for both induction modes (plate and cylinder mode) were calculated. They are shown in figure 12.

Chapter 6

Self-excited ballistic energy harvesting device

A gate controlled system has many advantages such as stable current and low target voltage. However, as an energy conversion device, it is practically useful to remove all electrical power sources from the system. This chapter introduces a self-excited energy conversion design that is comparable to Kelvin's water dropper. Two types of voltage divider, using resistors and diodes, are used to produce stable gate induction voltages. Maximally 17.9% energy conversion efficiency was obtained with a diode- gated system and there is still more space to improve the conversion performance.

Manuscript to be submitted

1. Introduction

The gate-controlled ballistic energy conversion as introduced in the previous chapter has many advantages, such as stable, current adjustable and surface potential-independent current generation. With a well-controlled applied voltage on the metal guard ring, theoretically the charge density can be increased until the Rayleigh limit, so that the target potential can be decreased to the order of daily-use range. However, as an electrical energy conversion device it is not feasible to use a voltage source for electrical energy harvesting and all input energy should come from mechanical energy, rather than electrical energy. In addition, self-excited energy conversion system is convenient for application. Many other self-excited energy devices have been studied. [1-5]

In 1876, Lord Kelvin invented an electrostatic high voltage generator by water dripping, named the Kelvin water dropper.[6] The schematic picture of the setup is shown in figure 2a. Two metal buckets with a pore at the bottom drip water. The falling water drops pass through hollow metal rings and are collected by two other metal buckets. The hollow metal rings are cross-connected with these bottom buckets. As a result, any tiny charge on the water drops (e.g. a positive charge) that left the left-top bucket will charge the bottom left bucket and hence the right side ring. The metal ring on the right side will then attract more negative charges to the water drops on the right side, so that more net negative charges will be collected by bottom right bucket and the negative voltage increases on the left ring. Hence, a positive feedback exists and the two downstream buckets will continue this charging process until voltage breakdown occurs between the two bottom buckets, or drops are repelled and fall outside of the buckets. The Kelvin water dropper is a positive feedback system that can charge water drops from dripping driven by gravity.[7] However, the Kelvin water dropper has not been well developed since the voltage is too high for practical application and the harvested currents are very small with regard to the amount of water consumed.

We can apply the charge induction mode of Kelvin's generator to our ballistic energy conversion system. However, the positive feedback system is also an uncontrollable system. For a certain load resistance, there will be an optimal charge

density of droplets for energy conversion, otherwise overcharged droplets will easily be deflected causing a lower efficiency as can be seen from figure 4 in chapter 5. Taking a 30μm pore as an example, the optimal target voltage for a 1Tohm resistor is around 20kV, with a gate voltage around -170V. If we can obtain the proper gate voltage by dividing the target voltage using a voltage divider in Kelvin's induction system, the charge density will be properly controlled. This proper design and operation of this feedback system was attempted in the research described in this chapter.

Demonstration of current induction by gate voltage

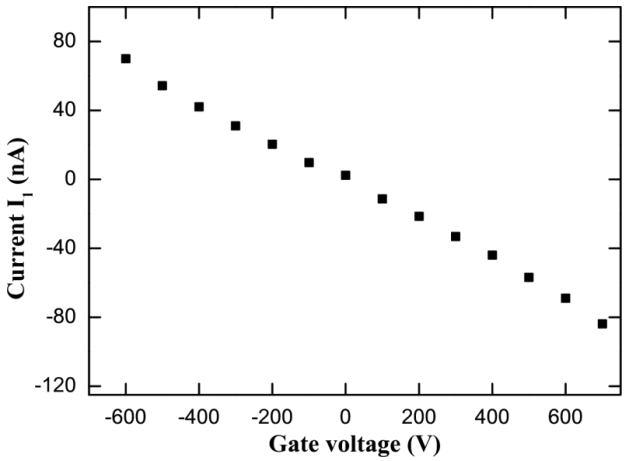

Figure 1 The principle of controlling the upstream current by gate induction. The polarity of current I_1 can be reversed by gate voltage. Solution 0.1M KCl, pore diameter 10 μm, applied pressure 2.2 bar.

As we described in chapter 5, a negative applied voltage on the gate can induce a positive current I_1 in the upstream reservoir, increasing the energy conversion stability by establishing a controllable current generation or charge density of droplets. To investigate the possibility of inducing both a positive and negative current be gate induction, as needed for self-excited, we performed a preliminary experiment in which we applied both a negative and positive gate voltage. The results are shown in Figure 1. The applied voltage ranges from -600V to 650V and in this case is supplied by a Keithley power source (2410). A 0.1M KCl solution

was used in this experiment and the water jet was forced by 2.2bar through a 10μm pore. We found that the current can be tuned from positive (75nA) to negative (-83nA). Hence, by adjusting the voltage on the gate ring, we can not only adjust the droplet charge density but also reverse the polarity of the current and droplet charge. This provides a possibility to use the design of the Kelvin water dropper to build a self-excited ballistic energy conversion device.

2. Principle and setup

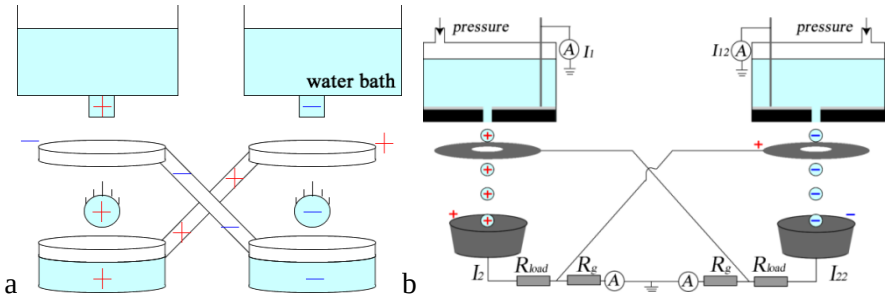

Figure 2a. the Kelvin water dropper driven by gravity, operating by setup of a positive feedback system. 1b Our self-gated ballistic energy system driven by pressure. Resistors form a voltage divider to separate the gate voltage from the target voltage.

Figure 2a gives the schematic figure of Kelvin's water dropper operating via the mechanism described in the introduction. Figure 2b shows the schematic picture of our proposed self-excited ballistic energy conversion device. Two silicon nitride membranes containing a single cylindrical pore with a diameter of 30 μm were mounted in pressurized PMMA reservoirs with rubber O-rings. The reservoirs contained degassed ultrapure 10m KCl solution. A layer of 150nm thickness Pt was sputtered at the back side of the chip for electrical connection with instruments via four copper pins. The mechanical input power can be calculated with measurement of the flow rate (Bronkhorst Cori-flow) and pressure using a pressure sensor (see Chapter 3). Two pieces of aluminum foil (with thickness of 0.2mm) were attached under the chip holders to function as induction gate. The current can be measured by either pico-ammeter (Keithley) or by connecting with a multi-meter. A multi-

meter in voltage range will show the voltage difference between an integrated 10MOhm resistor. The flowing through current can be calculated by the voltage reading: I = 10mV/10MOhm = 1nA.

In some experiments the current generated by deflection of droplets from the target to the gate ring (I_3) was measured using a multi-meter in the voltage range. Two stainless steel cups functioned as targets and were placed beneath the chip holders to collect charged droplets. The load resistance connected between these targets and ground was divided into two sections: resistors for electrical power generation and resistors for induction of the other jet, named R_{load} and R_g respectively. Resistors were immersed in an oil bath (Shell Diala S2-ZU-I) to prevent corona discharge and a layer of Delrin (Polyoxymethylene) was mounted at the edge of the cup for the same reason, at the location where the electrical field was expected to be the strongest.

Equivalent circuit

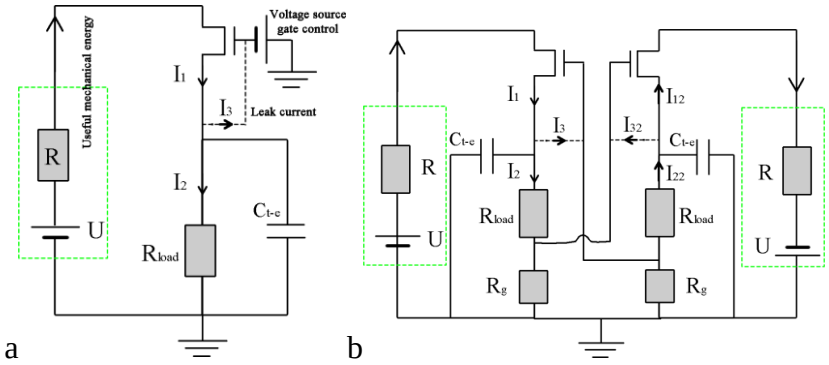

Figure 3. a. the equivalent circuit of gate controlled system in single micro jet system. The power source delivers an amount of useful mechanical power. Upstream current I_1 is induced (controlled) by a voltage source by an element with a function similar with the function of a field effect transistor (FET). The target voltage is produced by current I_2 flowing through R_{load}. I_3 is a leakage current induced by deflection of droplets to the guard ring or other leakages. b. The equivalent circuit of a self-excited ballistic energy conversion device. The

electrostatic current induction was modeled as a field effect-like transistor that allows current passage to be controlled by the voltage drop over the other R_g. $C_{t\text{-}e}$ and I_3 (I_{32}) respectively indicate the capacitance between target and earth, and the leakage current induced by deflected droplets, corona discharge or electrospraying.

To simply model the ballistic energy conversion principle, the device, including the mechanical parts, was converted to electronic elements and modeled as an equivalent circuit. The single gate controlled ballistic energy conversion device was modeled in figure 3a. The "equivalent" voltage source U_S represents the mechanical pressure driven energy source, with opposite polarity of the current. The mechanical power can be calculated by $P_{in} = (U_S)^2/R$. At constant pressure, the input power will also be constant. In principle, the current flow through the inner resistance R of the mechanical energy supply can range from 0 (non-charged micro jet) to the Rayleigh limit. The induction current (I_1 and I_2) in the top circuit is a linear function of the gate voltage as shown in figure 1. The function of the induction gate is modeled as a FET-like element in the circuit. With applied voltages on the "gate" (metal ring), more current will be induced between "source" (solution in reservoir) and "drain" (metal target). Then the current/charges will be captured in the droplets and fly to the target. When the charged droplets are collected by the target they produce a high voltage via the resistors. In addition, there will be two possible ways for current leakage: from the highly charged target to the grounded environment (such as the grounded Faraday cage) and to the reversely charged induction gate. The deflected droplets or corona discharge can also produce a leakage current I_3, marked as a dashed line, representing droplets reflected from the target when the product of I_2 and R_{load} exceeds the power of the power source. I_3 therefore only flows at high target voltages. In the self-excited system (Fig 3b), the current of two jets were interactively induced by placing a voltage divider at downstream current as we described above. The current leakage via I_3 can thus be considered as a negative feedback limiting the gate voltage to a balanced value, preventing I_2*V_{target} to exceed P_{in}. Finally, we can create a self-excited ballistic energy conversion as shown in Fig.3b. Here each gate voltage will be produced by current flowing through the voltage divider of the other device.

3. Experiment results

3.1 Gating by resistors

First, two 1T Ohm resistors were series connected for power generation and gate induction. In figure 4a, we can see clearly that the upstream currents I_1 and I_{12} start to increase rapidly after the upper electrodes were connected to the ammeter. The upstream currents from the two jets have different polarities, showing successful operation in feedback mode. Both currents reached a saturated value quickly and droplets were seen to be deflected to the gate ring, decreasing the current flow through R_g and the gate voltage. These deflected droplets can be considered as a negative feedback to the gate voltage that keep the charge density at an proper level. As we know however, the deflected droplets don't contribute to energy conversion. In addition, the deflected droplets contacting the gate electrodes decreased the current flow through R_g, thus doubling the electrical energy losses. The periodic transients in the current level weren't because of voltage breakdown, but because charged water that accumulated at the bottom of the gate by deflected droplets dropped to the downstream metal target. From figure 4b it can be seen that the downstream currents I_2 and I_{22} which are the currents through R_g, were much smaller than the upstream currents, because partially the charged droplets were deflected reducing the current through R_g and generating a current through the gate ring.

To calculate the electrical output power, we need to know the current flowing through all the resistors. For simplification, we can extract the electrical elements from the setup and make a simple circuit drawing shown as figure 4c. The current flow through the gate was measured by a multi-meter in voltage range. A 10MOhm resistor is integrated in the multimeter in the voltage range, so that the current can be calculated by the voltage reading of the multimeter divided by 10MOhm. Finally, according to Kirchhoff's circuit law, the current flow through R_{load} equals the sum of the current through the gate and R_g. The output power of two jets thus calculated is 225.8μW. From measurements of the flow rate (13.12μL/s) and pressure (1.40bar), the efficiency of whole system is then calculated as 12.3%.

The reason for the low efficiency in this setup is that the R_g is too high for proper induction of charges. Assuming there is no leakage current by deflected droplets, 10nA will introduce 10kV on gate ring, which is too high an induction voltage when compared with the results obtained in chapter 5 (figure 4). Another reason for the low efficiency is that the highly charged droplets repel each other and form a cone when they move out of the gate. Hence, less air wake will be formed so that air friction force losses increase. Besides, the difference in trajectory distance for droplets at the outside and inside of the cone will also cause a lower efficiency.

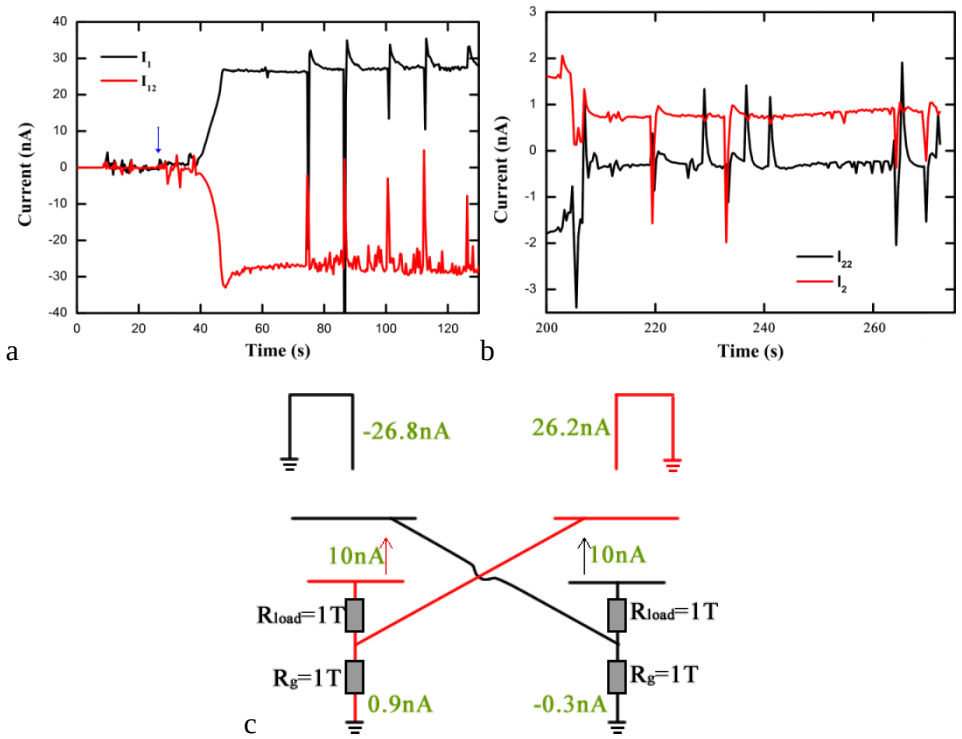

Figure 4. Measurements using the self-gating system. a. The upstream currents I_1 and I_{12} increase as function of time. The blue arrow indicates when the induction gate was connected. b Both downstream currents I_2 and I_{22} after some time of operation. c The circuit diagram with indicated current values.

As we analyzed above, the 1T ohm resistor is too high as R_g. Hence, a lower value of R_g is recommended for gating. According to our experimental results in chapter

5 (figure 4), the optimal gate voltage is about 170V for a 1Tohm R_{load} in 30μm pore experiments. From the ratio of optimal target voltage and gate voltage (20kV/170V), we can find that the optimal R_g = 8.5MΩ when a 1Tohm R_{load} is connected. The resulting simplified electrical circuits are shown in figure 5 for three different connections, so that we can easily calculate the electrical output power. Experiments were performed using these configurations and the upstream and downstream currents measured are shown in the figure.

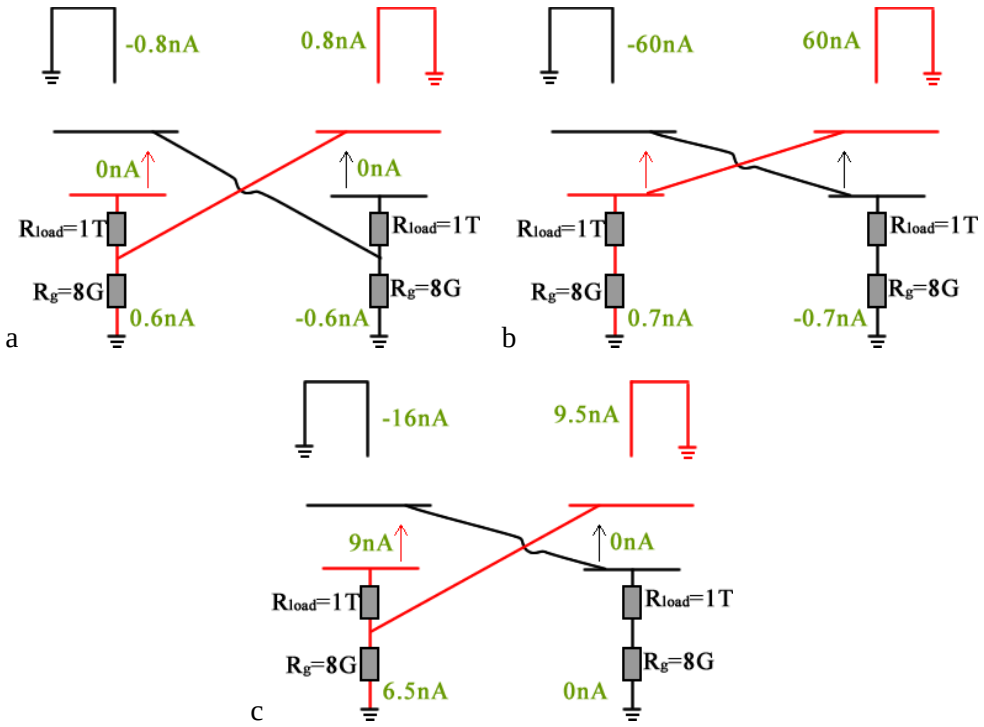

Figure 5. Three experiments performed using 8GΩ R_g resistors in different connections and the current flows obtained. a.A symmetric connection of R_g can produce current constantly, but in a low value. B. The typical connection of Kelvin's dropper. Most droplets are highly charged and deflected to the gate ring. c. An asymmetric connection of R_g. 30μm pore and 10mM KCl aqueous solution was used in these experiments.

By symmetric connection of R_g shown in figure 5a, the upstream current is slightly induced. The induced current remained quite stable at the such low values within at least 10min duration of the measurements. This is possibly because the R_g is too small to generate an appreciable voltage on the gate ring, so that hardly a current is induced from the reservoir. With the typical Kelvin's dropper connection (figure 5b) on the other hand, using R_{load} instead of R_g, the droplets are immediately charged and deflected to the gate ring. This indicates that the droplets become easily overcharged compared with an optimal current with a certain load resistance. The deflection of droplets can be considered as a negative feedback to decrease the gate voltage. As we know from Chapter 3, the deflection of droplets is one of the causes of electrical energy loss. However, in the self-excited system, the deflected droplets will touch the gate balancing the current from the other downstream cuircuit, thus decreasing the current flow through R_g. Hence, the deflection of droplets will double the electrical energy loss in the self-excited system. Finally, by assymetric connection of resistors (figure 5c), this mechanism of energy loss is seen more clearly on the right side jet. The current I_1 on the left side can be well induced. However, the deflection of droplets balanced the downstream current through the right side resistance, so that almost no power can be produced from the jet on the right side. The influence of the resistance can be seen clearly from the difference of induced upstream current between two jets. The Kirchhoff laws won't work if we take the upstream current in consideration, since a lot of droplets loss occurred to the environment.

Theoretically, 8GOhm should be the optimal R_g connected with 1TOhm load resistance for energy current induction. However, the current shown in figure 5a is much lower than expected. The possible reason is that 8GOhm is still practically lower than the required R_g. The conclusion is that the control of gate voltage still needs further investigation. One possible way is to used the current and induction rates defined in chapter 5, since the induction currents are linearly related with the gate voltage, and therefore with the target voltage in case of self-excited. Further studies are thus still required for optimal self-excited operation.

3.2 Gating by diodes

When gating by resistors it is very difficult to control the induction voltage. Since the gate voltage is determined by ohmic resistors, the droplets are either been easily overcharged or not charged at all. Even though the gate resistor voltage divider decreases the induction voltage considerably, it is still a positive feedback system. Deflected charged droplets will play the role of negative feedback, decreasing the gate voltage. Hence, we propose to gate the micro jet by reversely connecting a diode, which provides a constant voltage with increasing current. As a result, the gate voltage can stay in a constant reasonable range preventing overcharging the droplets. The I-V curve of a reversely connected diode (MULTICOMP - UF4001) was measured and is shown below. An accurate current source (Keithley 2410) was used to apply a constant DC current and measure the voltage difference in real time. It can be seen in figure 6 that a quite small DC current (4 nA) can produce about 500V between the terminals of the diode and this voltage will be almost independent of the current. As a result, we can use the inversly connected diode to produce a constant gate voltage allowing more stable energy conversion.

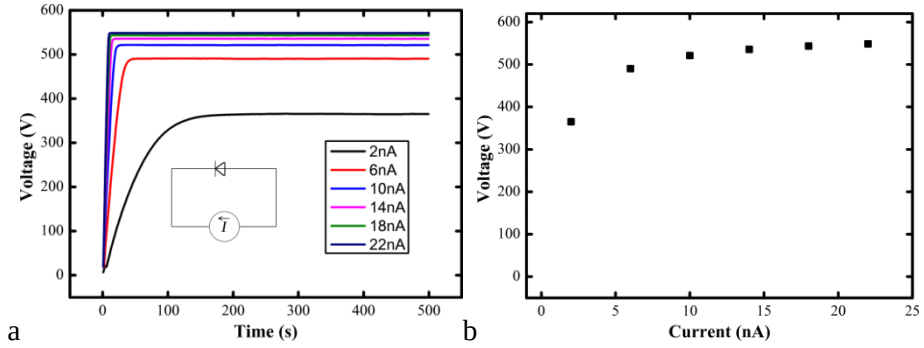

Figure 6. a. Reversed voltage generated over the diode by a constant DC current as a function of time. Currents in the nA range can produce around 500V voltage drop. b. The I-V curve after 500 seconds. At higher currents the voltage becomes saturated and independent of the applied current, so that the gate voltage will remain constant and won't overcharge the droplets.

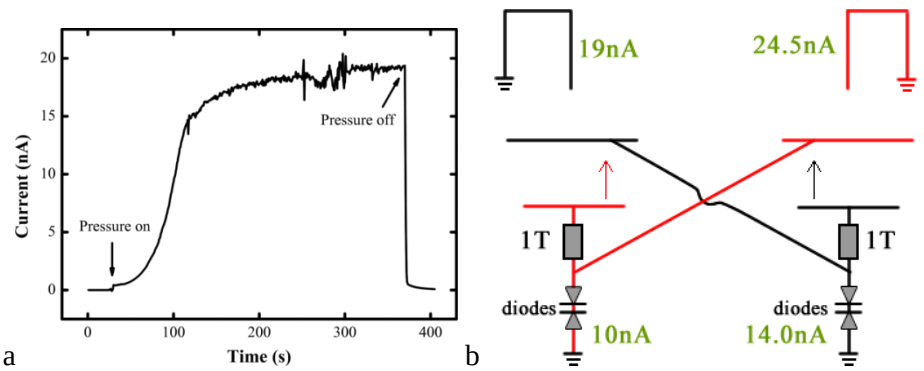

Figure 7. a. The rise of current I_{12} as a function of time. A clear saturated current can be found and the current disappears immediately when the pressure been turned off. b. Scheme of the electrical circuit and measured currents. The efficiency can be calculated by simultaneous measurement of flow rate and pressure.

Instead of a single diode in reverse connection, two diodes were connected in opposite directions to prevent random charging of the two microjets (Fig7.b). As the pressure was turned on, less than 1nA current was initially generated by the microjet due to the streaming current (Fig7.a). This value is much lower than the streaming current measured in Chapter 3 because of the use of a salt solution (10mM KCl). The current then rapidly increased because of current flowing through the diodes and generating an induction voltage. When the current was over 15nA, it reached a saturated value (finally around 19nA). It could also be seen that the noise in the saturated current section is larger, which we think was caused by deflected droplets landing on the gate.

The difference between using diodes and resistors is that a stable voltage can be produced for induction of current, so that the droplets won't be overcharged. It can indeed be seen from figure 7.a. that a much higher current (than downstream current gated by resisitors in figure 4 and 5) was measured at the downstream. The target voltage can be approximately calculated by the sum of the voltage over the resistor and the diodes (about 500V when the downstream current is over 4nA). With measurement of the flow rate for the two microjets (12.3μL/s) and the applied pressure (1.40bar), we can calculate that the total efficiency of the self-excited system is at least 17.9%. Because partially the current will be balanced by those of

the deflected droplets, the current through R_{load} is larger than the value we measured and hence the efficiency is probably underestimated. In addition, there is more space to improve the performance of energy conversion, such as changing the pore size on the gate ring, designing the target and the modifying the properties of the diodes.

4. Further discussion and conclusion

The self-excited ballistic energy conversion system conceptually is comparable to the Kelvin's water droppper, although the systems fundamentally differ in driving force and energy conversion mechanism. No theoretical analysis on the energy conversion efficiency of Kelvin's water dropper has been made yet. However, theoretically the energy loss is expected to be quite low for Kelvin's water dropper, due to the low surface energy and air friction. However, the actual limitation of Kelvin's water dropper is the need for a high voltage on the collector and a high volume flow of water. Because of the low surface-bulk ratio, the induced charge density will be quite small, which means a high target voltage is required for high effciency. In our case, micrometer sized droplets are produced from the pore with initially a high speed which droplets are decelerated by target voltage. Since the droplets can be highly charged, the target voltage can be decreased to hundreds of volts as shown in figure 5 in chapter 5. We present a DC voltage microfluidic energy harvesting device. However, by proper design and connection of the circuit, it can also switch to AC voltage. [8]

In this chapter, we demonstrated that both the droplet charge density and polarity can be changed using a voltage source. This provided the possibility that we can use a cross connection of target and gate ring to induce the current, a similar method as used in Kelvin's water dropper. To prevent the droplets from being overcharged, a voltage divider was connected at the downstream circuit. As a result, the gate voltage could be separated from the target voltage, providing the possibility of stable current and energy generation. Experimentally, we succesfully induced inversed currents from two liquid jets and obtain 12% energy conversion efficiency. By using reversely connected diodes, the gate voltage can be regulated in a reasonable range in a stable way. Much higher downstream currents were then

observed and a maximum efficiency of 17.9% was obtained experimentally. However, further research is still required as the optimal method to control the gate resistance still needs to be found out.

5. References

1. Alolah, A.I., *Static Power Conversion from 3-Phase Self-Excited Induction and Reluctance Generators.* Electric Power Systems Research, 1994. **31**(2): p. 111-118.
2. Arrillaga, J. and D.B. Watson, *Static Power Conversion from Self-Excited Induction Generators.* Proceedings of the Institution of Electrical Engineers-London, 1978. **125**(8): p. 743-746.
3. Sait, H.H., S.A. Daniel, and P.M. Babu, *Analysis and control of an Autonomous Hybrid Wind-driven PM alternator and Photovoltaic Array without battery storage.* 2008 Ieee Region 10 Conference: Tencon 2008, Vols 1-4, 2008: p. 2391-2395.
4. Singh, G.K., *Self-excited induction generator research - a survey.* Electric Power Systems Research, 2004. **69**(2-3): p. 107-114.
5. Wu, J.C., *AC/DC power conversion interface for self-excited induction generator.* Iet Renewable Power Generation, 2009. **3**(2): p. 144-151.
6. Kelvin, L., *On a self-acting apparatus for multiplying and maintaining electric charges, with applications to illustrate the voltaic theory.* Proceedings of the Royal Society of London, 1867. **16**: p. 67-72.
7. Ziaei-Moayyed, M., E. Goodman, and P. Williams, *Electrical deflection of polar liquid streams: A misunderstood demonstration.* Journal of Chemical Education, 2000. **77**(11): p. 1520-1524.
8. Zahn, M., *Self-Excited Ac High-Voltage Generation Using Water Droplets.* American Journal of Physics, 1973. **41**(2): p. 196-202.

Chapter 7

Summary and Outlook

1. Summary

The rapid economic development and increasing consumption of electrical energy requires people to generate more energy. The new energy sources developed are required to be clean and environmentally friendly. [1, 2]Microfluidic energy harvesting device is relatively less known compared with other popular renewable energy sources, such as solar cell and bio-fuels, but can provide such a clean and environmentally-friendly source.

When the net charges inside the electrical double layer (EDL) are transported by water flow, they produce electrical current which can be harvested via connection of electrodes at two ends of a channel. Electrical power can then be generated by load resistors connected in the external circuit. However, the maximum experimental efficiency in channels with overlapping EDLs is only 3-5% in nanochannels or nanopores.[3, 4] Many theories predict that the efficiency can be much improved with slipping boundary, however this has not yet been achieved in experiments. [5] The maximum possible theoretical efficiency in such systems is 50%, since at maximum power conversion a leakage current ('conduction current') will run through the internal resistance of the channel of equal magnitude to the current through the external circuit.

We investigated the energy conversion performance by the streaming potential using totally different approaches. By introducing gas bubbles, which can be considered as perfect insulators, the internal electrical resistance of the system can be increased, decreasing the conduction current. Following this approach, according to an equivalent circuit analysis, experimentally we achieved over 163 times efficiency increase compared with single water phase flow. The absolute efficiency however was still quite low, due to the corner conduction and high bulk conductivity of the solution used, as well as the use of microchannels. Hydrophobic surfaces are expected to further increase the energy conversion efficiency according to our preliminary experiments.

The conduction current decreases the efficiency for traditional energy conversion from streaming potential. To totally prevent the conduction current, we took a

radically different approach. The flow chart below shows how the ballistic energy conversion principle is fundamentally different from traditional energy conversion from streaming potential. We employ a microjet system which is described by fundamentally new physics. It operates in two stages: first pressure is converted to kinetic energy and subsequently kinetic energy is converted to electrical energy. In the first stage a stream of high-velocity charged droplets is produced by forcing water through a micropore. The microjet formed then breaks up into droplets by the Rayleigh-Plateau instability. The droplets have acquired their charge from the EDL at the membrane surface. In the second stage the charged droplets travel through an electrical field towards a high-potential target, decelerating them to zero speed. The target acquires its potential by droplet impact. Current is drawn from the target to do useful work. The second process can be represented simply by the equation $ma = -qE$.

Experimentally, we found that the average optimal efficiency from a 10μm pore using this approach is over 30%, with an output power of 42μW under 1.4 bar pressure and 1 μL/s flow rate for a single pore. Because we found this conversion mechanism is fundamentally different from traditional energy harvesting from streaming potential, we called it “ballistic” energy conversion.

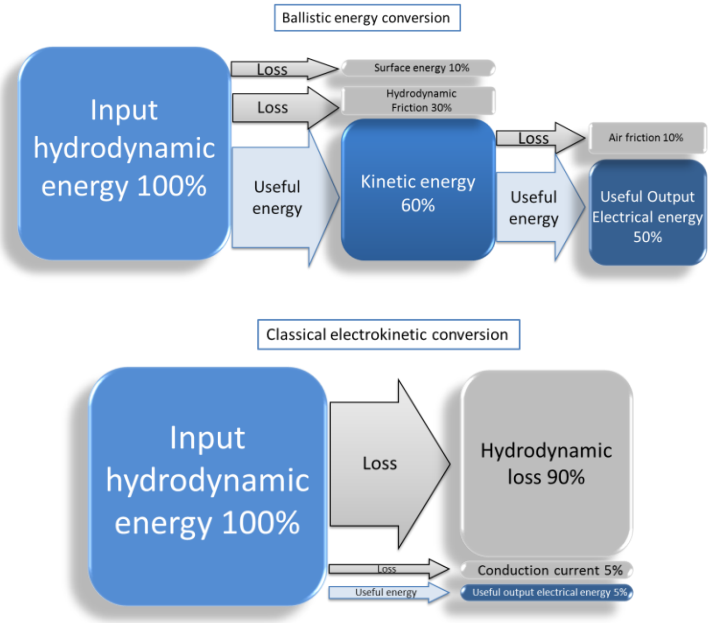

The classical electrokinetic energy conversion mechanism is entirely different. It relies on a single stage conversion by forcing liquid through a channel with charged walls. Acceleration now plays no role (low Re). Conversion in a high-friction high-conductivity environment gives as main loss factors hydrodynamic friction and a conduction current back through the channel. As already mentioned above, best conversion efficiencies experimentally achieved were only 5%.

To determine the limit of the ballistic energy conversion system, we experimentally measured and theoretically modelled energy losses during the conversion process from pressure energy to electrical energy. For a 10μm pore, a 52% energy loss was experimentally observed from pressure to knetic energy of droplets in step 1. With the theoretical investigations, 33% energy losses by viscous forces and 22% by creating surface were expected, in good agreement with experimental results. A lower energy loss in larger pores is theoretically expected due to the decrease of the surface-bulk ratio, causing lower viscous loss (25%), surface energy (8.4%) and air friction losses (6%). Experimentally, we found a 35% energy loss by droplet generation using a 30 μm pore, in a good agreement with the simulations.

A large pore will thus create less energy loss due to the lower surface-bulk ratio. However, this lower ratio will also decrease the net charge density on droplets where the net charges come from transport through the EDL. To obtain a high efficiency, a higher target voltage is then required to decelerate the droplets with low charge density thus giving more chance of electrical energy losses due to processes as corona discharge and electro-spraying. Hence, highly charged droplets are preferable in the system. To achieve this, we applied voltages on the guard ring to create an electrical field to electrostatically induce more charge in the droplets. It was found that the charge density increases linearly with applied voltage. Using this approach nearly 50% efficiency was obtained from experiments. We experimentally found two modes for induction of charges, named plate mode and cylinder mode. A theoretical analysis was given to explain and to estimate the magnitude of current induction by gating.

For a practically useful electrical energy harvesting device, the input energy source should be entirely mechanical, without the need for a voltage source integrated in the system. Thus, combining the ballistic principle with the design of Kelvin's water dropper [6], we can also apply two jets and introduce cross-connected induction rings in our system. However, Kelvin's water dropper is a positive feedback system which has the consequence that the voltages become too high and most of the charged droplets become deflected to the induction ring, so that less current flows through the load resistors producing electrical power. We improved the design by incorporating a voltage divider so that the voltage on gate can be separated from the target voltage, leading to a stable power generation system.

2. Outlook

2.1 Power density and power generation in membrane

Besides energy conversion efficiency, another very important factor in energy conversion is the power density. This is also quite important for a portable device, which must take up a relatively small space but needs to provide high power. From our existing experiment, the maximum output power produced by 1.4 bar in a 30

μm pore (shown in figure 4 chapter 5) is about 400μW. Considering a 50×50μm square cell, the power density obtained can be 160kW/m^2. So, by integration of parallel pores in a membrane, the output power can be 400W in a 5×5 cm^2 membrane under 1.4bar with volume flow rate 6.5L/s. This is far leading the existing renewable energy conversion methods, such as wind power (85.61W/m^2) [7, 8], solar cell (170W/m^2)[9], traditional hydropower station (considering the water surface area in average 2.98W/m^2)[10], and traditional energy conversion from streaming potential (3W/m^2)[3]. By scaling up, we can thus at least in principle obtain quite a high power in a small area, which might be good for the local environment. However, as can be read in this thesis there are still quite a lot of technical problems that need to be solved. The purity of water is a quite critical problem, since any tiny particle can clog the micropore, which then can't constantly produce a liquid jet. Filtering can here provide a possible solution.

2.2 Design of target electrode

From the theoretical calculations in chapter 4, the limit of energy conversion efficiency (63%) in a 30μm pore is still higher than the experimental results (48%). According to Peek's equation, the measured target voltage (20kV) is about the limit of operation voltage (24kV) due to small curvature of target. Thus, a better design of target collector is required for further studies and application.

In addition, as we described in chapter 5, highly charged droplets are preferable since it can decrease the required target voltage, which is especially useful for practical application. However, these highly charged droplets have a higher electrostatic repulsion force between each other and therefore form a spray cone. This spray cone introduces two disadvantages: first, no air wake or less air wake will be formed, so that air friction loss will increase. Second, the optimal trajectory distances for the droplets at the outside and inside of the cone are different. As a result, more droplets are likely to be deflected and energy conversion efficiency will decrease.

Finally, to satisfy these two key technical design factors, a target with large curvature, smooth surface and circular shape is required. The membrane with guard ring will be placed in the geometrical center of the target.

2.3 The design for application

One of the advantages of microfluidics and "Lab on a chip" techniques is the possibility to integrate complicated systems into a piece of chip and devices. Besides, the ballistic energy conversion device can be quite simple, since it only requires a micro-machined membrane, a metal target and pure water.

As we described above, the ballistic energy conversion can provide quite a high power density (160kW/m^2 under 1.4 bar). Considering a person with 80kg weight, the pressure generated from the footprint is about 3bar, thus 800W electrical power can be produced by standing. The figure below shows a –greatly preliminary- design for application. A flexible air cushion was integrated under the shoes. Steps push the air in the reservoir via a check valve. Pressure drives the water through the membrane and produces energy, which can be collected and then used for example for charging the cell phone.

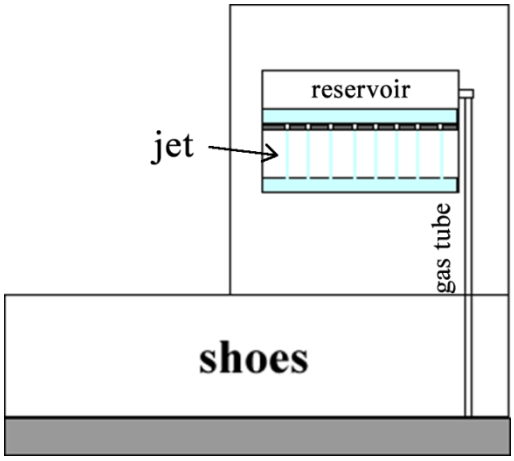

3. References

1. Weisz, P., *Long term energy solutions: The truth behind the silent lie - Reply.* Physics Today, 2004. **57**(11): p. 18-20.
2. Hoffert, M.I., et al., *Energy implications of future stabilization of atmospheric CO2 content.* Nature, 1998. **395**(6705): p. 881-884.
3. Xie, Y.B., et al., *Electric energy generation in single track-etched nanopores.* Applied Physics Letters, 2008. **93**(16): p. -.
4. van der Heyden, F.H.J., et al., *Power generation by pressure-driven transport of ions in nanofluidic channels.* Nano Letters, 2007. **7**(4): p. 1022-1025.
5. Ren, Y.Q. and D. Stein, *Slip-enhanced electrokinetic energy conversion in nanofluidic channels.* Nanotechnology, 2008. **19**(19): p. -.
6. Kelvin, L., *On a self-acting apparatus for multiplying and maintaining electric charges, with applications to illustrate the voltaic theory.* Proceedings of the Royal Society of London, 1867. **16**: p. 67-72.
7. Sopian, K., M.Y.H. Othman, and A. Wirsat, *The wind energy potential of Malaysia.* Renewable Energy, 1995. **6**(8): p. 1005-1016.
8. Darus, Z.M., et al., *Potential of Wind Energy in Sustainable Development of Resort Island in Malaysia: A Case Study of Pulau Perhentian (Perhentian Island).* Mathematical Methods, Computational Techniques, Non-Linear Systems, Intelligent Systems, 2008: p. 431-435.
9. SMIL, V. *ENERGY AT THE CROSSROADS* in *Scientific Challenges for Energy Research* 2006. Paris.
10. Marco Aurelio dos Santos, L.P.R., Bohdan Sikar, Elizabeth Sikar, Ednaldo Oliveira dos Santos, *Gross greenhouse gas fluxes from hydro-power reservoir compared to thermo-power plants.* Energy Policy, 2006. **34**: p. 481–488.

List of Publications

Journals

- Published work

- **Yanbo Xie** and John D. Sherwood and Lingling Shui and Albert van den Berg and Jan C.T. Eijkel* "Strong enhancement of streaming current power by application of two phase flow." ***Lab on a chip***, **23**, 4006-4011, 2011 (Selected as HOT articles for open free access)
- Trieu Nguyen, **Yanbo Xie**, Vreede de, L.J. Berg van den, A. and Jan. C.T. Eijkel*, "Highly enhanced energy conversion from the streaming current by polymer addition", ***Lab on a Chip***, **13**, 3210-3216, 2013
- John D. Sherwood, **Yanbo Xie**, Albert van den Berg and Jan C. T. Eijkel, "Theoretical aspects of electrical power generation from two-phase flow streaming potentials" ***Microfluid Nanofluid*, 15**, Issue 3, pp 347-359**,** 2013
- Marin G. Alvaro, Wim van Hoeve, Garcia-Sanchez Pablo, Lingling Shui, **Yanbo Xie**, Marco A. Fontelos, Jan C.T. Eijkel, Albert van den Berg and Detlef, Lohse*, "The microfluidic Kelvin water dropper", ***Lab on a chip***, (accepted)

- Unpublished work

- **Yanbo Xie**, Diederik Bos, Lennart J. de Vreede, Hans L. de Boer, Mark-Jan van der Meulen, Michel Versluis, Ad J. Sprenkels, Albert van den Berg, Jan C.T. Eijkel * "High-efficiency ballistic energy conversion in a microjet" (submitted)
- Diederik Bos[#], **Yanbo Xie**[#], Michel Versluis, Mark-Jan van der Meulen, Albert van den Berg, Jan C.T. Eijkel* "Theoretical investigation of ballistic energy conversion" (ready to submit; [#] these author contributed equally)
- **Yanbo Xie**, Hans L. de Boer, Albert van den Berg, Jan C.T. Eijkel "Self-excited ballistic energy harvesting microfluidic device" (Manuscript in preparation)
- **Yanbo Xie**, Diederik Bos, Hans L. de Boer, Albert van den Berg and Jan C.T. Eijkel, "Gate controlled high efficiency ballistic energy conversion system" (ready to submit)
- Songyue Chen, **Yanbo Xie**, Arpita De, Albert van den Berg, Edwin T. Carlen. "Electrical shielding for silicon nanowire biosensor in microchannels"
- Tuan Tran, Yoshiyuki Tagawa*, **Yanbo Xie**, Chao Sun, and Detlef Lohse, "Microdroplet impact on superheated surfaces: Vapor triggers splashing" (submitted)

Patent

Yanbo Xie, Jan C.T. Eijkel, HIGH EFFICIENCY ENERGY CONVERSION USING THE STREAMING POTENTIAL, 14079452, 2012

Conferences

-Oral presentation

- **Yanbo Xie,** Lennart de Vreede, Nguyen Trieu, Hans de Boer, Ad Sprenkels, Albert van den Berg, and Jan C.T. Eijkel, (2012) "High efficiency energy conversion from liquid jet flow". *MicroTAS 2012*.
- **Yanbo Xie,** and John D. Sherwood, and Lingling Shui, and Albert van den Berg, and Jan C.T. Eijkel, "Strong enhancement of streaming current power by application of two phase flow". *Powermems 2010*
- **Yanbo Xie**, Lennart de Vreede, Trieu Nguyen, Albert van den Berg, Jan C.T. Eijkel, HIGH EFFICIENCY ENERGY CONVERSION FROM LIQUID JET FLOW, *MFHS2012*

-Poster presentation

- **Yanbo Xie**, Diederik Bos, Hans de Boer, Albert van den Berg and Jan C.T. Eijkel, Gate controlled high efficiency ballistic energy conversion system, *MicroTas 2013* (accepted)
- **Yanbo Xie**, Lennart de Vreede, Albert van den Berg, Jan C.T. Eijkel, OPTIMIZING LIQUID WATER JET ON ENERGY CONVERSION PERFORMANCE , *Power MEMS, 2012*
- **Yanbo Xie,** and John D. Sherwood, and Lingling Shui, and Albert van den Berg, and Jan C.T. Eijkel, "Strong enhancement of streaming current power by application of two phase flow". *MicroTas 2011*

Acknowledgements

Four-year research in BIOS has passed so quickly, here I would like to express my gratitude to all who have ever helped, discussed with me and accompanied me.

First of all, I would like to express my deepest appreciation to you, my promotor Jan Eijkel. It was you who introduced me to this group and guided me how to become an independent researcher. I really enjoyed every meeting since you give me fully freedom to express my own ideas. You are patient, kind, multidisciplinary and with extraordinary knowledge and always introduced me to the right person who can accelerate the progress of research. I do learn a lot from you from scientific aspects and beyond.

Thank you Albert, for giving me the chance to work in your lab. In the monthly meeting, you always provided me with a different view of my work and gave many novel ideas and suggestions. I did learn that the applications of scientific research are sometimes more important. Besides, the social activities such as the BBQ and Mountain biking will be one of the most impressive moments in my memories.

I appreciated that we have a lot of experts in electrical, mechanical engineering and cleanroom work. Thank you, Hans. When I proposed my difficult designs of the chip holders and setup, you always tried your best to help me. Ad, you helped me a lot with the measurements of high voltage and low current systems, creating so many possibilities for the experiments that I can do. Lennart, you helped me with the chip design and preliminary experiments of the micro jet. Thanks for your work. Johan, thank you for your guidance in the cleanroom. Paul, you helped me to deal with the ordering and transfer smiling to everyone. Jan van Nieuwkasteele, thanks for your help with the microscopy in the first two years.

Michel, you helped me learn a lot both in theory and experiments with the liquid jet. Mark-Jan, thank you for helping us to make a series of nice movies of the liquid jet, as our first look at our own micro liquid jet. I would also like to thank Dr. John Sherwood. At the time when I was struggling to build up a theory on energy conversion from bubble flow, you came to our University and quickly solved all my problems, but forgive me that I still feel headache when reading your equations ;). Diederik, you joined my project for your Master thesis and you did

excellent work on the theoretical modeling, accelerating my understanding and the experimental process. Lingling, thank you for your help when I just came to the group and getting familiar with all kind of techniques. Chao, from the POF group, thanks for your trust which gave me a chance to have a look at other new research projects. Edwin, thank you for your kind help and discussion at my early stage of research. “You only have four years”. Now I realized this is so true.

Hermine, thanks for arranging all the documentary stuff, it is always fast and efficient. Thanks to my previous room mates: Mingliang, Masood, Rerngchai, Lonneke, Maarten and Laura. I really enjoyed working with you together. To the other Biotes, I would like to thank you all for the contribution to a smooth working atmosphere: Wouter, Severine, Eddy, Mathieu, JP, Justyna, Loes, Sertan, Yawar, Verena, Adi, Rogier, Allison, Floris, Arpita, Burcu, Evelien, Natalia, Trieu, Susan, Fleur, Loan, Wesley, Bjorn, Zhenxia, Wei-shu, Alexander and others of whom I haven’t a name.

Thanks Songyue and Haizheng who agreed to be my paranymghs. Songyue, I am pleasured with our discussions and lunch time (with Yifan). Haizheng, I have enjoyed the discussion including all the topics we are interested in.

Thanks for all my Chinese friends in the Netherlands. Excuse me that there are so many people that I can’t name them one by one. I am so happy living and studying with your together. You all made me feel free to speak mother languages and share the happiness.

Last, but not least, I would like to thank my wife Jiazhen for her understanding and love during the past few years. Your support and encouragement was in the end that made this dissertation possible.

Yanbo
Sep. 2013
in Enschede